NASA CR-174844

CREEP FATIGUE LIFE PREDICTION
FOR ENGINE HOT SECTION MATERIALS (ISOTROPIC)
SECOND ANNUAL REPORT

by V. Moreno, D.M. Nissley, and L.S. Lin

United Technologies Corporation
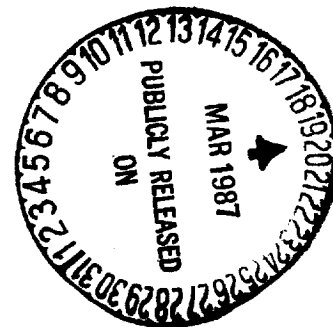Pratt & Whitney Group
Engineering Division

December 1984

Prepared For
NATIONAL AERONAUTICS AND SPACE ADMINISTRATION

LEWIS RESEARCH CENTER
2100 BROOKPARK ROAD
CLEVELAND, OHIO 44135

Contract NAS3-23288

Copy No. 00119

PREFACE

The Second Annual Report contained in this document covers the activities performed during the first two years of the NASA HOST Program, "Creep Fatigue Life Prediction for Engine Hot Section Materials (Isotropic)", under Contract NAS3-23288. The objective of this effort is to improve the high temperature crack initiation prediction technology for gas turbine hot section components. This program is being conducted under the direction of Dr. G.R. Halford who serves as the NASA Program Manager. The Program Manager and Principal Investigator at United Technologies Corporation (UTC) is Mr. Vito Moreno. Mr D.M. Nissley significantly contributed to the analytical effort for data reduction and model evaluations. Dr. L.S. Lin performed all of the metallographic examinations and interpretations of this information. The authors would like to express their gratitude to Messrs R. Masci and N. Glowac for their efforts in conducting the fatigue testing.

PRECEDING PAGE BLANK NOT FILMED

Table of Contents

SECTION 1.0

INTRODUCTION

The overall operating cost of the modern gas turbine engine is greatly
influenced by the durability of combustor and turbine structural components
operating at high temperatures. Inadequate durability results in reduced
engine efficiency and increased maintenance costs due to premature repair and
replacement. To increase the durability of these components, more accurate
structural analysis and life prediction methods must be developed for
components operating at higher temperatures. However, improvements in the
state-of-the art technology for elevated temperature durability prediction
have been hampered by 1) the severe operating conditions of the engine, 2) the
inability of analytical and life prediction tools used in the design of lower
temperature components to predict complex material behavior and interaction of
damage mechanisms of components at elevated temperatures, and 3) the high cost
of engine development testing which prohibits the accumulation of adequate
failure data and local operating conditions required for the systematic
development and calibration of durability prediction models.

Traditionally, component durability associated with fatigue cracking has been
attributed to separate crack initiation and crack propagation processes.
Current cyclic crack initiation prediction methodology is based on correlative
fatigue models generally developed to address a specific component or loading
configuration. These prediction models are directly calibrated to
macroscopically observable and predictable quantities (strain range, mean
stress, etc.) and do not address the specific mechanisms associated with the
initiation process. This approach has been successful at lower temperatures
but its applicability at higher temperatures, where interaction of deformation
mechanisms and damage accumulation is strongly temperature dependent, has not
been established. This is particularly true for the higher strength isotropic
alloys used in gas turbine hot section structures.

The NASA Hot Section Technology (HOST) program is aimed at developing improved life prediction technology for structures operating at elevated temperatures. As part of HOST, the present program will investigate fundamental approaches to high temperature crack initiation life prediction, identify modeling strategies and develop specific models for component relevant loading conditions. The program is a 5-year, 2-part effort (2-year base program plus a 3 year optional program) that will consider two isotropic hot section materials and protective coating systems. Under the base program, various life prediction approaches for high temperature applications have been investigated and basic models for simple cycle, isothermal loading conditions selected and developed. Models that address thermomechanical cycling, multi-axial conditions, cumulative loading, environmental effects and cyclic mean stress will be developed under the optional program. These models will be verified on an alternate material.

SECTION 2.0

SUMMARY

This report summarizes the activities performed during the first two years of the NASA HOST Program, "Creep Fatigue Life Prediction for Engine Hot Section Materials (Isotropic)", being conducted by Pratt & Whitney Aircraft. The program is a 5-year, two part effort aimed at improving the high temperature crack initiation prediction technology for gas turbine hot section components. The two-year base program comprised the following tasks:

Task I - Material/Coating/Component Selection and Acquisition
Task II - Screen Candidate Life Prediction Approaches
Task III - Evaluate Best Candidate Life Prediction Approach
Task IV - Reporting

Significant results of the program are listed below. A discussion of the technical progress of the program is provided in the following section.

The major results of Task I are summarized below:

1. Cast B1900 + Hf and wrought IN 718 were selected as the base and alternate materials, respectively.

2. A single heat of B1900 + Hf was obtained and test specimens fabricated.

3. The material was characterized with respect to grain size, ' size, carbide distribution, and dislocation density.

4. Monotonic tensile and creep testing demonstrated engineering properties within anticipated scatter for this material.

5. Examination of the tensile tests has shown a transition from inhomogeneous "planar" slip within the grains at lower temperatures to more homogeneous matrix deformation at higher temperatures.

6. Examination of the creep tests has shown a transgranular failure mode at 760°C (1400°F) and an intergranular failure mode at 871°C (1600°F) and 982°C (1800°F).

7. A study was conducted that investigated the effects of test specimen geometry and fabrication process on fatigue life. As a result, the axial strain controlled specimens were designed with a smooth (no extensometer ridges) gage section and fabricated using centerless grinding followed by light electropolishing.

8. A fatigue test matrix was established to provide baseline data to define crack initiation life as a function of major variables and for life prediction model evaluation. Approximately 100 strain controlled fatigue tests have been completed. Major variables investigated were temperature, strain range, strain rate, mean strain, and strain hold times.

9. Examination of specimens during testing indicated that measurable 0.76mm(.030 in.) surface cracks appear early in the specimen cycle lives. This has been used as the definition of crack initiation for the initial model evaluation work.

10. Observed crack initiation sites are all surface origins associated with either grain boundary carbides or local porosity. The initiation life is not significantly affected by the character of the site.

11. Transgrannular cracking was observed at most initiation sites.

The major results of Task II are summarized below:

1. A total of seven different life prediction models were evaluated using the data generated in Task I. The specific models included:

   A. Coffin-Manson
   B. Damage Rate (Majumdar)

C. Hysteresis Energy (Ostergren)

D. Crack Tip Opening Displacement

E. Linear Elastic Fracture Mechanics

F. Total Strain - Strainrange Partitioning

G. Ductility Exhaustion

Each model was evaluated with respect to its predictive capability and the types of data required for the determination of the model constants.

2. Most of the models were able to accurately regress baseline data used for model constant determination. However, none were considered to demonstrate the degree of predictive capability together with simple data (test) requirements to serve as the basis for a practical and useable life prediction model for gas turbine hot section components.

The major results of Task III are summarized below:

1. A life prediction approach, designated Cyclic Damage Accumulation (CDA), has demonstrated good predictive capability with the minimum data requirements. As currently proposed all model constants are determinable from rapid cycle fatigue, monotonic tensile and creep tests.

2. The model is fundamentally a Ductility Exhaustion approach in which the cyclic capability (ductility) of the material grains is exhausted by a damage parameter integrated through the cyclic evolutionary response.

3. The transgrannular initiation, observed in the majority of tests, was considered to be indicative of a grain damaging process. Those cycles which generated intergrannular initiation were considered a grain boundary damaging process. Based on similarities of the deformation structures, the grain and grain boundary cyclic capabilities were associated with the amount of primary and secondary creep observed in monotonic creep loading tests.

5

4. At temperatures where time dependent deformation is normally not considered a significant process, the grain cyclic capability is assumed to be related to the amount of residual inelastic strain (% elongation) observed in a monotonic tensile tests.

5. The cyclic damage parameter is based on determination of a reference damage rate. The reference condition for this work has been fully reversed, strain controlled fatigue tests conducted at a strain rate of 0.00167 sec^{-1}. The reference damage rate is determined as the cyclic grain capability divided by the observed number of cycles to crack initiation.

6. For cycles other than the reference condition, two damage ratios representing time independent and time dependent processes, are used to modify the damage reference rate. The damage ratios, determined from the stress response, are considered an advantage of this method since absolute damage increments are not calculated.

7. Application of the model to the prediction of fatigue tests not used in the constant determination has shown the ability to predict strainrate, mean strain and hold time effects.

8. Sensitivity analyses were conducted to evaluate the predictive capability for various assumptions regarding initiation crack definition and the accuracy of the local stresses. Some loss in predictive capability was demonstrated but the model was still able to adequately predict the trend in life associated with various cycle parameters.

SECTION 3.0

TECHNICAL PROGRESS

3.1 TASK I - MATERIAL/COATING/COMPONENT SELECTION AND ACQUISITION

3.1.1 Hot Section Survey and Material Selection

A survey was conducted of the isotropic materials and surface protection coating systems currently in use in the hot section of commercial gas turbine engines. The results of the survey, shown in Table I, indicate that the predominant hot section materials are high strength nickel base alloys in either cast or wrought form. Furthermore, the surface protection coating systems currently can be classified as either diffusion or overlay. A recommendation identifying the materials and coating systems for the base and option programs was submitted to the NASA Program Manager who approved the following selections:

Base Material: Cast B1900 + Hf (PWA 1455)
Alternate Material: Wrought IN 718 (AMS 5663)
Coatings: Diffusion Aluminide (NiAl)/Overlay (MCrAlY)

These selections provide an opportunity to investigate generic creep-fatigue crack initiation mechanisms and life prediction approaches for a wide range of relevant hot section materials and applications. The use of cast and wrought alloys allows the development and examination of life prediction models for two materials having the same matrix (Ni) but significantly different composition and microstructure (e.g., high vs low volume fraction γ'). The selection of a diffusion and an overlay coating also provides a variation in composition and microstructure and will be useful in developing mechanistically based life prediction models. These material/coating systems provide the broadest range of generic information consistent with the goals of the HOST program.

Table I

Hot Section Materials and Surface Protection Coating Systems

Material Designation	Form/Base	Usage/Comments
B1900 + Hf (PWA 1455)	Cast - Ni	o High Pressure Turbine (HPT) Blade and Vane Application o Potential Segmented Combustor Use
IN 792 (PWA 1467)	Cast + HIP - Ni	o Sideplate and Vane Application
IN 713C (PWA 655)	Cast - Ni	o Extensive Low Pressure Turbine (LPT) Vane Application o HPT Sideplate Application
MAR-M-509 (PWA 647)	Cast - Co	o HPT 1st Vane Application o Strategic Material
IN 718 (AMS 5662)	Wrought - Ni	o Extensive Projected Use in Hot Section Static and Rotating Structures
Hastelloy X (PWA 1038)	Wrought - Ni	o Combustor Liner Sheet Alloy o Single Phase Alloy - Conclusions may not be Relevant to Other Hot Section Superalloys
Haynes 188 (PWA 1042)	Wrought - Co	o Combustor Liner Sheet Alloy o Strategic Material

Coating Type	Composition	Comments
Diffusion Aluminide	NiAl	o Extensive Blade and Vane Application o State of the Art for Oxidation Coatings
Overlay	MCrAlY	o Different Composition and Microstructure o Compatible with Application of Thermal Barrier

8

3.1.2 Base Material Description

The B1900 + Hf material selected for the program was part of a single heat, designated W-0098, obtained from Certified Alloy Products Inc., Long Beach, California. The chemical composition of this heat is compared to nominal specifications in Table II. A total of 2500 pounds of material was obtained for specimen fabrication.

Table II

Chemical Composition of B1900 + Hf (Heat W-0098)

Element	Nominal (%)	Heat W-0098
C	0.11	0.09
Cr	8.0	7.72
Co	10.0	9.91
Mo	6.0	5.97
Al	6.0	6.07
Ta	4.3	4.21
Ti	1.0	0.99
B	0.015	0.016
Zr	0.08	0.04
Fe	0.35*	0.17
W	0.1*	0.04
Cb	0.1*	0.08
Bi	0.5 ppm	0.1
Pb	10.0 ppm	0.1
Hf	1.5	1.19
Ni	Remainder	Remainder

*Maximum

Two casting geometries were selected for specimen fabrication. The "standard" bar shown in Figure 1A was initially selected because it could accommodate all anticipated test specimen configurations. The constant section bar (Figure 1B) was later cast to investigate the effects of porosity on material properties (see Section 3.1.4). For both bar geometries the casting parameters, melt and mold temperatures, were established to produce a uniform small grain size in each bar. This would result in a large number of grains in a specimen cross-section and insure an "isotropic" material response.
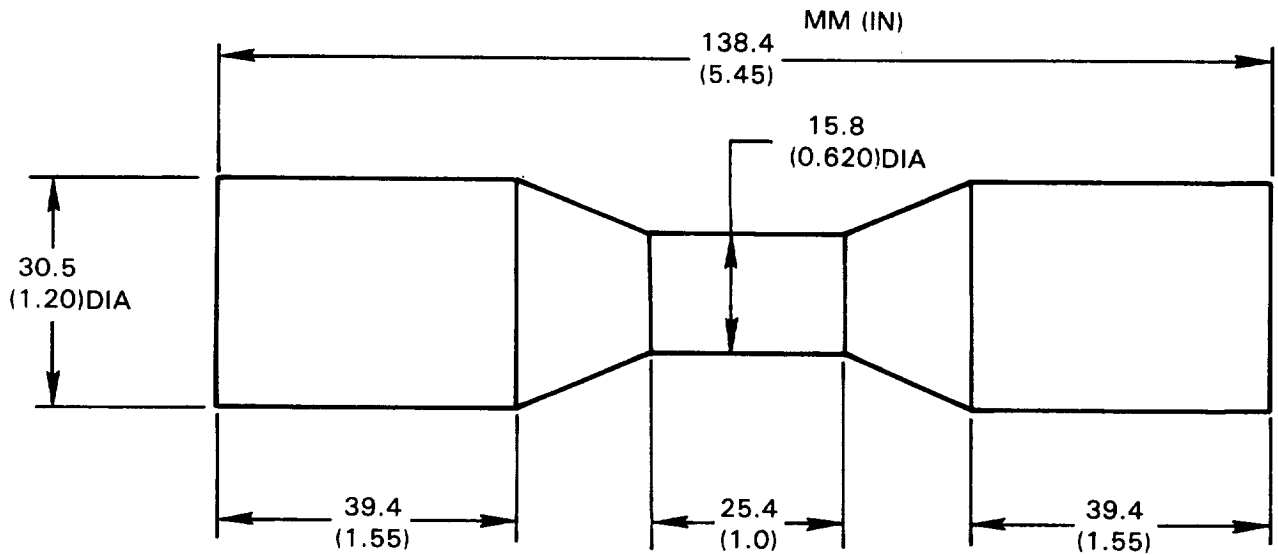
(A) "Standard" Bar Configuration
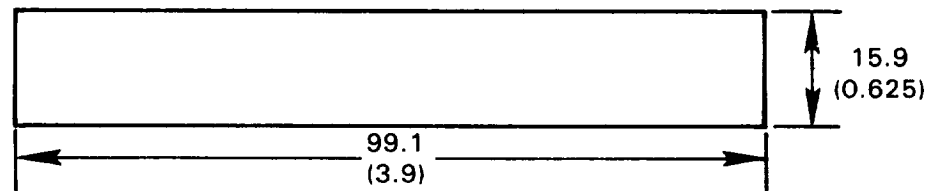
(B) Constant Section Bar

Figure 1 Casting Geometries Used for Test Specimens

All bars were fully heat treated prior to machining. The heat treatment cycle included:

Solution - 1079 ± 14°C (1975 ± 25°F) for 4 hours; air cool

Precipitation - 899 ± 14°C (1650 ± 25°F) for 10 hours; air cool

For future reference, all cast bars were given an identifying designation. The "standard" bars were cast four bars at a time. The molds were numbered sequentially from number one, with individual bars designated A, B, C or D. The cylindrical bars were numbered sequentially starting with 647.

10

The structure of the material was documented in both the as-cast and fully heat treated condition using optical, SEM and TEM techniques. The following observations were made:

1. Use of a micrograph (300X) showed the grain size of both the as-cast and fully heat treated material to be between ASTM No. 1 and 2. This represents an average grain diameter of 0.018 cm (0.007 in) to 0.025 cm (0.010 in) which should produce isotropic stress and strain conditions in the test specimens. A comparison of the micrographs and the ASTM standard is shown in Figure 2.

2. The replica technique was used to study the gamma prime, γ', size and distribution within the grains. In the as-cast material, the γ' size was 0.6 μm while the fully heat treated material showed an increase in size to 0.9 μm (see Figure 3).

3. MC carbides were observed in the grain boundaries of both the as-cast and fully heat treated material (see Figure 4). Microprobe analysis indicated that the carbides are enriched in Ta, Ti, Mo, and Hf.

4. For future assessment of deformation accumulated in specimens after testing, initial dislocation density measurements were made. Representative dislocation networks for the as-cast and fully heat treated materials are shown in Figure 5. Calculated densities are about 9.3 x 10^9/cm^2 for the as-cast material and about 5.7 x 10^9/cm^2 for the fully heat treated material.

3.1.3 Tensile and Creep Characterization

Monotonic tensile and creep testing of B1900 + Hf specimens was conducted to document typical engineering quantities and define deformation and failure mechanisms. Specimen geometries used for this testing are shown in Figure 6.
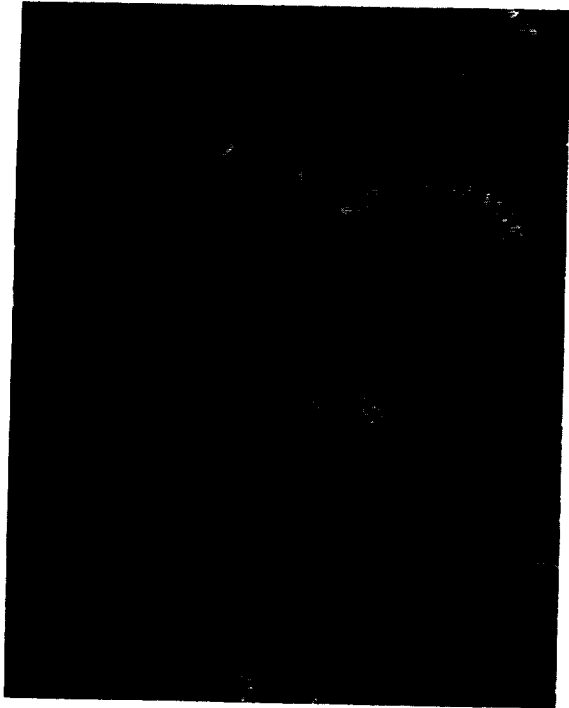
AS - CAST
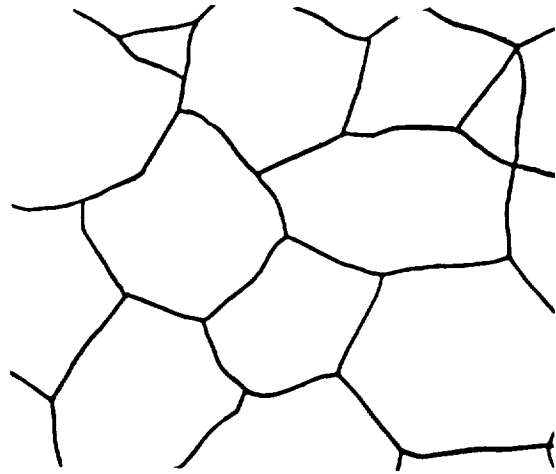
ASTM STANDARD No. 1   100 μm
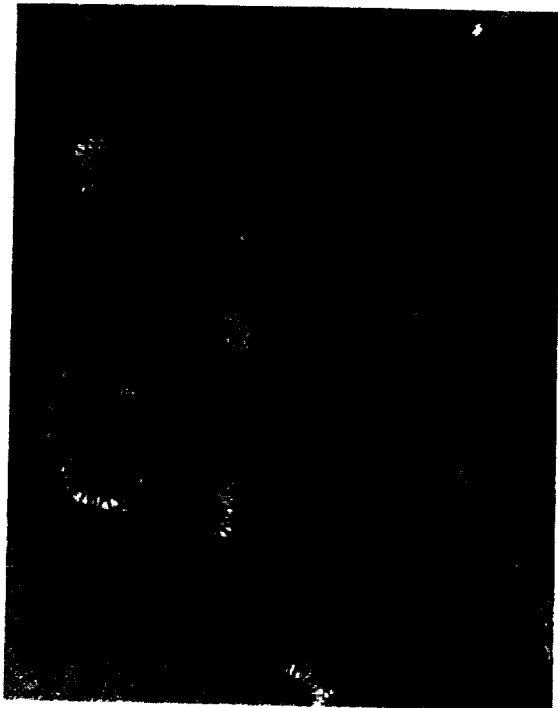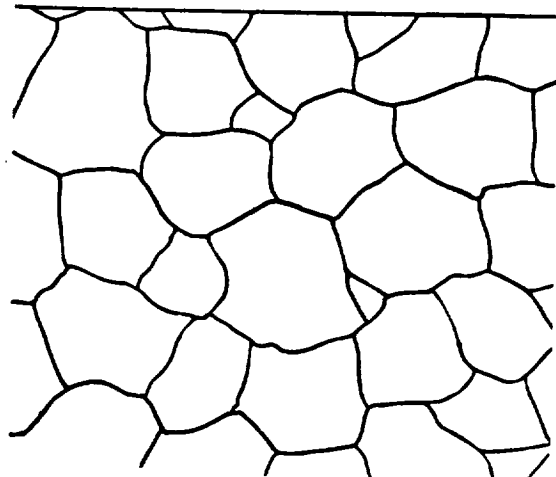
FULLY HEAT TREATED

ASTM STANDARD No. 2   100 μm

Figure 2   Grain Size of As-Cast and Fully Heat Treated Material
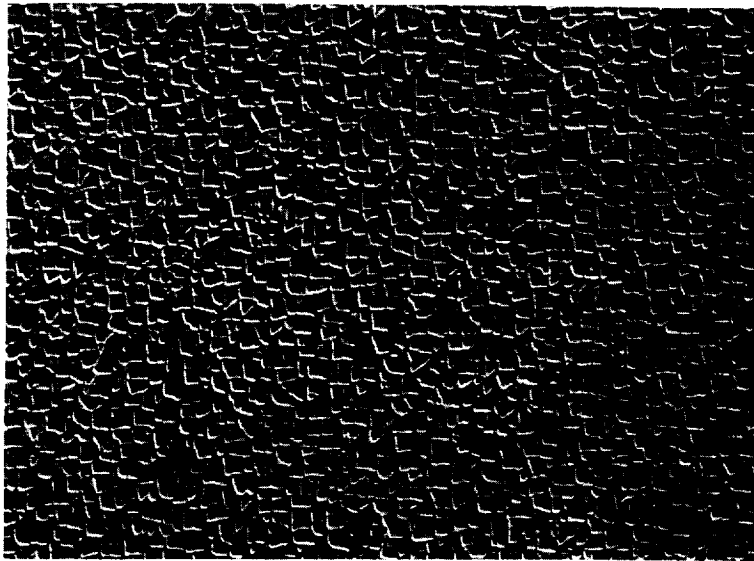
As-Cast $\gamma' = 0.6\,\mu m$ 10μm
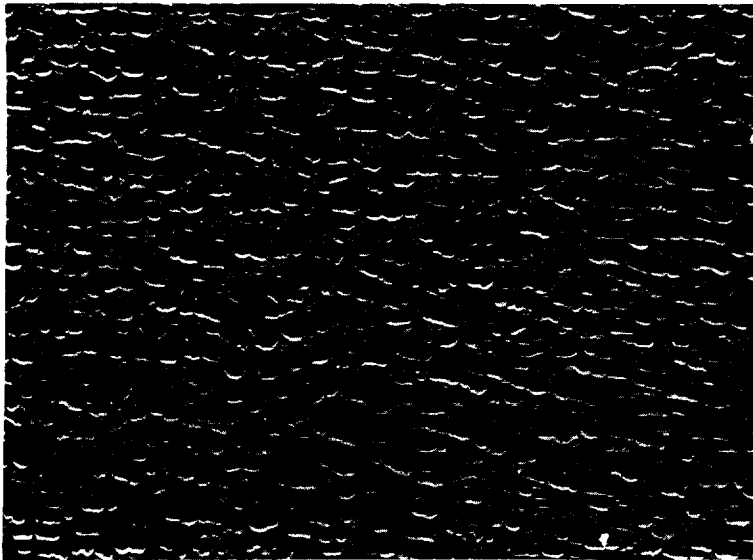
Fully Heat Treated $\gamma' = 0.9\,\mu m$ 10μm

Figure 3   Gamma Prime (γ') Shows Increase with Heat Treatment

As-Cast   25 µm

                           25 µm
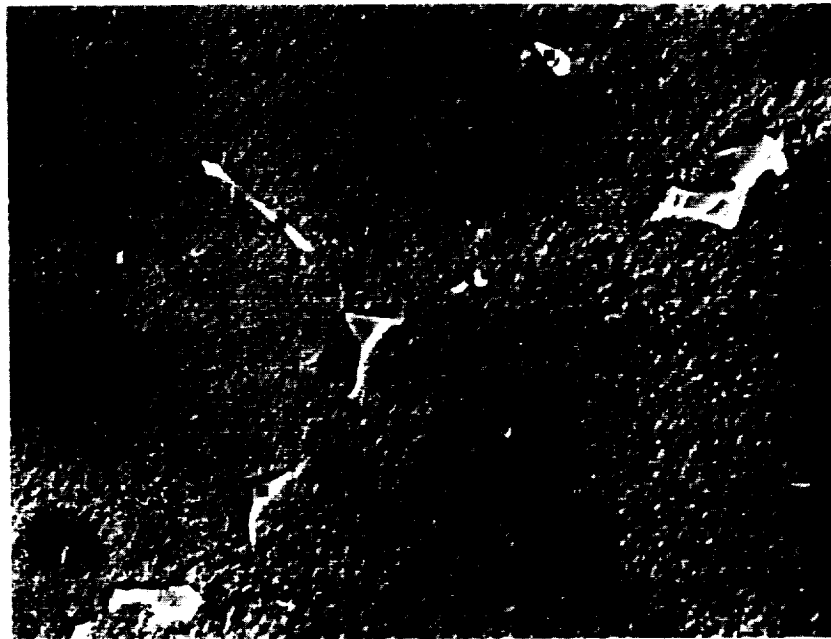
Fully Heat Treated

Figure 4 Typical Distribution of Carbides Along Grain Boundaries

As-Cast $\rho = 9.3 \times 10^9/cm^2$ 1 μm

Fully Heat Treated $\rho = 5.7 \times 10^9/cm^2$ 1 μm

Figure 5   Dislocation Networks for As-Cast and Fully Heat Treated Materials

15
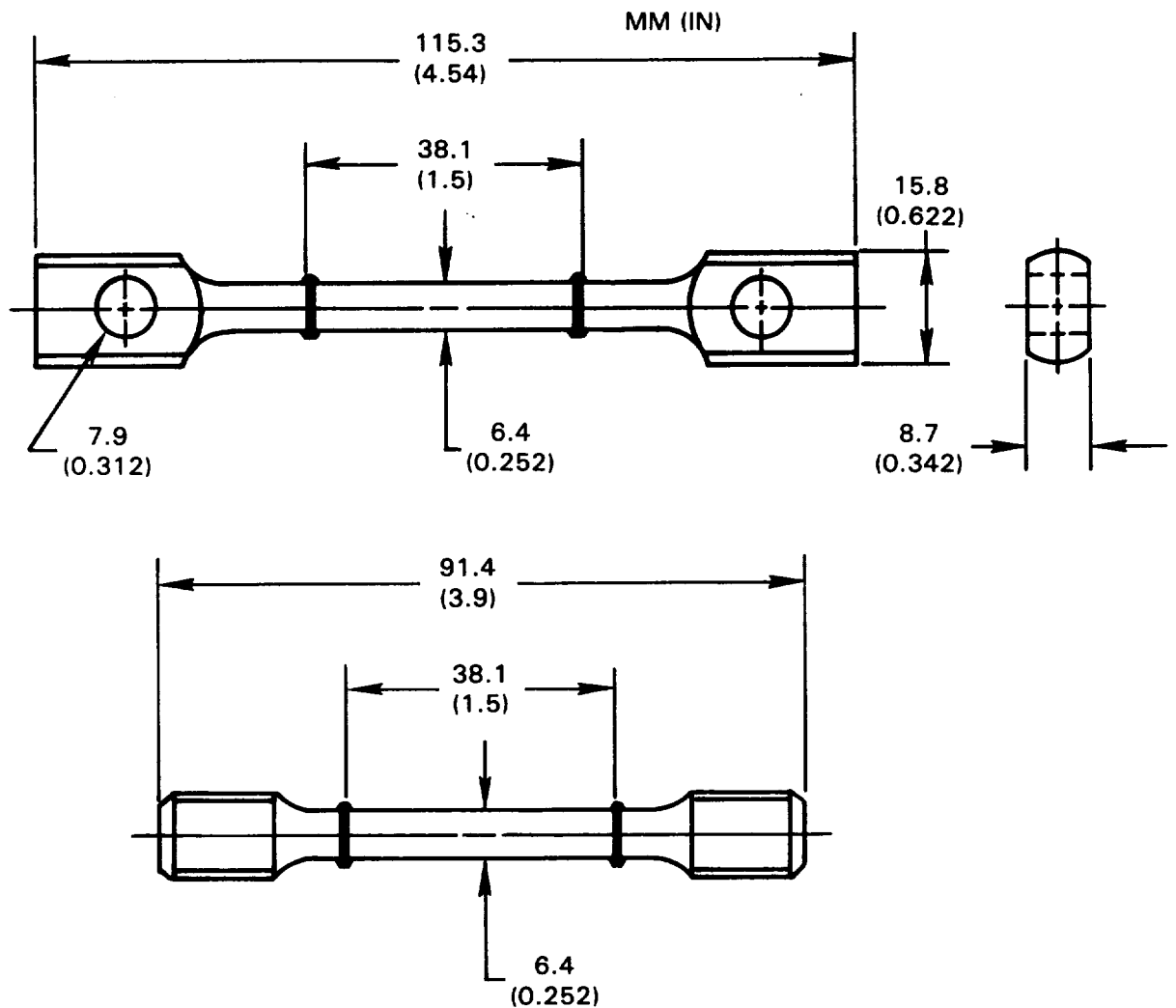
Figure 6 Test Specimens for Monotonic Tensile and Creep Testing

Tensile Tests

A total of 21 monotonic tensile tests were conducted. A summary of all test conditions and observed properties is presented in Table III. A majority of the tests were run at the ASTM standard rate of 0.005 min.$^{-1}$. Several tests were also conducted at 0.0005 min^{-1} to investigate rate effects on the tensile properties. As indicated, a number of tests terminated with fracture occurring outside of the gage section of the specimen. Despite these failures, most of the properties measured early in these tests (e.g., modulus, 0.2% yield) are consistent with results obtained from tests in which failure occurred within the specimen gage section. An examination of these specimens suggested that the tendency to fail outside the gage section is associated

16

Table III

Summary of Tensile Testing

Temp. C(°F)	Spec. ID	$\dot{\epsilon}$ min⁻¹	Ex10⁻³ MPa(KSI)	.2% Yield MPa(KSI)	Ult. MPa(KSI)	Elong %	RA %	Comments
Γ	18A	0.005	187.5(27.2)	714(103.5)	-	4.1[3]	5.9[3]	
50(500)	18B	0.005	169.6(24.6)	702(104.8)	888(128.8)	8.3	10.7	
38(1000)	2A	0.005	149.6(21.7)	727(105)	-	-	-	stopped at 1.5% for ex..
49(1200)	19A	0.005	143.4(20.8)	701(10)		4.7	7.2	
60(1400)	2C	0.005	150.3(21.8)	709( )		-	-	O.G.[1]
	2D	0.005	122(17.7)	721( )	96(115.5)	-	-	O.G.
	38B	0.005	144.1(20.9)	739	-	-	-	O.G.
	650[2]	0.005	157.8(22.9)	709	955(138.5)	8.0	9.1	
	38A	0.0005	122.7(17.8)	77	-	-	-	O.G.
	647	0.0005	146.8(21.3)	70	947(137.4)	7.8	7.6	
71(1600)	19B	0.005	146.9(21.3)		-			stopped at for exam.
	39B	0.005	147.5(21.4)		-	-	-	O.G.
	651	0.005	131(19.0)		792(114.8)	5.7	6.8	
	39A	0.0005	156.5(22.7)		-	-	-	stopped at for exam.
	648	0.0005	146.8(21.3)		780(113.1)	5.7	5.3	
82(1800)	20A	0.005	117.2(17.)	5)	-	-	-	stopped at for exam.
	41B	0.005	111(16.1)	.6)	470(68.1)	6.5	5.0	
	652	0.005	135.8(19)	9.3)	492(71.4)	7.7	8.8	
	41A	0.0005	119.3(1)	0.7)	-	-	-	stopped at for exam.
	649	0.0005	144.1( )	41.1)	471(68.3)	6.5	7.2	
1093(2000)	20B	0.005	101.3	(24.3)	-	-	-	stopped at for exam.

1 fractured outside gage sect..
2 specimens 648 - 652 machine... inch diameter bars
3 within representative scat...

17

with a higher degree of porosity at the thicker ends of each casting as illustrated in Figure 7. To further investigate these failures, a series of specimens was fabricated from 15.9mm(5/8") diameter cylindrical bars. While cast with the same parameters as the previous castings, the cylindrical shape was thought to produce a more uniform distribution of porosity. Six tensile tests were run with these specimens (designated 647 to 652). As shown in the table, the tensile properties are consistent with previous tests and all failures occurred in the specimen gage section.

Comparisons of the 0.2% yield strength and measured static modulus of elasticity vs the anticipated representative scatter in B1900 + Hf are presented in Figures 8 and 9. Representative stress - strain responses at various test temperatures are shown in Figure 10.
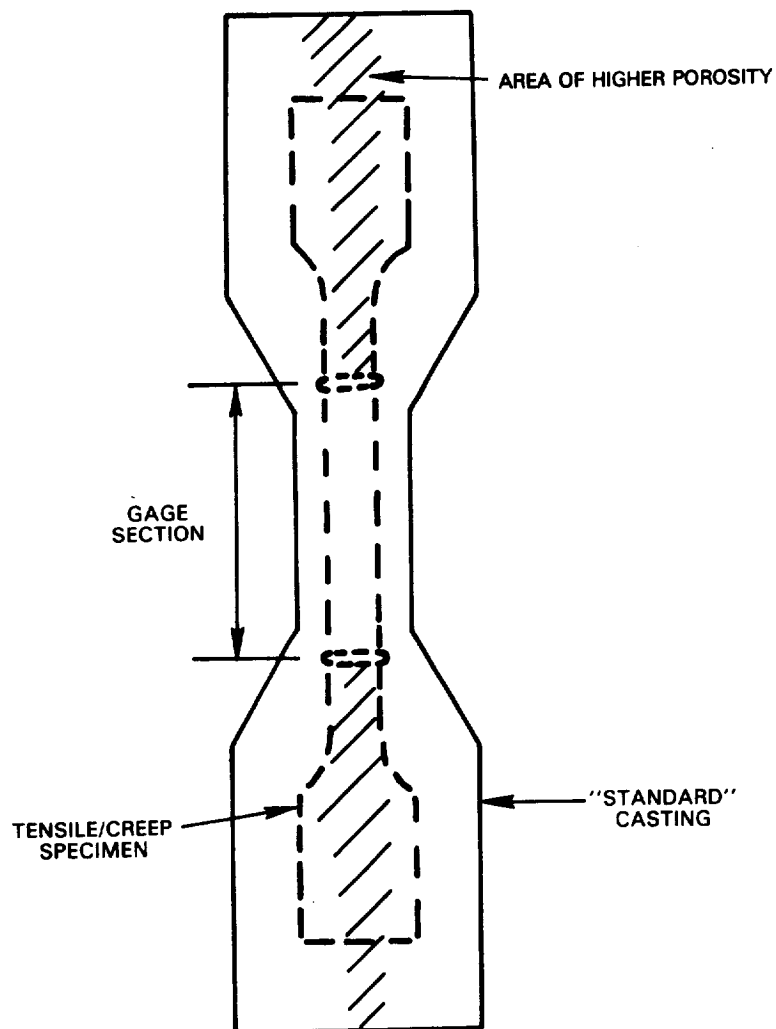
Figure 7 Observed Area of Higher Porosity in As-Cast Bar
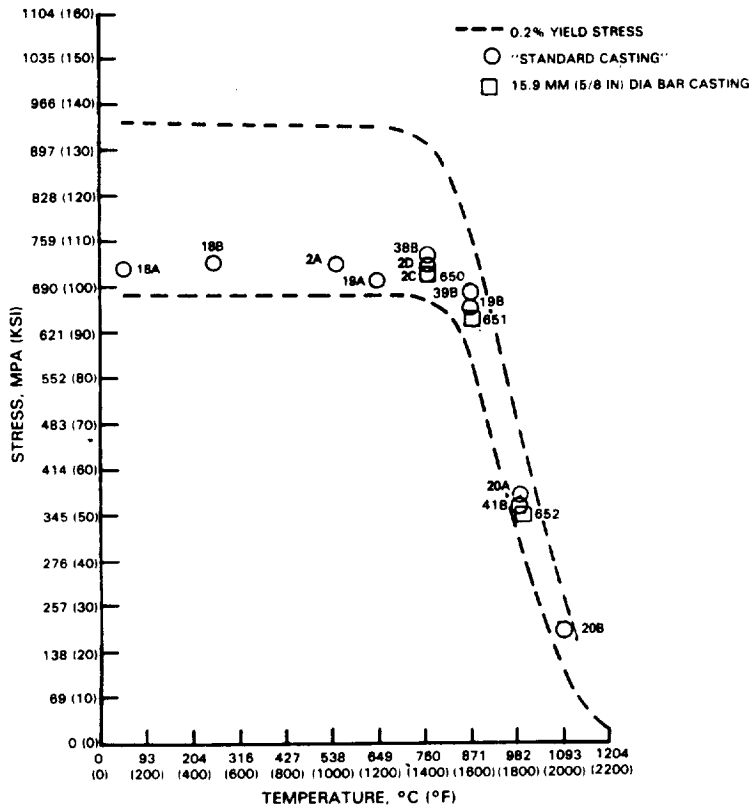
Figure 8   0.2% Yield Stress vs Representative Scatter (B1900+Hf)
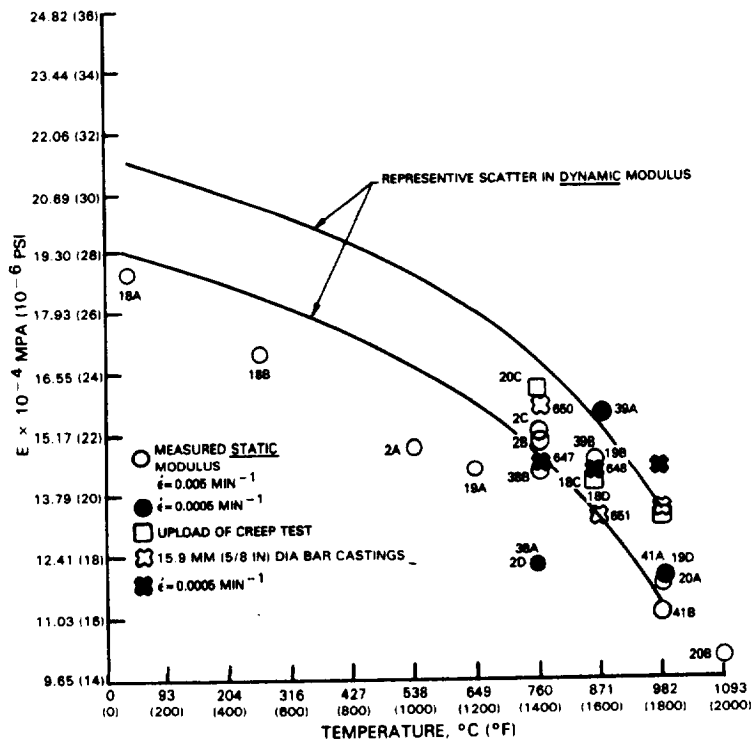
Figure 9   Measured Static vs Dynamic Modulus (B1900+Hf)
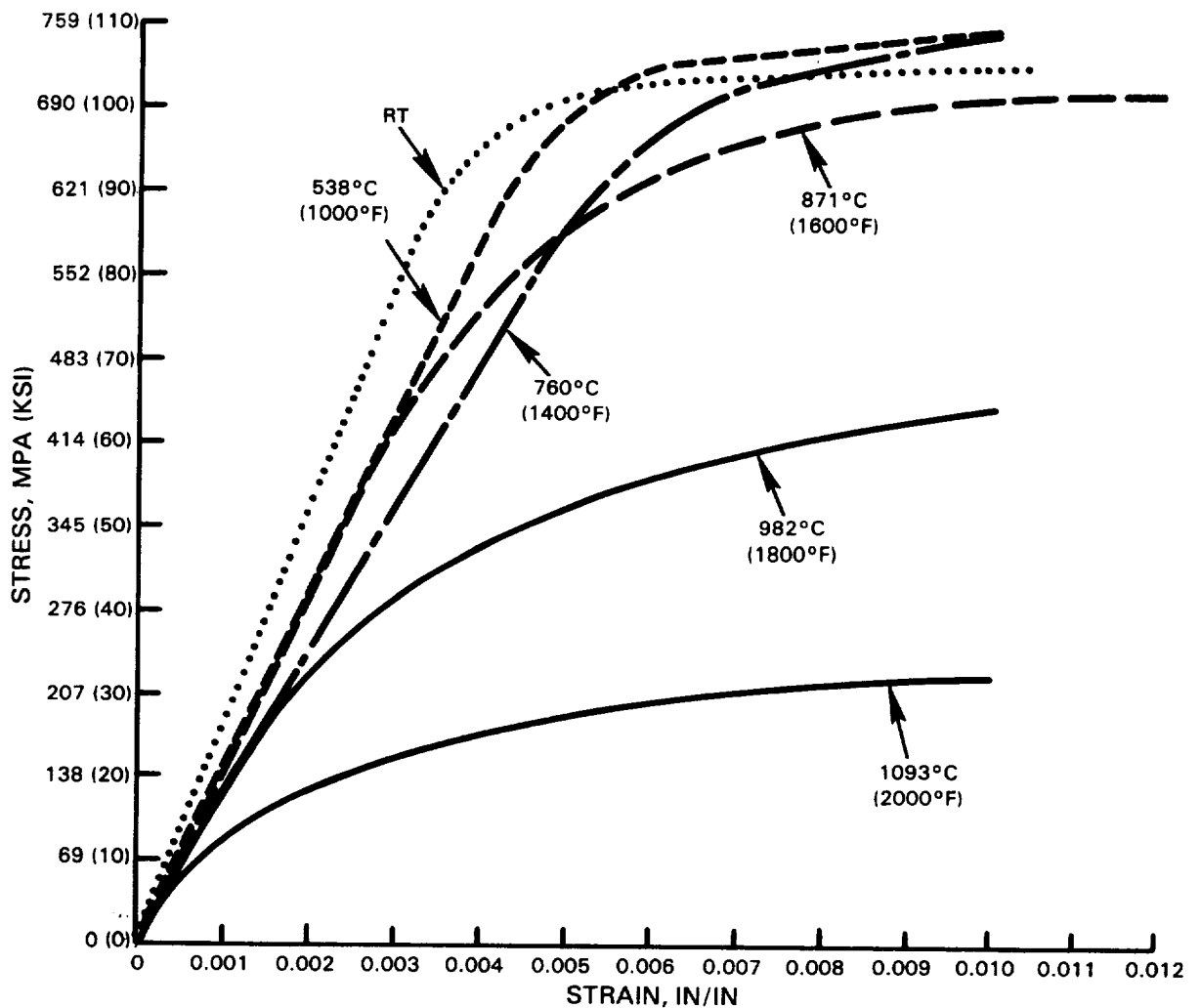
Figure 10   Monotonic Tensile Response - $\dot{\epsilon}$ = .005 min^{-1}

Six specimen tests were terminated at approximately 1 - 1.5% strain for examination to characterize the change in dislocation structure with increasing temperature. As expected, the lower temperature ≤ 871°C (≤ 1600°F) deformation is characterized by inhomogeneous slip as illustrated by the 760°C (1400°F) deformation shown in Figure 11. At higher temperatures, as transition between the inhomogeneous "planar' slip to more homogeneous matrix deformation in the grains is observed. The deformation at 1093°C (2000°F) is shown in Figure 12. A composite for all the temperatures examined at the same strain is presented in Figure 13. Note that microtwins were observed in the latter stages of deformation (≈ 4.5%) at 760°C (1400°F).

20

Figure 11 Planar Deformation at 1400°F

Figure 12 Homogeneous Matrix Deformation at 2000°F

21
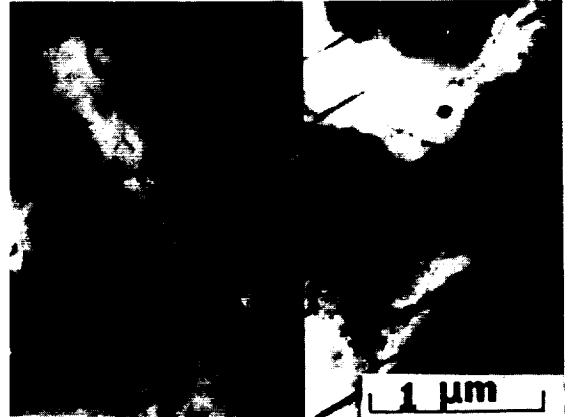
A. 538°C (1000°F), 1.5% STRAIN

B. 760°C (1400°F), 1.3% STRAIN
   760°C (1400°F), 4.5% STRAIN

C. 871°C (1600°F), 1.3% STRAIN

D. 982°C (1800°F), 1.2% STRAIN

E. 1093°C (2000°F), 1.0% STRAIN

TENSILE

Figure 13   Composite TEM Photos of Tensile Tested B-1900 Hf Specimens at Various Temperatures

22

Creep Tests

A summary of the test conditions and observed properties for all monotonic creep tests conducted is presented in Table IV. As indicated, the tests were conducted at four temperatures [649°C (1200°F), 760°C (1400°F), 871°C (1600°F), 982°C (1800°F)] and at stress levels representing 50 to 122% of the bottom of the yield stress scatter band. As shown in Figure 14 the normalized stress ($\sigma / \sigma_{.2\% \text{ YS}}$) reduces the apparent temperature effect for specimens having the same deformation mode, i.e., specimens tested at 871°C (1600°F) and 980°C (1800°F) have similar rupture lives for the same normalized stress and intergrannular failure, while specimens tested at 760°C (1400°F) and 649°C (1200°F) show a significantly longer life for the same, or higher, normalized stress level.

Table IV

Summary of Creep Test Results

Spec- imen	Temp. °C(°F)	Stress MPa(KSI)	% Min. Yield	Frac- ture	Life (Hrs.)	Secondary Creep Rate (Min^{-1})	Elong. %	RA %
19C	982(1800)	234(34)	75	I	20.6	2.5 E-05	6.0	7.8
19D	982(1800)	283(41)	90	I	4.1	0.7 E-04	3.0	2.4
39C	982(1800)	283(41)	90	n.a.	2.9	2.0 E-04	5.5	5.5
41C	871(1600)	283(41)	50	n.a.	441	6.0 E-07	2.6	n.a.
18C	871(1600)	427(62)	75	I	18.2	2.5 E-05	3.2	4.9
40B	871(1600)	427(62)	75	n.a.	20.3	1.5 E-05	2.26	2.7
18D	871(1600)	517(75)	90	I	2.8	1.0 E-04	3.2	5.4
40A	871(1600)	517(75)	90	n.a.	2.5	1.25 E-04	2.3	3.5
59B	871(1600)	586(85)	104	n.a.	0.68	3.85 E-04	2.87	5.04
47D	871(1600)	586(85)	104	n.a.	0.44	7.80 E-04	2.79	n.a.
1	871(1600)	586(85)	104	n.a.	0.24	1.40 E-03	2.72	n.a.
7B	871(1600)	690(100)	122	n.a.	0.082	6.40 E-03	3.00	2.40
7C	871(1600)	690(100)	122	n.a.	0.047	1.54 E-02	3.22	n.a.
40B	871(1600)	690(100)	122	n.a.	0.035	1.25 E-02	1.97	n.a.
59?	760(1400)	600(87)	90	n.a.	38.5	2.64 E-06	1.47	2.41
20C	760(1400)	600(87)	90	T	134.8	n.a.		3.1
20D	760(1400)	669(97)	100	T	30.2	7.9 E-06	2.9	9.4
39D	760(1400)	669(97)	100	n.a.	49.8	7.5 E-05	3.78	5.9
602	649(1200)	690(100)	102	n.a.	1958.7	1.18 E-07	1.10	1.60

I = Intergranular
n.a. = Not Available
T = Transgranular

Examination has shown that at the higher temperatures [871°C (1600°F) and 982°C (1800°F)] the specimens failed in an intergranular cracking mode, while the specimens tested at 760°C (1400°F) showed a greater tendency for transgranular cracking (see Figures 15 through 18). Substantial differences in the grain dislocation structure were also observed. In specimens tested at 932°C (1800°F) and 871°C (1600°F) (Figures 19 and 20), dislocation networks surrounding the gamma prime (γ') particles are the dominant features. This is an indication of a loss of coherency of the γ' and the matrix. At 760°F (1400°F), no dislocation network is observed; instead short segments of dislocation and microtwins (similar to the tensile tests) are inhomogeneously dispersed throughout the grains. The presence of the microtwins at this temperature may account for the tendency of cracks to progress in a transgranular manner.

A comparison of the percent elongation observed in several of the specimens during the monotonic tensile and creep testing is presented in Figure 21. As indicated, the creep elongation is generally smaller than the tensile elongation.
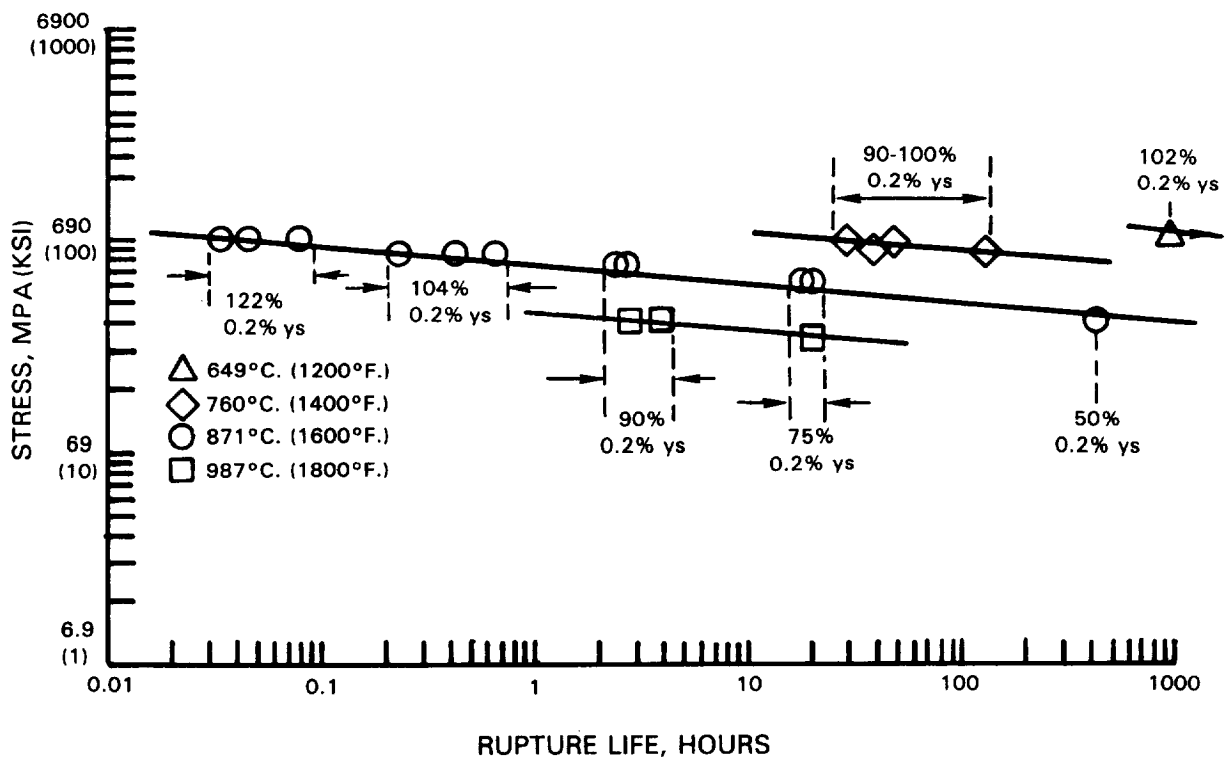
Figure 14   Variation of Creep Rupture Life with Stress

24
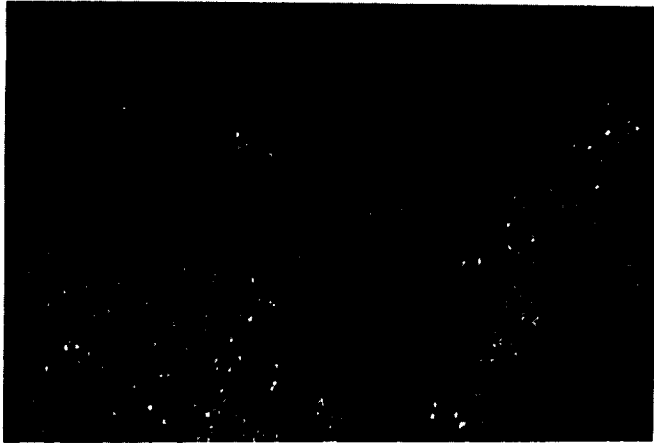
CREEP
FRACTURE MODE

982°C/283 MPA
(1800°F/41 KSI)

871°C/517 MPA
(1600°F/75 KSI)

↑ INTERGRANULAR

↓ TRANSGRANULAR
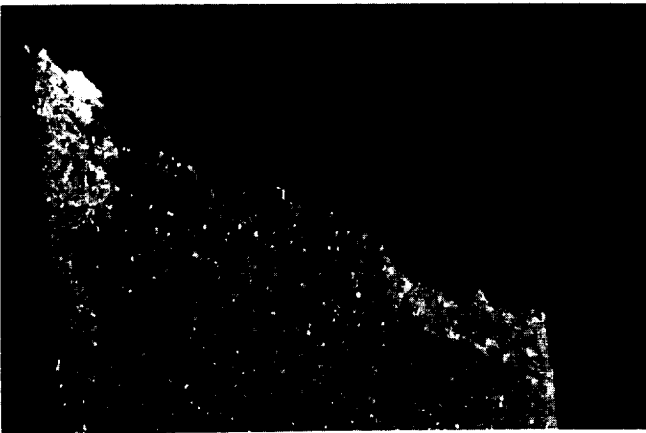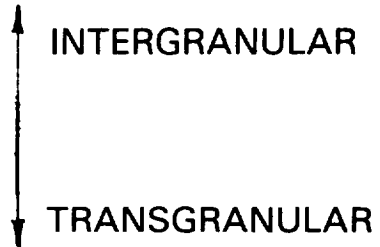
760°C/600 MPA
(1400°F/87 KSI)

Figure 15 Creep Fracture Modes
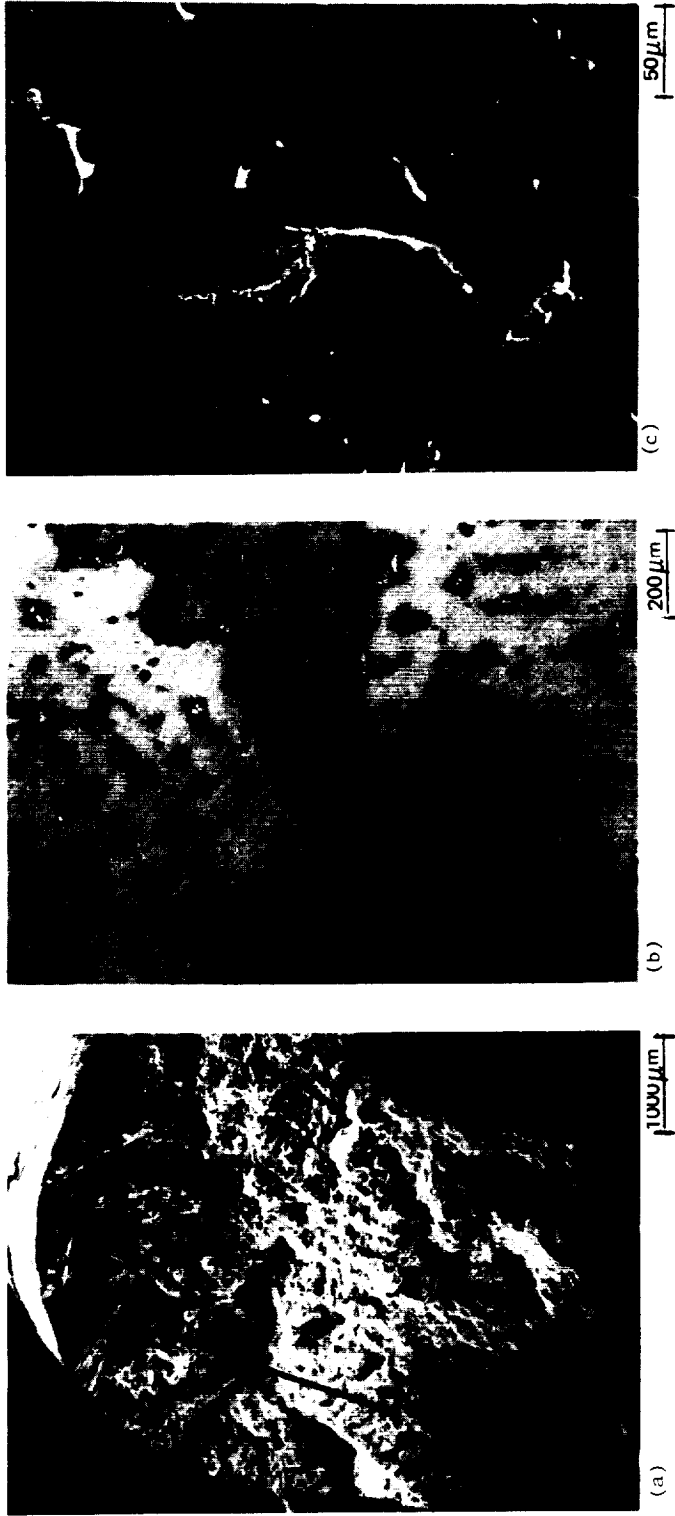
Figure 16 Specimen 19C After Being Creep Tested at 982°C/234 MPa
(1800°F/34 ksi) for 20.6 Hours. (a) Heavily oxidized fracture
surface (b) Longitudinal section along line AA' showing
intergrannular fracture by optical microscopy (c) Longitudinal
section along line AA' showing intergrannular fracture by SEM.
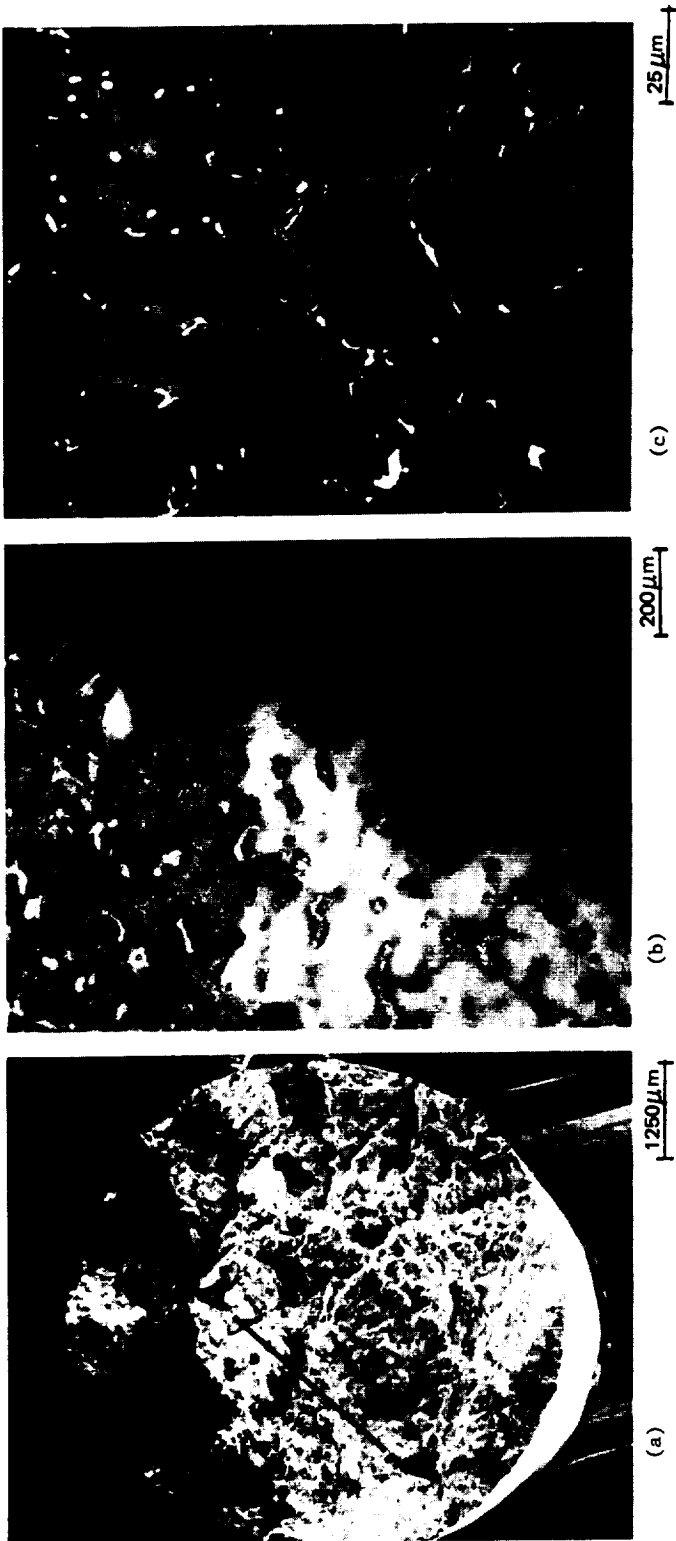
Figure 17 Specimen 18C After Being Creep Tested at 871°C/427 MPa (1600°F/62 ksi) for 18.2 Hours. (a) Heavily oxidized fracture surface (b) Longitudinal section along line AA' showing intergrannular fracture by optical microscopy (c) Longitudinal section along line AA' showing intergrannular fracture by SEM.
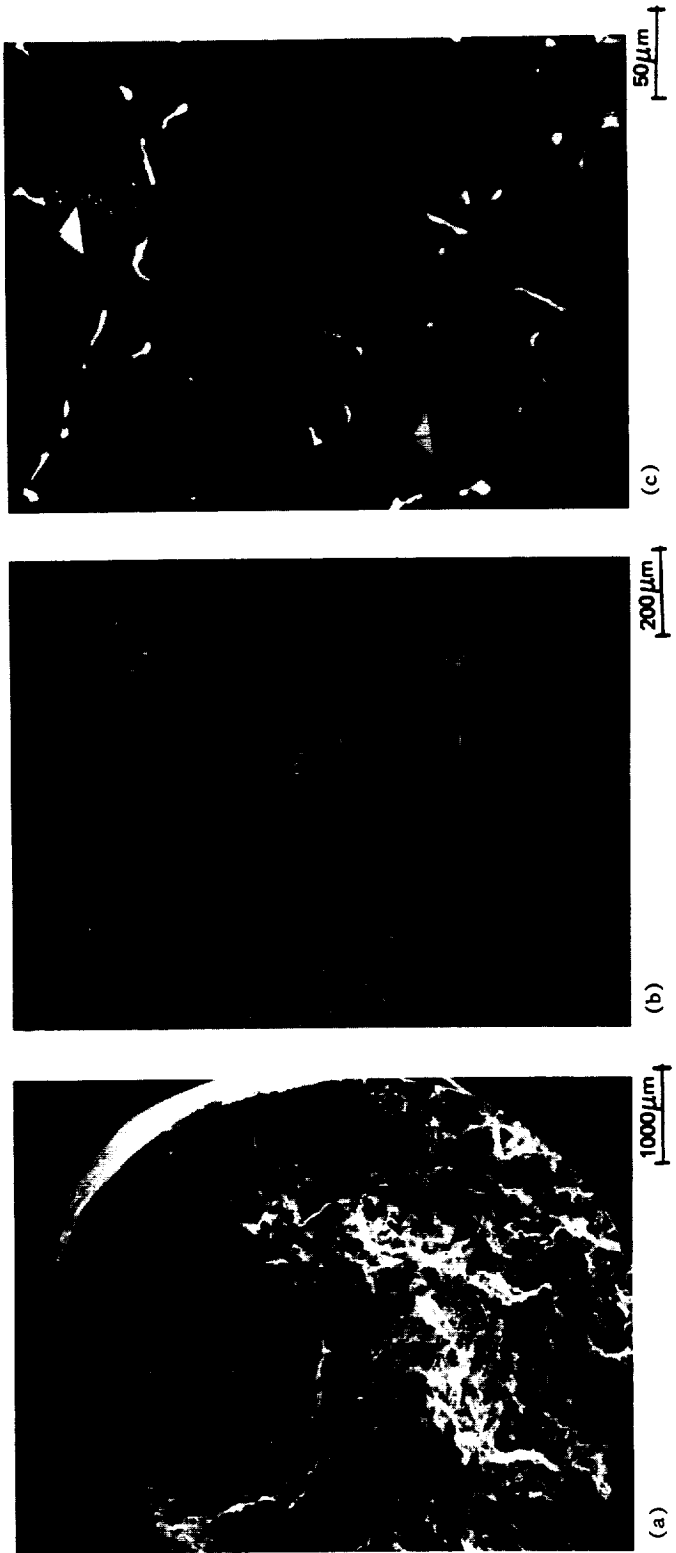
Figure 18 Specimen 20C After Being Creep Tested at 760°C/600 MPa
(1400°F/87 ksi) for 134.8 Hours. (a) Heavily oxidized fracture
surface (b) Longitudinal section along line AA' showing
intergrannular fracture by optical microscopy (c) Longitudinal
section along line AA' showing no indication of intergrannular
fracture by SEM.

Figure 19 Dislocation Networks Surrounding Gamma Prime Indicate Loss of Coherency Between γ/γ'. (a) Specimen 19C After Being Creep Tested at 982°C/234 MPa (1800°F/34 ksi) for 20.6 Hours. (b) Specimen 19D after being creep tested at 982°C/283 MPa (1800°F/41 ksi) for 4.1 hours.
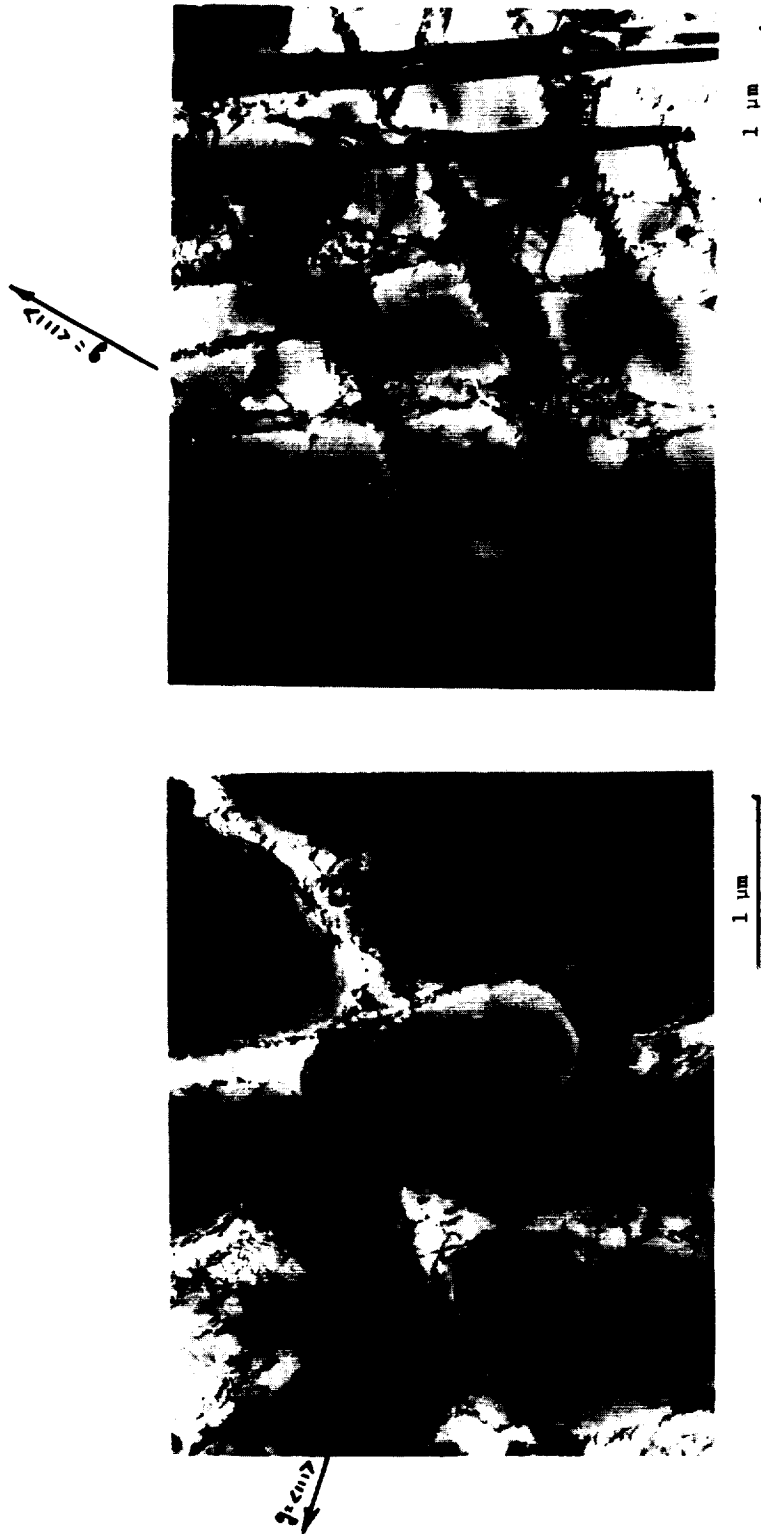
Figure 20 Dislocation Networks Surrounding Gamma Prime Indicate Loss of
Coherency Between γ/γ'. (a) Specimen 18C After Being Creep Tested
at 871°C/427 MPa (1600°F/62 ksi) for 20.6 Hours. (b) Specimen 20C
after being creep tested at 760°C/600 MPa (1400°F/87 ksi) for 134.8
hours. Dislocation segments and microtwins are the characteristic
features.
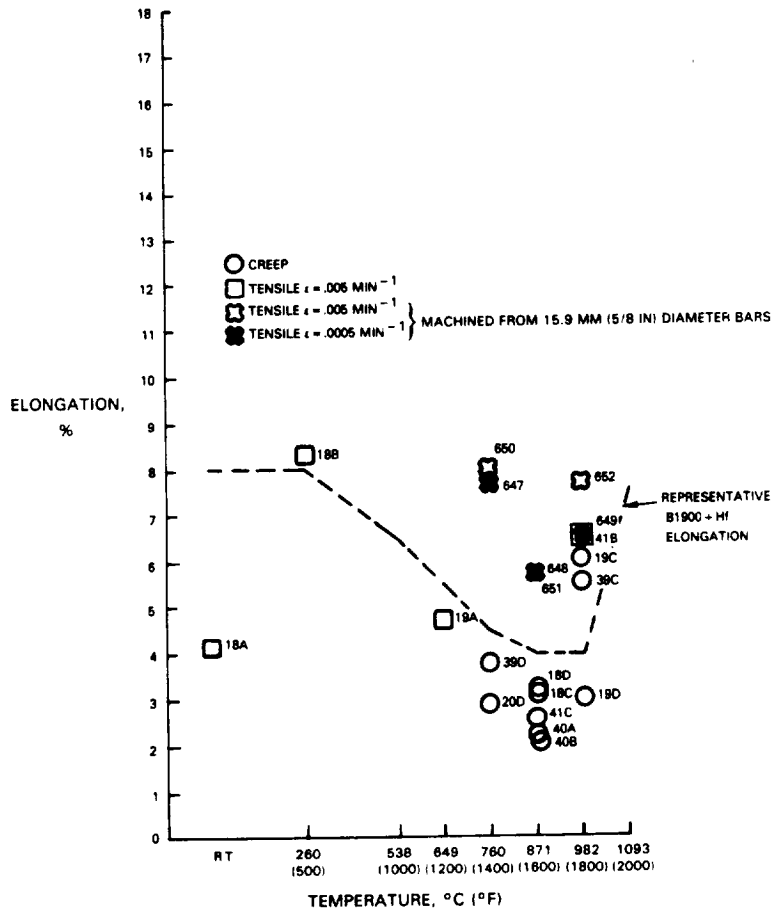
Figure 21 Elongation Observed in Tensile and Creep Tests

3.1.4 Fatigue Specimen Design, Fabrication and Test Facility

The three axial, strain control specimen designs used in the initial fatigue testing are shown in Figure 22. Type A has integral, large extensometer ridges; type B has integral "mini" ridges; and type C is a smooth cylindrical gage section design. An initial group of 18 specimens was fabricated to investigate machining and geometry effects on fatigue life. Six type A specimens were electrochemically ground and six each of types B and C were centerless ground from "standard" B1900 + Hf castings (see Figure 1A). All specimens were then electrochemically polished. Fully reversed, strain controlled fatigue tests were conducted at:

871°C (1600°F), $\Delta\epsilon = \pm\ 0.25\%$, $\dot{\epsilon} = 1.67$ E-03 s^{-1}

538°C (1000°F), $\Delta\epsilon = \pm\ 0.25\%$, $\dot{\epsilon} = 1.67$ E-03 s^{-1}

31
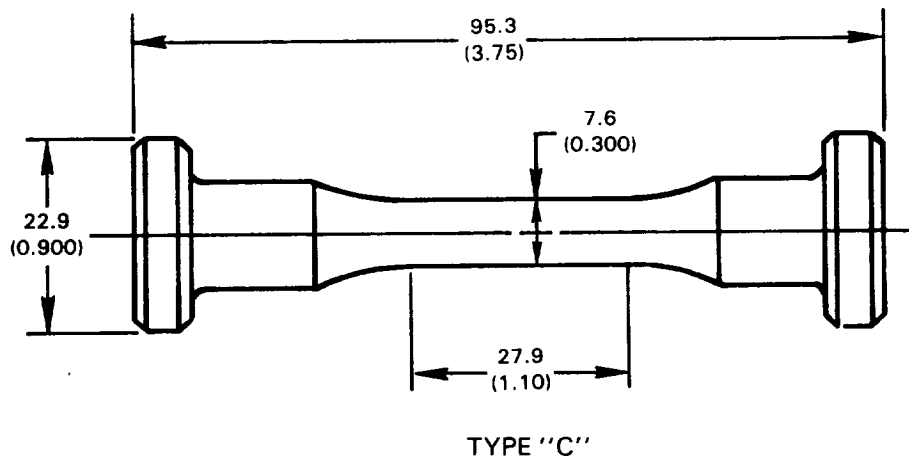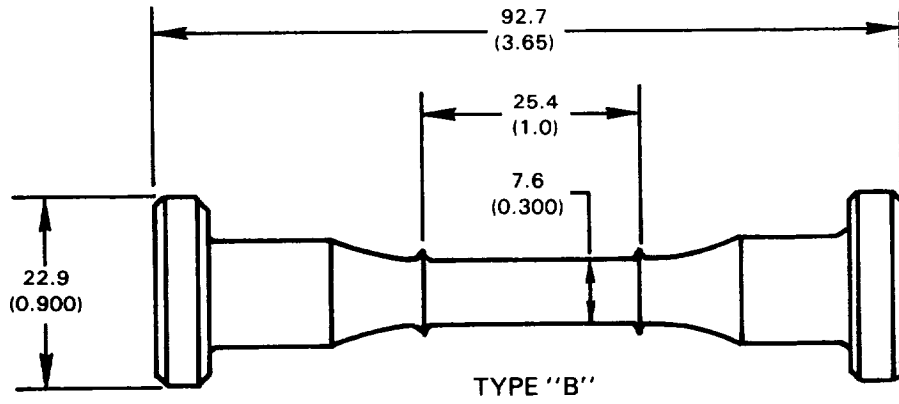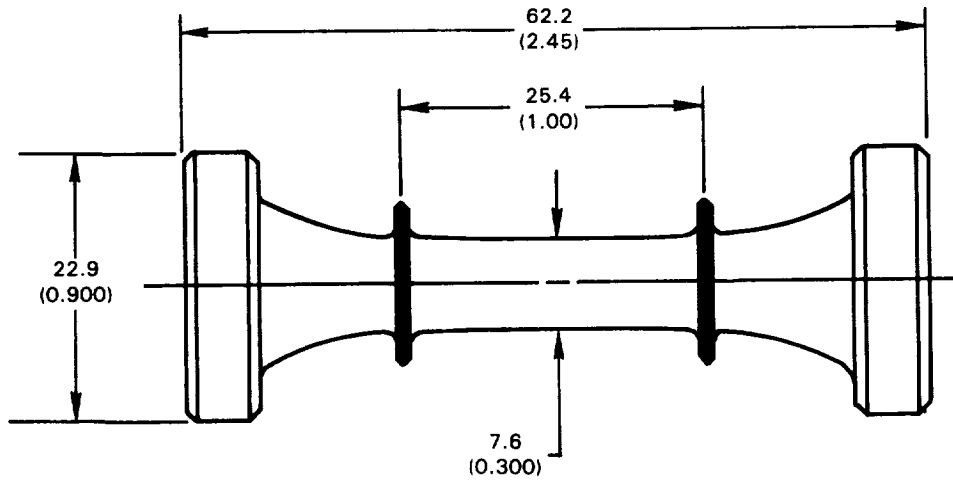
Figure 22   Fatigue Specimen Geometries for Initial Testing

Both total specimen cyclic life and failure location were recorded. Two
specimens were subsequently eliminated from the study because of testing
problems. A Weibull analysis of the data, presented in Figure 23, shows that
the 871°C (1600°F) data for each specimen type is uniformly distributed,
indicating little effect of geometry or machining procedure at this
temperature. Primary failure locations occurred throughout the gage section
for all specimens tested. However, at 538°C (1000°F), the type C data are
grouped at the higher end of the distribution. Furthermore, the type A and B
failure locations were predominantly associated with the extensometer ridge
fillets, whereas the type C failures generally occurred throughout the gage
section. These results suggest a fillet or "notch" effect in the fatigue life
at the lower temperature. The distribution of the type A and B tests also
suggests that the machining procedure (ECG vs CG) has little effect on fatigue
life at these conditions.
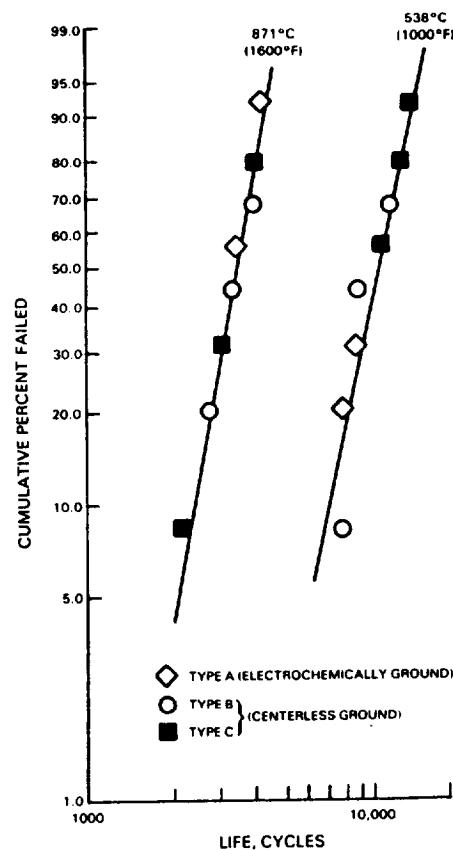
Figure 23   Weibull Analysis of Initial Fatigue Data to Investigate Geometry
and Machining Effects

33

Further investigation using X-ray diffraction to measure residual surface stresses produced by both processes resulted in similar average stress levels, but significant amounts of scatter were observed in the measurements. The X-ray diffraction (XRD) technique is successfully used on fine grain (wrought) materials; however, application to a cast material, which has a relatively larger grain size, results in fewer grains being sampled by the incident X-ray beam, and thus, much more scatter in the stress measurements. Data taken on several B1900 + Hf specimens machined using centerless grinding and electrochemical grinding is shown in Figure 24. For comparison, measurements taken on fine grain (wrought) IN 718 material show considerably less scatter, with centerless grinding producing a slightly larger compressive stress.

A second group of specimens was fabricated with the type B geometry using centerless grinding and a light [< .025mm(<0.001 in.) removal on a diameter] electropolish. The cyclic lives of these specimens, tested at the same conditions, showed similar trends to the previous data. Subsequent specimens were fabricated to the type C geometry in order to eliminate the notch effect at lower temperatures using centerless grinding and a light electropolish.
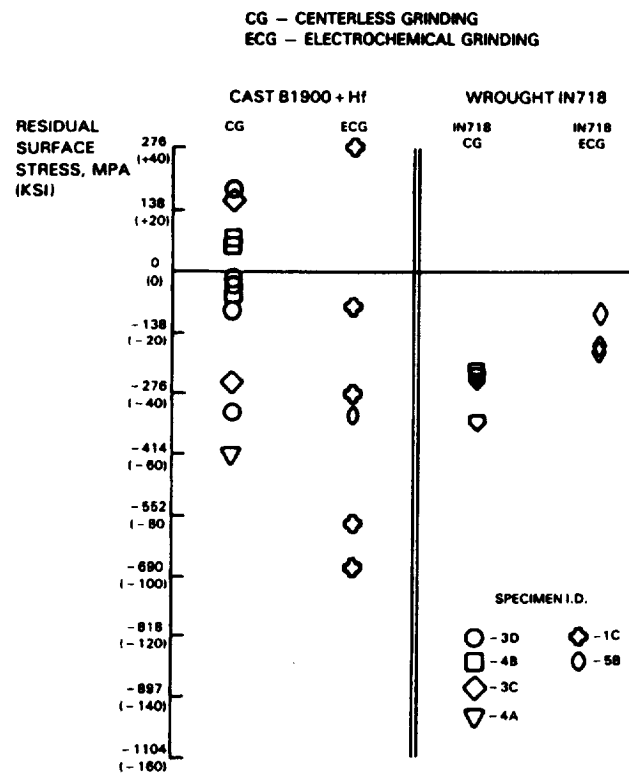
Figure 24 Residual Stresses Measured by X-Ray Diffraction

34

The test facility used for the isothermal fatigue tests included a servo-controlled, closed loop hydraulic testing machine with MTS controllers, a 7.5 kw - 10khz Tocco induction heater, and an Ircon infrared radiation pyrometer for temperature measurement. Induction heating was selected to facilitate setup and inspection of the many fatigue tests. The Ircon pyrometer is used to measure temperatures above 760°C (1400°F); below this temperature, a thermocouple monitored specimen temperature. Axial strain measurement was accomplished with an MTS extensometer. The quartz rods which define a one-inch gage section are spring loaded against the specimen and did not show any signs of slippage during testing. A typical test setup is illustrated in Figure 25.
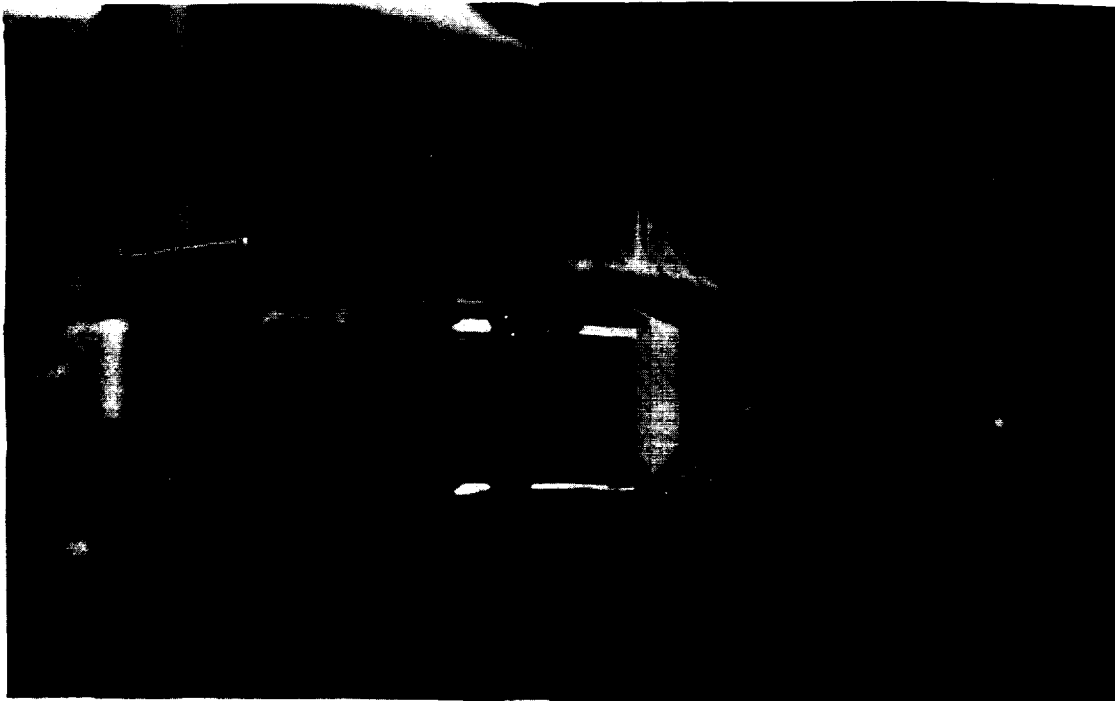
Figure 25 Typical Test Setup for Isothermal Fatigue Testing

3.1.5 Baseline Fatigue Testing

Isothermal, strain controlled fatigue tests were conducted to define the crack initiation life of B1900 + Hf material and to provide a baseline for life prediction model evaluation. Testing was limited to key variables relevant to the general creep fatigue life prediction problem. A general matrix of the tests is presented in Figure 26 and includes strain range ($\Delta \epsilon$), strain rate,

strain ratio ($R\epsilon$), dwell periods and temperature. All of the tests conducted for the base program are summarized in Appendix I. Those tests conducted at a strain rate of 1.67 E-03 sec^{-1} represent the upper limit of rates tested and are considered to be fast enough to preclude a significant creep fatigue effect. Representative hysteresis loops from 871°C (1600°F) tests conducted at strain ranges of 0.5% and 0.8% indicate a small amount of inelastic strain relative to the total strain range (Figures 27 and 28). A review of the cyclic response histories of the $R\epsilon$ = -1 tests indicates that at 871°C (1600°F) a small amount of cyclic softening occurs, while at 538°C (1000°F) cyclic hardening is observed at the larger strain ranges. The representative inelastic strain ratio of four specimens and the range of values for all specimens tested at the same conditions are presented in Figures 29 and 30.

TEST CONDITION	STRAIN RANGE			STRAIN RATIO			STRAIN RATE			DWELL PERIODS						TEMPERATURES			
	$\Delta\epsilon_1$	$\Delta\epsilon_2$	$\Delta\epsilon_3$	$-\infty$	-1	0	$\dot\epsilon_1$	$\dot\epsilon_2$	$\dot\epsilon_3$	ϵ_{MAX} t_1	t_2	ϵ_{MIN} t_1	t_2	ϵ_{INT} t_1	t_2	T_1	T_3	T_4	T_5
1	X				X		X											X	
2		X			X		X											X	
3			X		X		X											X	
4	X				X		X											X	
5			X		X		X											X	
6	X				X				X									X	
7			X		X				X									X	
8	X				X			X											X
9			X		X			X											X
10			X		X		X												X
11	X				X			X									X		
12			X		X			X									X		
13	X				X			X								X			
14			X		X			X								X			
15		X			X			X		X								X	
16		X			X			X				X						X	
17		X			X			X					X					X	
18			X		X			X				X							X
19			X		X			X						X					X
20		X				X		X											X
21		X		X				X											X

Figure 26 Test Matrix for Baseline Fatigue Tests
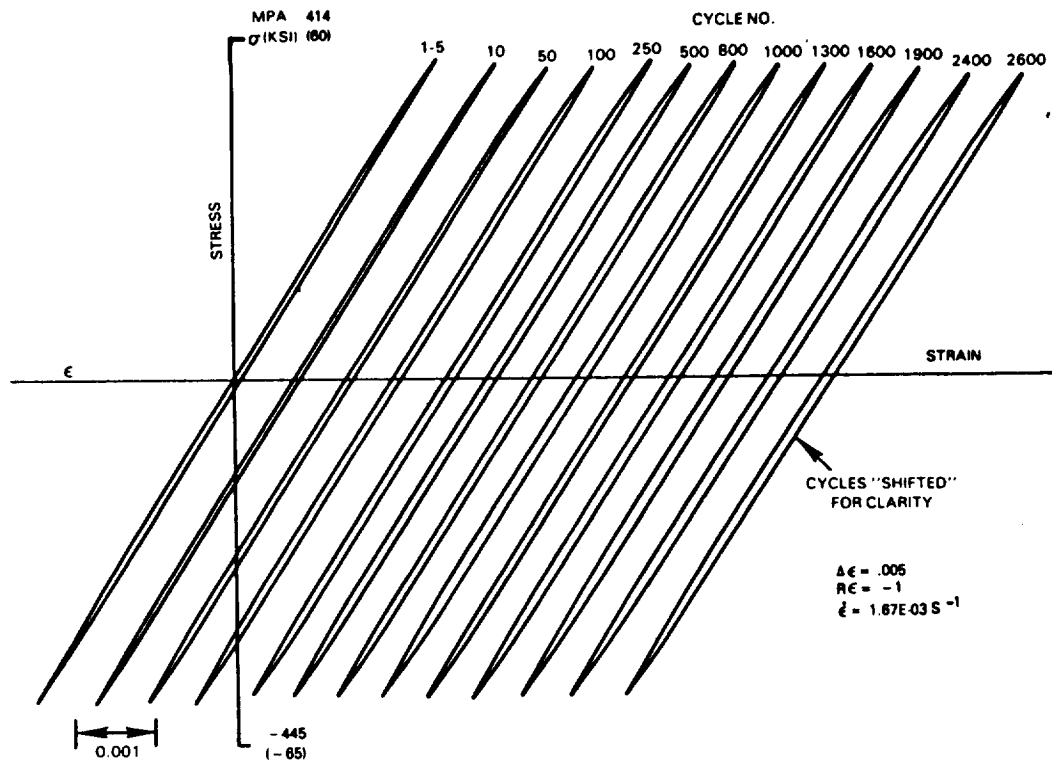
Figure 27   Cyclic Response of 871°C (1600°F) Fatigue Test with $\Delta\epsilon = \pm$ .25%
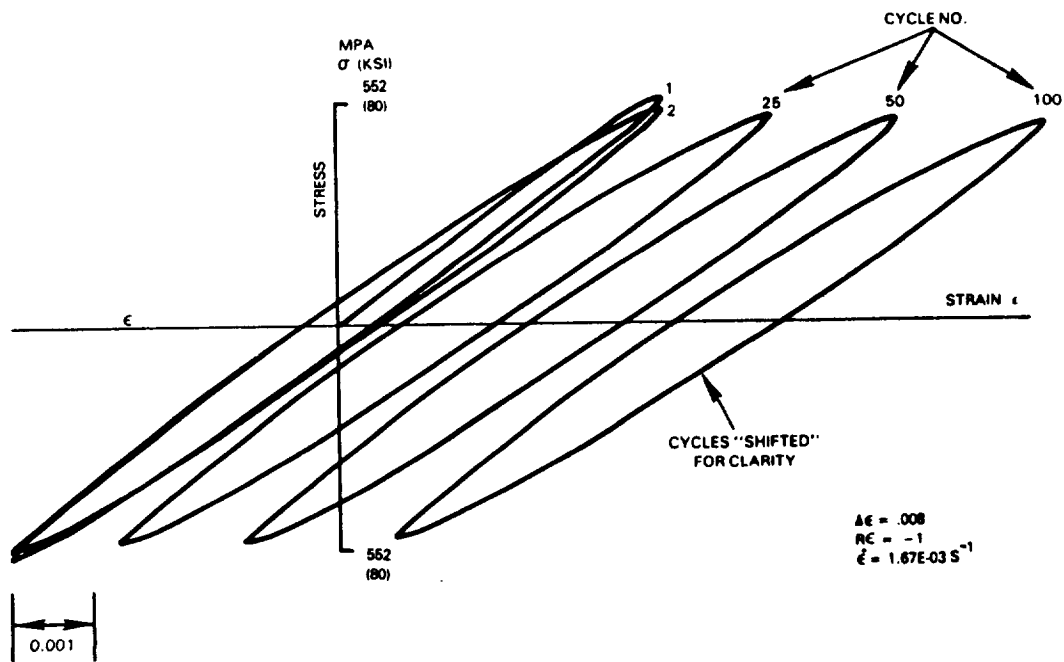
Figure 28   Cyclic Response of 871°C (1600°F) Fatigue Test with $\Delta\epsilon = \pm$ .4%
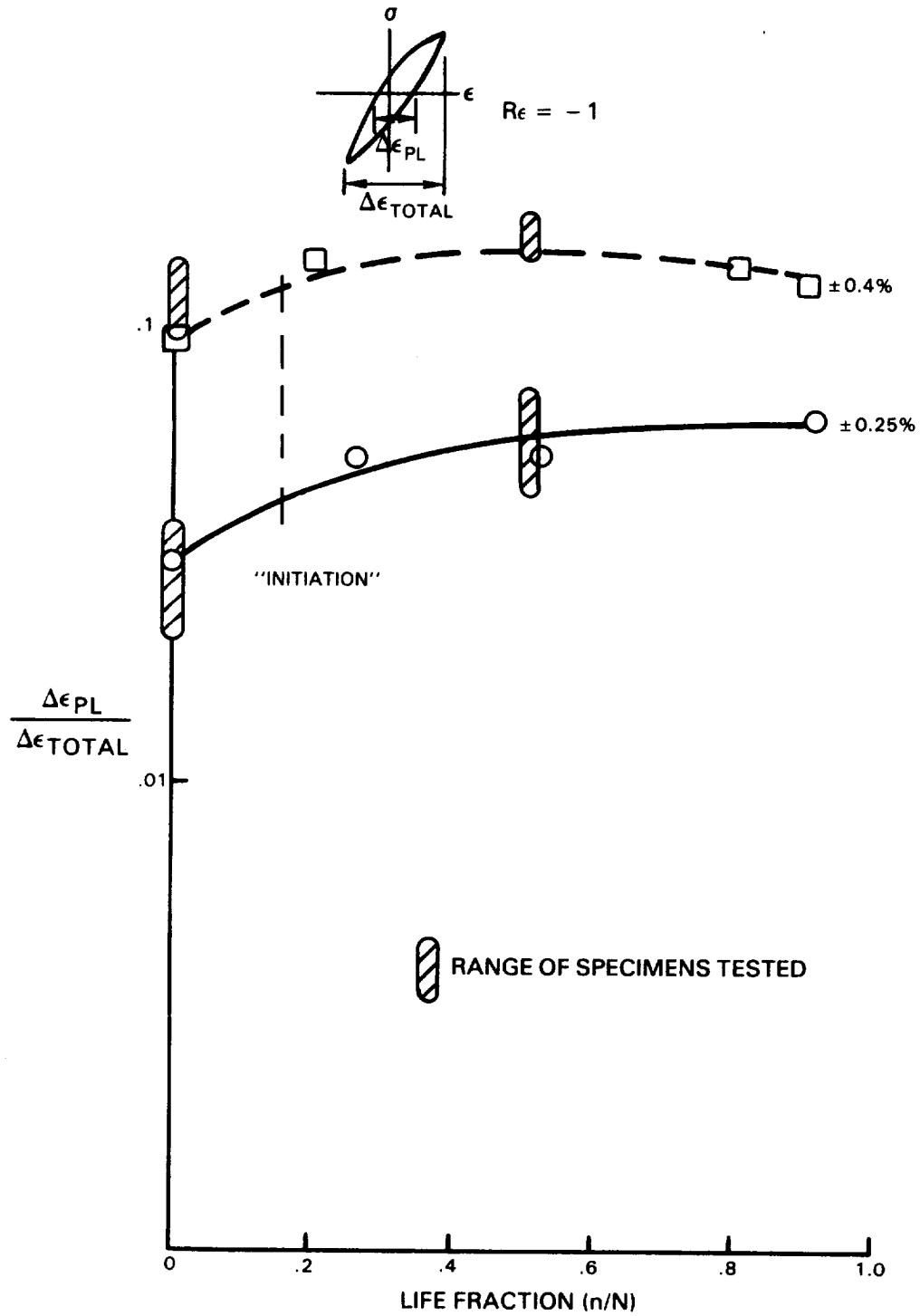
Figure 29 Inelastic Strain Ratio for 871°C (1600°F) Fatigue Tests
($\dot{\epsilon}$ = 1.67 E-03 S^{-1})
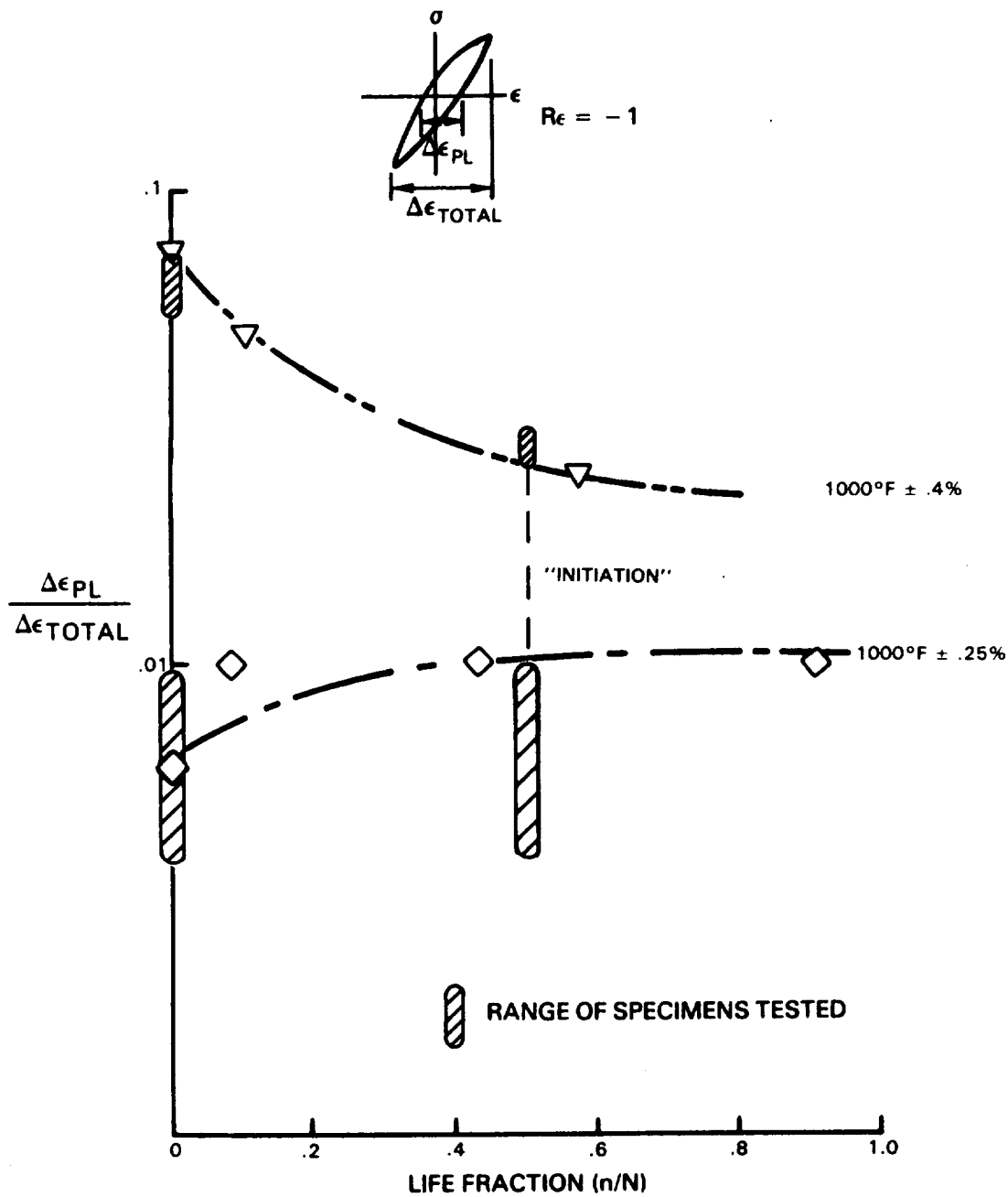
Figure 30 Inelastic Strain Ratio for 538°C (1000°F) Fatigue Tests
($\dot{\epsilon}$ = 1.67 E-03 S^{-1})

For each specimen test, the crack initiation life was defined by three
methods; (1) total separation of the specimen, (2) cycles to 5% and 10% stress
amplitude drop from the steady state values, and (3) first indication of
cracking.

The first indication of cracking was established based on inspection of a number of specimens during testing. At each inspection, an acetate replica of the gage section was taken and examined to determine the number and size of surface cracks. In those tests where multiple cracks were observed, the crack that ultimately led to specimen failure was tracked throughout the life. At least one specimen was inspected for each condition shown in Appendix I. A summary of the fully reversed data based on the longest observed crack at each inspection is presented in Figure 31. General observations include the fact that measurable cracks 0.13 - 0.26mm (.005 - .010-in) appear earlier (based on percentage of separation life) and have faster growth rates at the higher temperatures. Specific details associated with each test type are discussed in Section 3.3.

During the initial life model evaluations, crack initiation was defined as the generation of a 0.76mm (0.030-in) surface crack. Inspection of several fatigue fracture surfaces has shown that the assumption of a semicircular crack to estimate crack depth is reasonable for surface crack lengths to $\approx$ 2.5mm ($\approx$0.100 in.). Thus, the 0.76mm (0.030-in) surface length represents a 0.38mm (0.015 in) depth crack as compared to a material grain size of 0.18 - 0.25mm (0.007 - 0.010 in) (see Section 3.2.1).

The original eighteen fatigue specimens, used to investigate geometry and machining effects on fatigue life, were also examined to determine the location of the primary failure initiation sites and the mode of cracking. All specimens were found to have surface initiated fatigue cracks associated with either carbides and/or porosity. Two representative specimens and failure sites, as identified by SEM and microprobe analysis, are presented in Figures 32 and 33. Failure sites determined to have a high tantalum (Ta)content or other constituents found in the grain boundary carbides were identified as carbide related failures. Failure sites having a chemical composition similar to the matrix, and where a pore could be observed, were identified as porosity related failures. Analysis of the specimen life data (Figure 34) suggested that the nature of the initiation site (carbide vs porosity) is not statistically significant in determining the fatigue life. Based on this result, carbide or porosity initiation was not considered a primary variable in the analysis of subsequent fatigue tests.

40
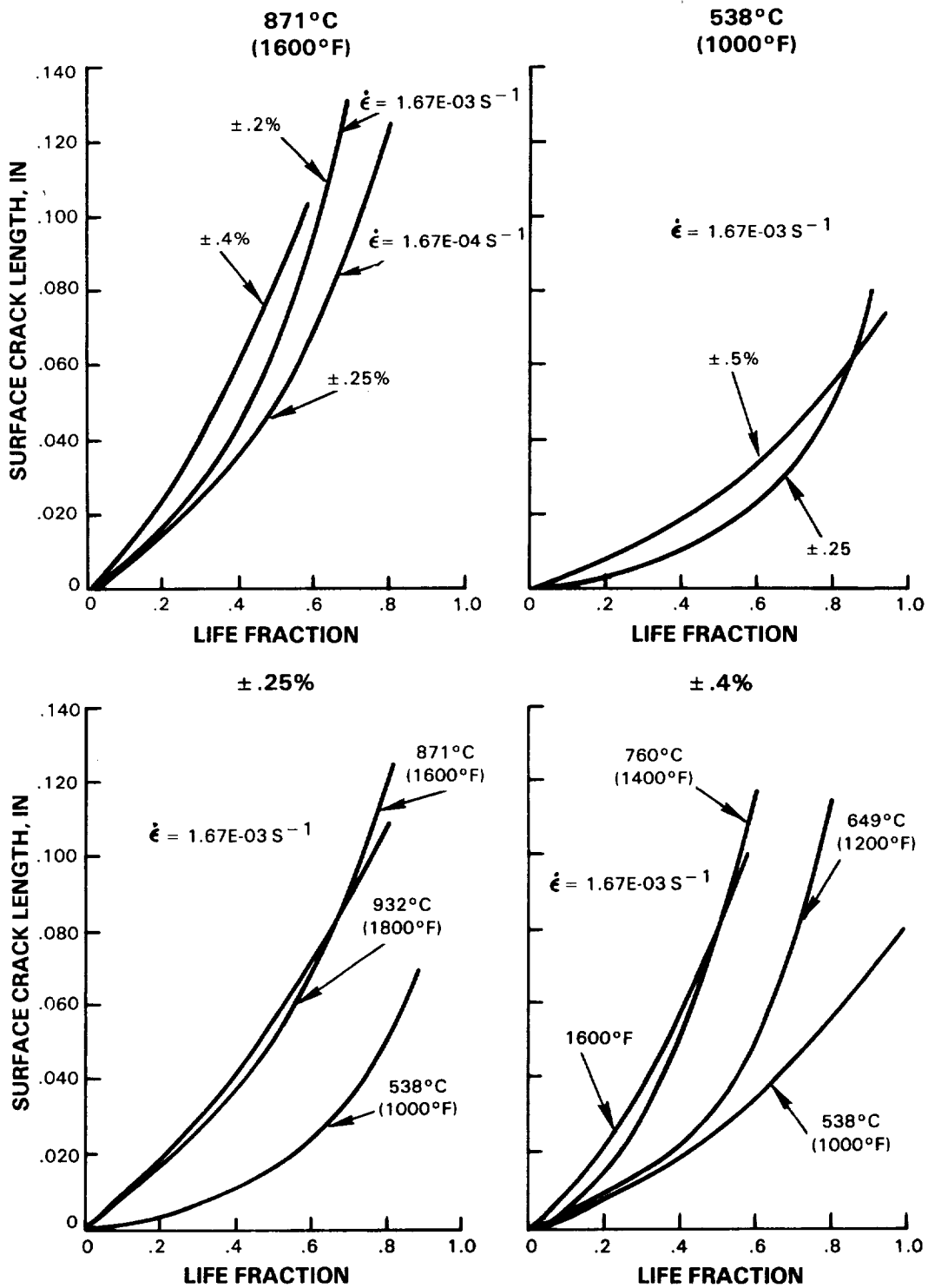
Figure 31 Summary of Specimen Replica Measurements

(b)

(a)
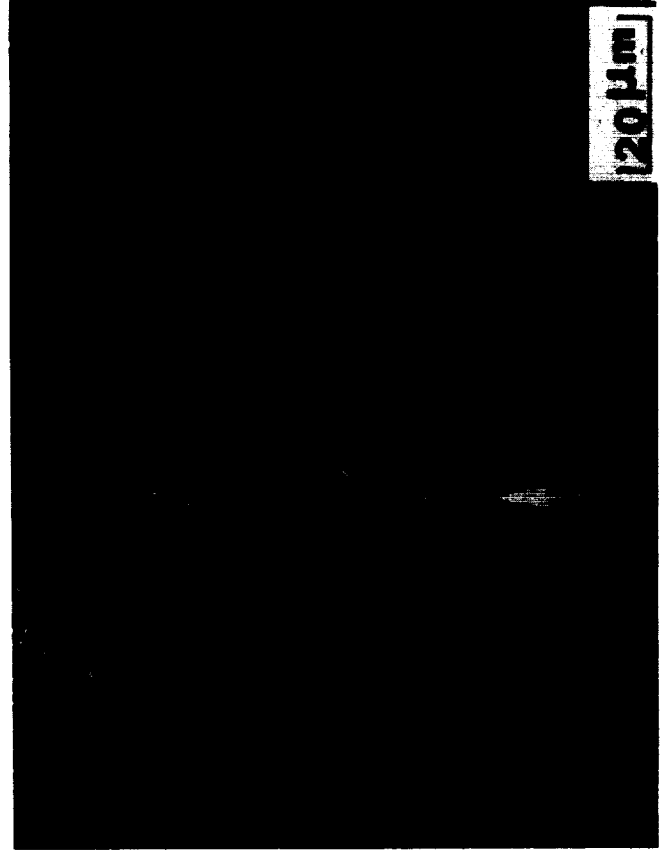
(c)

Figure 32   Fracture Surface of Specimen 6D After Being
Tested at 871°C (1600°F) $\Delta\epsilon_t = \pm 0.25\%$,
10cpm for 2965 Cycles.

(a) Typical fractographs showing two crack
    initiation sites A and B

(b) Carbide on surface at primary crack
    initiation site (A) is shown by arrow.

(c) X-ray map showing the distribution of Ta
    in area corresponding to (B)

42

Figure 33 Fracture Surface of Specimen 4D After Being Tested at 538°C (1000°F) $\Delta\epsilon_t = \pm 0.25\%$, 10cpm for 12,560 Cycles.

(a) Typical fractographs showing crack initiated on surface

(b) Porosity on surface at crack initiation site

(c) Faint fatigue striations along with secondary cracks

43
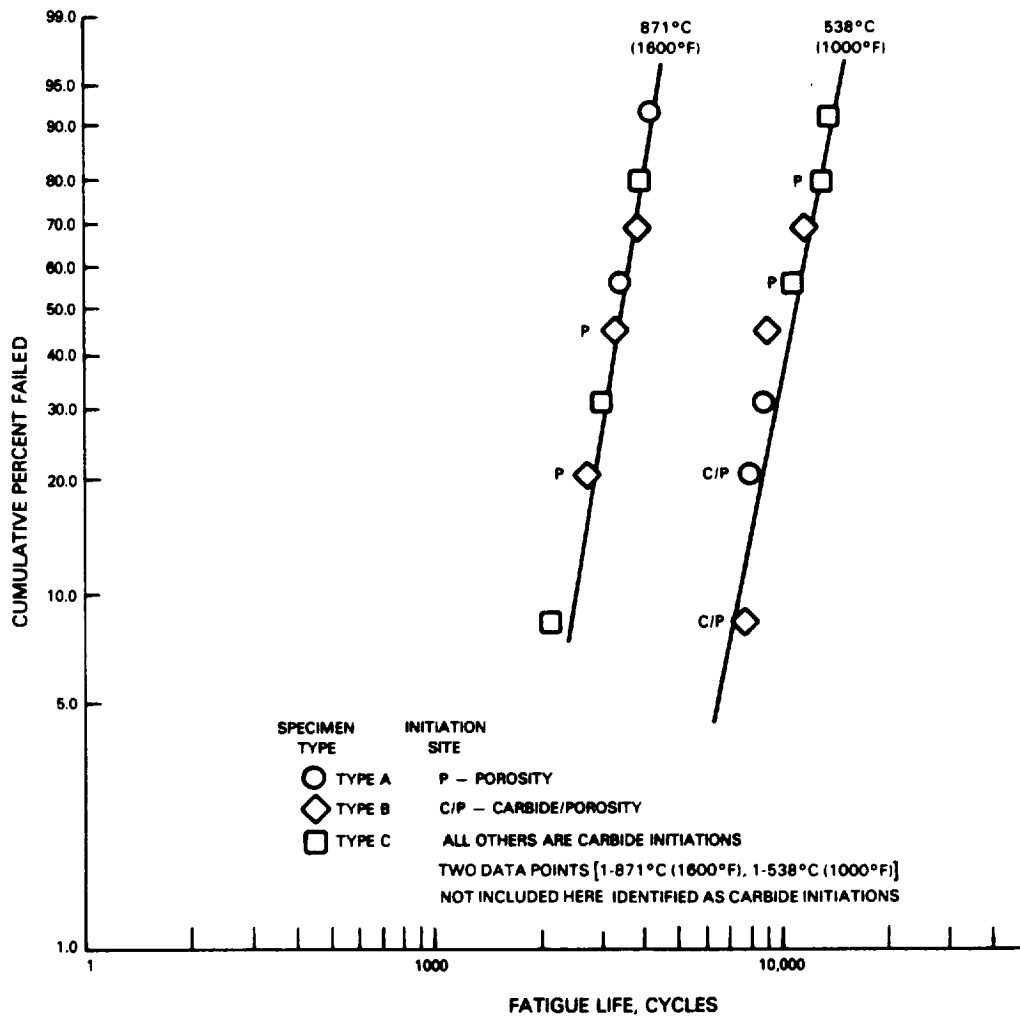
Figure 34 Distribution of Initiation Sites for Initial Fatigue Tests

In order to clearly identify the process of crack growth from the initiation site to the 0.38mm(0.015 in.) crack depth defined as initiation, several specimens were ground down longitudinally until the initiation site was exposed in the plane of polishing. Figure 35 shows the longitudinal view of a carbide initiation site in specimen 3D tested at 538°C (1000°F). The propagation path appears to be transgranular for approximately 4.8mm(0.190 in) (~20 grains) before switching to an intergranular mode. In Figure 36, examination of specimen 6B tested at 871°C (1600°F) identified the initiation site as a 0.005mm (0.0002 in) surface pore. The crack grows approximately 0.76mm (0.030 in) (3 grains) transgranularly before switching to an intergranular mode.

44

Examination of additional specimens has shown an increasing tendency toward intergranular cracking with higher temperatures and slower strain rates. Figure 37 shows the representative crack growth path in specimens tested at 538°C (1000°F) and 871°C (1600°F). The approximate crack depth for 10% and 50% of the specimen test life is superimposed. Clearly, a large portion of the cyclic life is spent on transgranular crack growth at these conditions.

Transmission Electron Microscopy (TEM) was used to characterize the dislocation structure developed by the cyclic testing. The typical dislocation structure of a specimen tested at 538°C (1000°F) (4D) is shown in Figure 38. It appears that the large γ' particles impede the motion of dislocations which results in the dislocations tightly encasing the individual particles of γ'. Two active octahedral slip systems were identified: (111) <$\overline{1}$10>, location A, and (111) <$\overline{1}0\overline{1}$>, location B. The typical dislocation structure of a specimen tested at 871°C (1600°F) (6D) is shown in Figure 39. In this case the dislocations do not form the tight encasement of γ' particles; rather, they gather in the matrix regions along the direction of the Burgers vector. Since cross slip is easier at 871°C (1600°F) than at 538°C (1000°F), as the dislocations encounter resistance from the γ' particles they apparently overcome the resistance by cross slipping onto a different slip system. There appears to be a general directional alignment of the dislocation activity in Specimen 6D (see Figure 39). Three active octahedral slip systems were identified in this specimen: (111) <$\overline{1}$10>, (111) <0$\overline{1}$1> and (111) <$\overline{1}0\overline{1}$>, typical of dislocations at locations A, B and C.

The thin foil specimens of 4D and 6D were taken ~7.1mm(~1/4 in) below the fracture. In order to establish that the dislocation structures observed were representative of deformation at the fracture surface, a thin foil was made on a second specimen tested at 538°C (1000°F), specimen 3D, immediately below the fracture. The results (Figure 40) generally agree with the observations made on Specimen 4D which suggests that the deformation process is at least initially "homogenous" throughout the gage section. Specific observations used in the development of the proposed life prediction model will be discussed in Section 3.3.
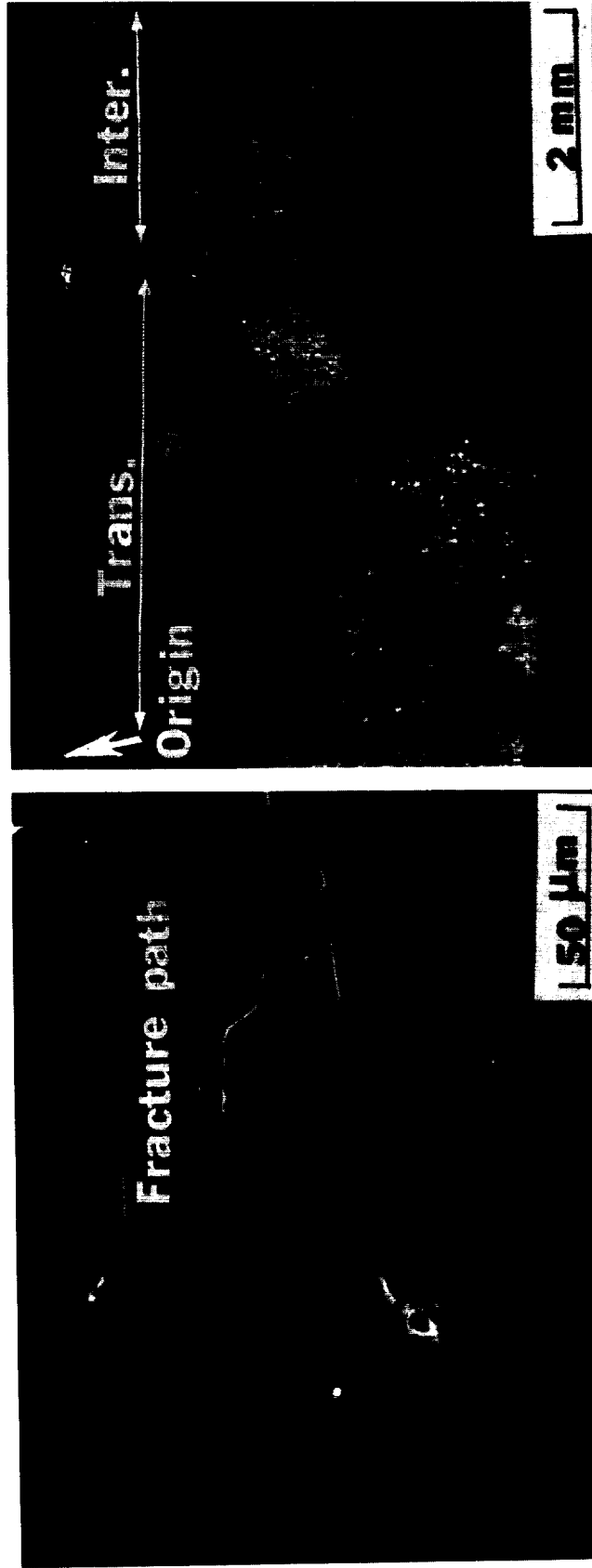
(a)

(b)

Figure 35 Longitudinal View of Specimen 3D After Being LCF Tested at 538°C (1000°F), $\Delta\epsilon_t = \pm\,0.25\%$, 10cpm for 13,300 Cycles. (a) Carbide at crack initiation site is shown by arrow. (b) Crack propagates transgrannularly and becomes intergrannular at location shown by arrow.

46
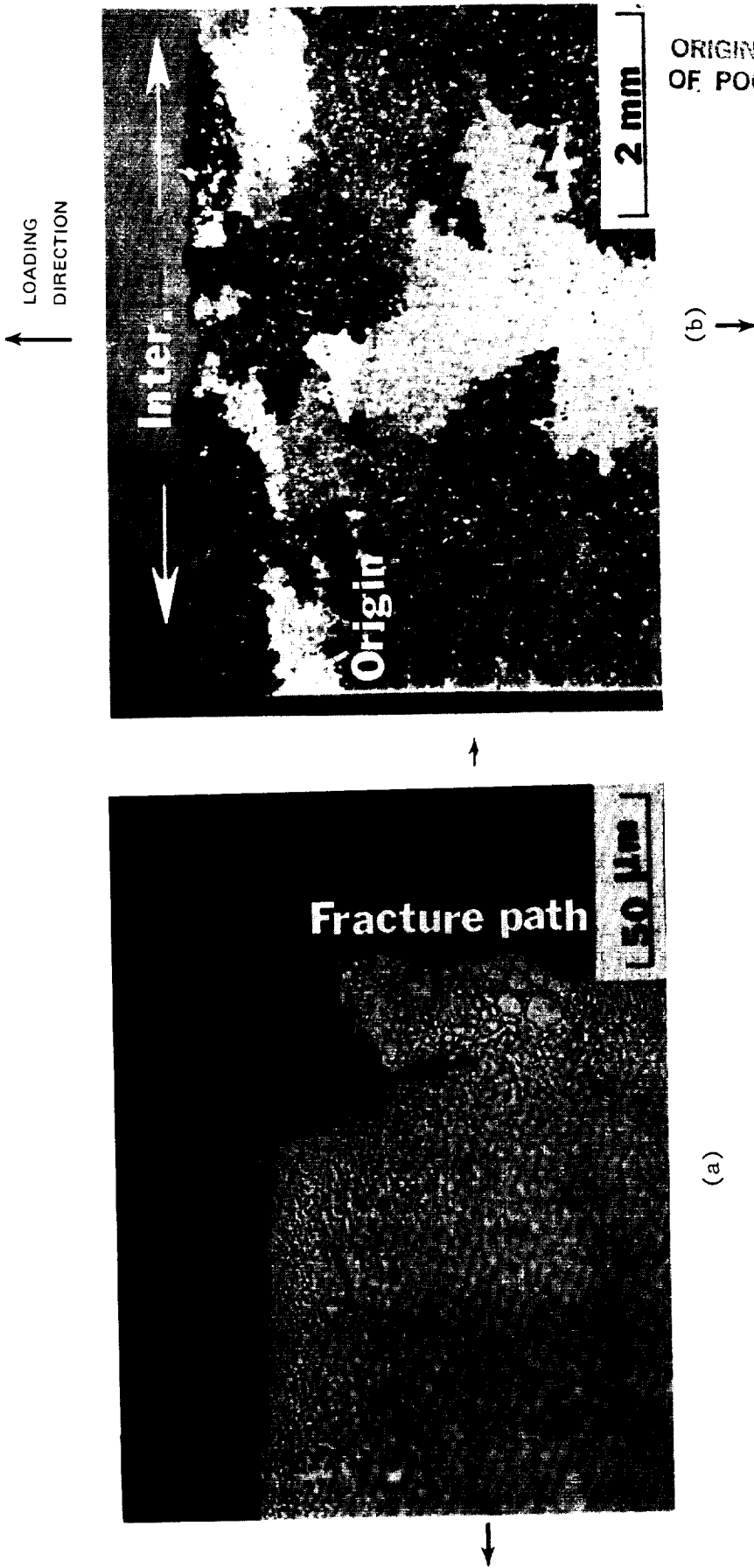
Figure 36 Longitudinal View of Specimen 6B After Being LCF Tested at 871°C (1600°F), $\Delta \epsilon_t = \pm 0.25\%$, 10cpm for 2716 Cycles. (a) Porosity at crack initiation site is shown by arrow. (b) Crack propagates transgrannularly and becomes intergrannular at location shown by arrow.

47

871°C (1600°F)
3,859 CYCLES (6.432 HRS)

538°C (1000°F)
10,650 CYCLES (17.75 HRS)

Figure 37   Primary Crack Depth at 10% and 50% of Specimen Cyclic Life

Figure 38 Dislocation Structures After
Being LCF Tested at 538°C(1000°F), 10cpm
$\Delta\epsilon_t$ = + 0.25% for 12,500 Cycles, Specimen 4D
(~1/4 in. away from fracture surface).
Zone axis (211) { A: (111) <1$\bar{1}$0>
{ B: (111) <10$\bar{1}$>

Figure 39 Dislocation Structure After Being LCF Tested at
871°C(1600°F), 10cpm, $\Delta\epsilon_t = \pm 0.25\%$ for 2,965
Cycles, Specimen 6D ($\sim$1/4 in away from
fracture surface).
A: ($1\bar{1}\bar{1}$) <$1\bar{1}0$>
B: ($\bar{1}11$) <$01\bar{1}$> Zone axis ($21\bar{1}$)
C: ($1\bar{1}1$) <$\bar{1}01$>
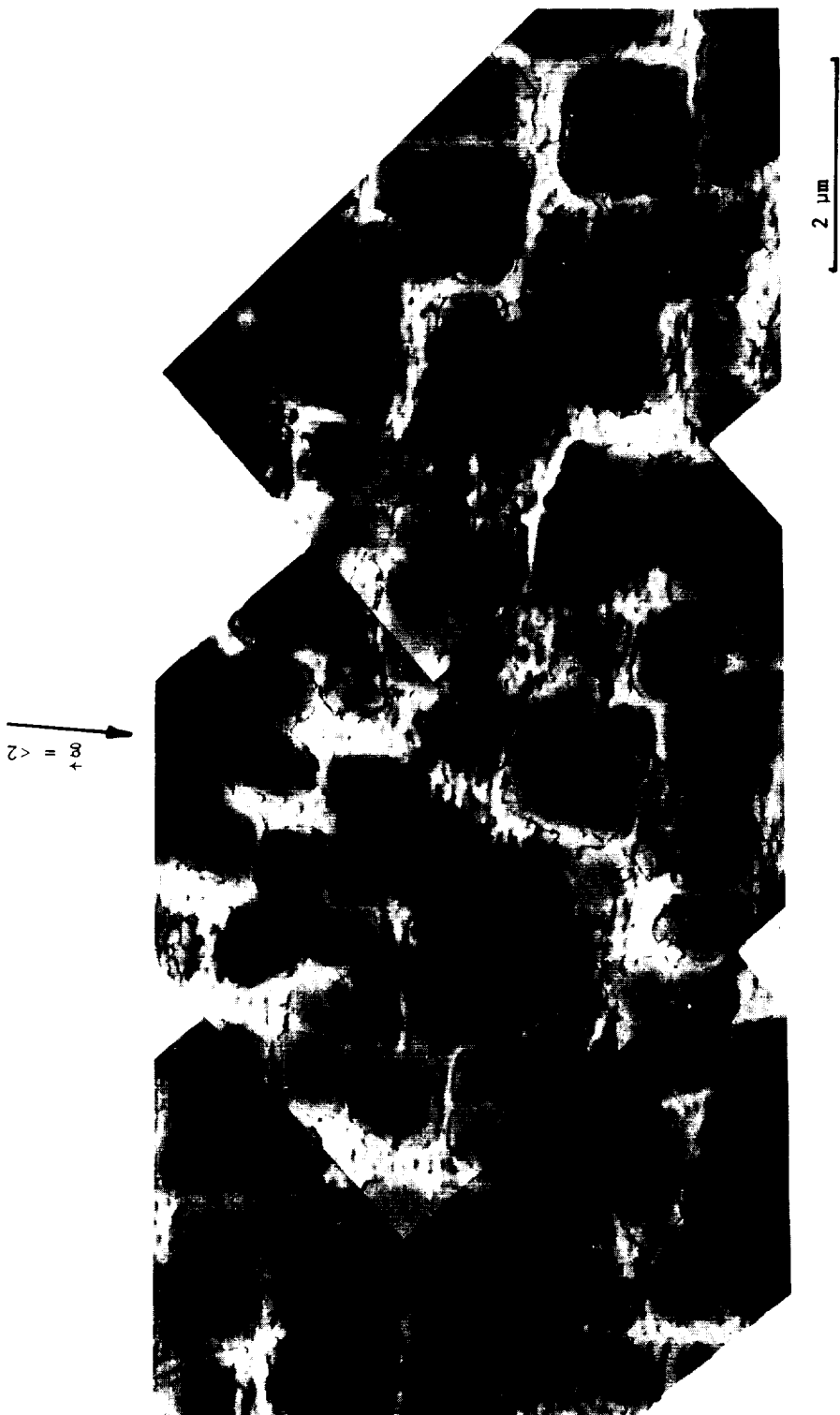
Figure 40   Dislocation Structures After Being LCF Tested at 538°C(1000°F), 10cpm.
$\Delta \epsilon t = \pm 0.25\%$ for 13,330 Cycles, Specimen 3D [1.52mm(0.06 in.) below
fracture surface].

3.2 TASK II SCREENING OF CANDIDATE LIFE PREDICTION APPROACHES

3.2.1 Model Selection and Screening Criteria

One of the fundamental objectives of this research effort is the identification of a fatigue life methodology or approach suitable for the wide range of conditions experienced by hot section structural components. For this effort, it is necessary to distinguish between an "approach" and a "model". A life prediction approach is considered as a conceptual basis for the prediction of cyclic life. Within current life prediction technology, approaches span the range of purely phenomenological to mechanistic. A life prediction model is the application of an approach in a mathematical form (a function or functional) for the prediction of life. On a relative basis, existing models can be characterized as shown in Figure 41, where the extreme left represents a purely phenomenological approach with increasing degree of mechanistic basis associated with the position to the right. As suggested in the figure, a model such as the Frequency Modified Life (Refs. 1,2), which relates the fatigue to inelastic strain range and frequency, is empirically derived using the observable macroscopic variables. All of the local macroscopic effects which determine life (crack initiation) are embodied in these parameters which are considered constant through the cyclic history.
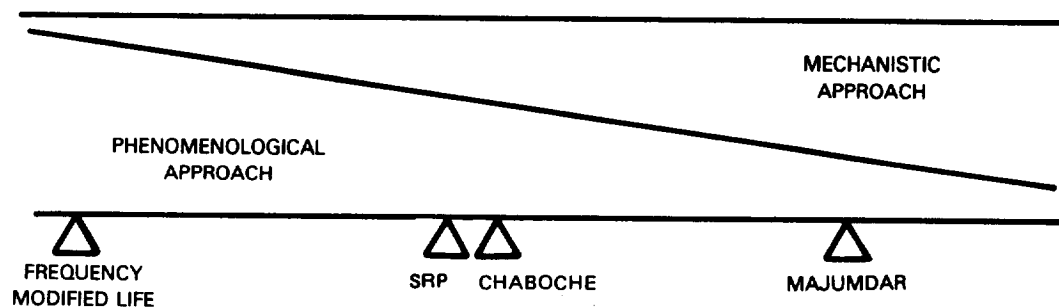
Figure 41 Characterization of Life Prediction Models

The Strainrange Partitioning (SRP) (Refs. 3,4,5) model also relates cyclic life macroscopic (observable) parameters, but has, as its foundation, the notion of local damage associated with reversible rate dependent effects. For this reason, it is considered to be more mechanistic than Frequency Modified Life. Chaboche's Damage Rate (Refs. 6,7,8) model represents a different approach from the previous two models. Local damage is associated with creep rupture and rapid cycle fatigue which accumulate non-linearly. Finally, the model of Majumdar (Refs. 9,10,11) relates the local damage to microscopically observable details (cavity growth, grain boundary cracking, ...). Here, the life relationships are represented as functions of the local damage process. This model is considered more mechanistically based than the previous three models.

From a practical standpoint all of the models use macroscopically observable quantities determined from tests. The primary difference in the approaches is the degree of mechanistic reasoning or justification. None of the models considered use explicitly measured micro-mechanistic properties.

During the initial screening, models representing the entire range of approaches were considered for selection of the best approach for prediction of elevated temperature crack initiation of the hot section structures.

Ranking Procedure

A ranking procedure was developed for evaluation and ranking of the life prediction approaches and models considered in this task. The ranking procedure was based on four criteria considered to be important in assessing the usefulness and predictability of a life prediction model. The four criteria were:

A. The amount and types of test data (called baseline data) required to determine all of the constants in a model to the same degree of confidence.

B. The ability of a model to regress the baseline data and accurately predict verification test data not used in determination of the constants.

C. The fundamental basis for the model (mechanistic vs phenomenological).

D. The amount of judgement required to apply a model to an actual component loading cycle.

Initially, a numerical procedure was developed that assigned point values or scores for each of the criteria. The first three, A, B and C, were scored together, with the first two each given twice as much "weight" as the third. The total score for A, B and C was then compared to a score assigned for criteria D. This was based on the notion that a model which accurately predicted simple cycle data but did not appear to be adaptable to a more relevant component loading cycle would not be considered as desirable as a model which did not predict the data as well, but potentially captured relevant loading cycle characteristics.

In reality, determination of a consistent score for a number of models required that all of the test data be available for each model. This was not practical due to the number of tests being run in support of the program and the fact that the test matrix evolved as trends and effects on fatigue life were identified. The evaluation process that was eventually used was based on the four criteria discussed above, but each model was evaluated with the data available at the time of the evaluation. Models that displayed obvious limitations with a control data set were not given further consideration, while models that displayed certain predictive characteristics were continually evaluated as more data became available. In addition, the crack initiation life for each test condition changed slightly throughout the course of the testing with additional replica data. Ultimately the approach and model which developed from the evaluation procedure, and described in detail in Task III, represents a combination of attractive features of several of the life prediction models considered.

54

3.2.2 Coffin - Manson Model

The Coffin-Manson Model (Ref. 13) was selected as a starting point for evaluation of life prediction approaches. The model ranking criteria, discussed in Section 3.3, were used as a "framework" for the initial evaluation with available fatigue data grouped into three sets designated A, B, and C.

$$A; 871°C (1600°F), \dot{\epsilon} = 1.67\text{-}03 \text{ sec}^{-1}, R = -1$$
$$B; 871°C (1600°F), \dot{\epsilon} = 1.67\text{-}04 \text{ sec}^{-1}, R = -1$$
$$C; 538°C (1000°F), \dot{\epsilon} = 1.67\text{-}03 \text{ sec}^{-1}, R = -1$$

Set A was considered baseline data and used for regression of model constants. Set B did not show a significant strain rate effect on fatigue life and was also considered in the initial model regressions. Set C was used as verification data to evaluate the predictive capability of each model. Prediction of the lower temperature 538°C (1000°F) fatigue lives with the model developed from the higher temperature 871°C (1600°F) data was initally considered a valid test of the predictive capability of the model because of similarities in the physical initiation site and transgrannular growth mode observed at both temperatures.

The crack initiation life for each specimen test was defined as the number of cycles required to produce a 0.76mm(0.030 in.) surface crack. Based on the replica data available at the time of the model evaluation, this was equivalent to approximately 15 percent of the total specimen life for tests conducted at 871°C (1600°F) and approximately 50 percent of the total life at 538°C (1000°F). Previous metallurgical examination had indicated that this portion of the life represented a crack depth of approximately two grain diameters and that the crack progressed transgranually from the initiation site. This observation appeared to be valid for all three data sets. For the model evaluation, it was assumed that the crack initiation process was represented by the cycle response parameters (inelastic strain and rate, etc.) as measured at the crack initiation life.

The model assumes a relationship between inelastic strain range and fatigue life. Regression and prediction of the three data sets with this model is presented in Figures 42 to 44.

As shown, combining data set B with set A (Figure 43) did not significantly change the model regression. This is due principally to a small strain rate effect on fatigue life for the conditions tested. Using this regressed model as a prediction of data set C (Figure 44) resulted in a conservative prediction of the crack initiation life at 538°C (1000°F). A later summary of test data including 538°C (1000°F), 760°C (1400°F), 871°C (1600°F) and 982°C (1800°F) results is shown in Figure 45 and indicates that a single independent parameter (inelastic strain range) would not correctly present the trends in initiation lives. This observation led to the consideration of life prediction approaches that included more than a single independent parameter.

3.2.3 Damage Rate Model

The Damage Rate Model proposed by Majumdar was considered representative of a more mechanistic approach and includes two independent variables. The model assumes that low cycle fatigue is primarily a process of crack propagation and cavity growth. Micro-cracks and cavities are assumed to be present in the virgin material and the majority of the low cycle fatigue life is spent growing these micro cracks and cavities to a critical crack size at which time they combine to form macro-cracks.

Following the development presented in Reference 12, the model assumes the growth law for the micro cracks and cavities as:

$$\frac{da}{dt} = \begin{cases} aT|\epsilon_{in}|^m|\dot{\epsilon}_{in}|^K & \text{(For tensile stresses)} \\ aC|\epsilon_{in}|^m|\dot{\epsilon}_{in}|^K & \text{(For compressive stresses)} \end{cases} \qquad (1)$$

$$\frac{dc}{dt} = \begin{cases} cG|\epsilon_{in}|^m|\dot{\epsilon}_{in}|^{Kc} & \text{(For tensile stresses)} \\ C(-G)|\epsilon_{in}|^m|\dot{\epsilon}_{in}|^{Kc} & \text{(For compressive stresses)} \end{cases} \qquad (2)$$
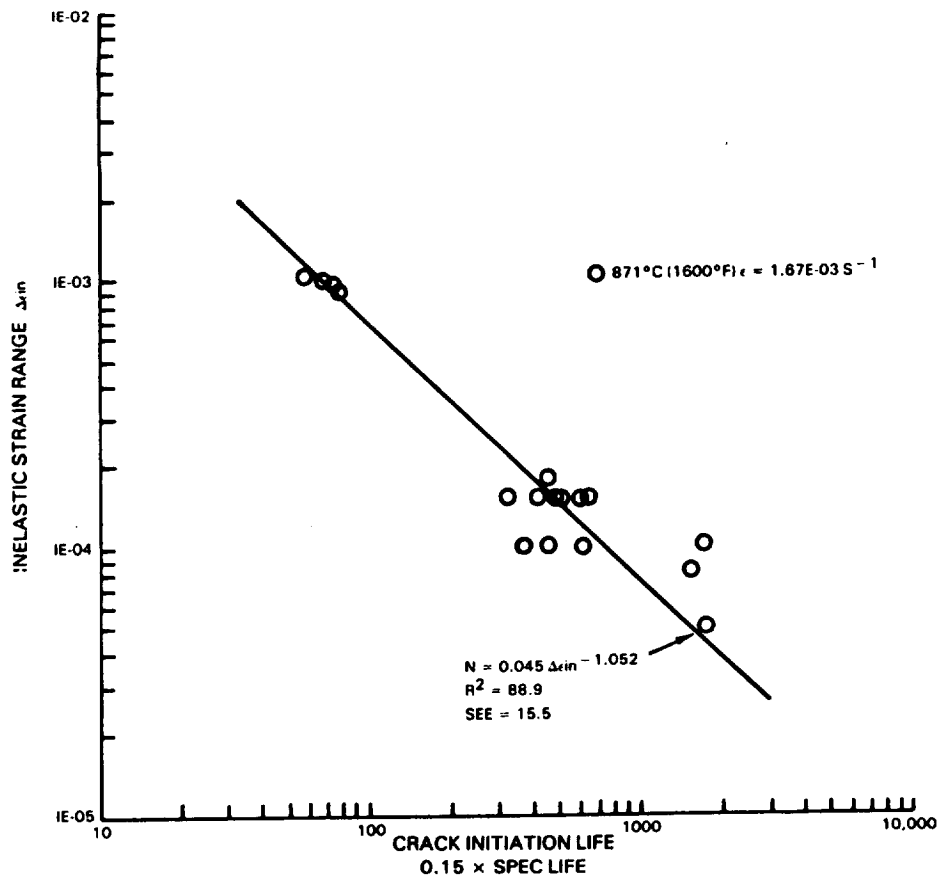
Figure 42   Regression of Coffin-Manson Model to Baseline Data (A)
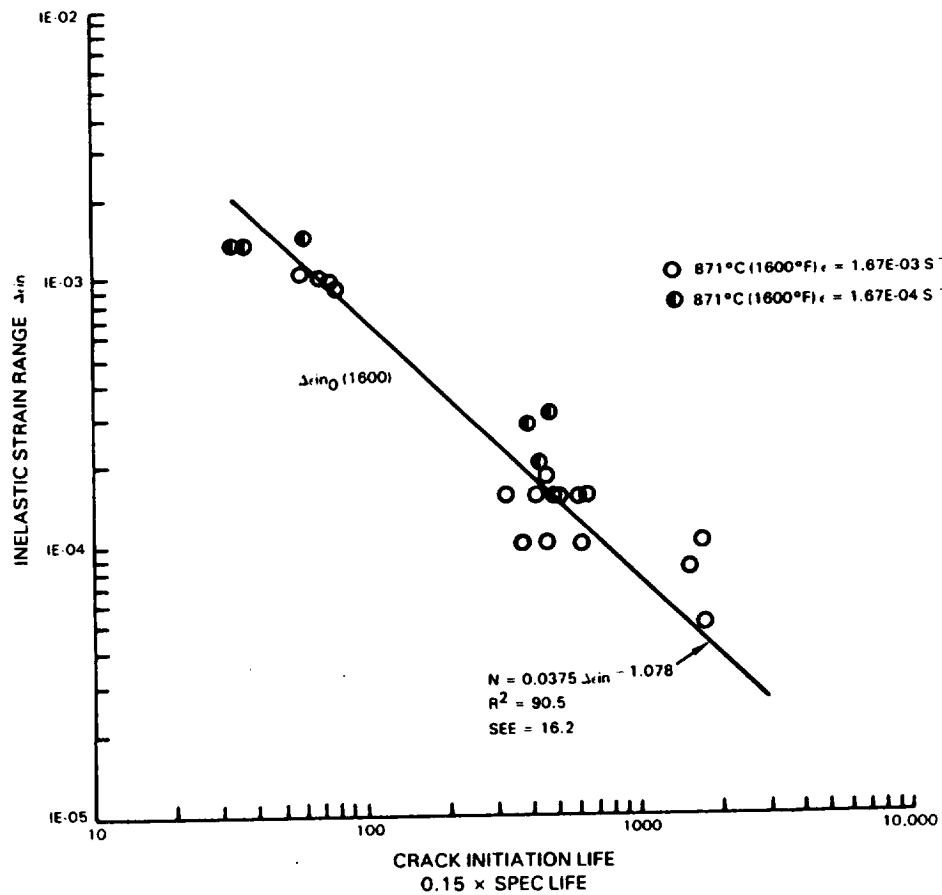
Figure 43   Regression of Coffin-Manson Model to Combined Baseline Data (A + B)

57
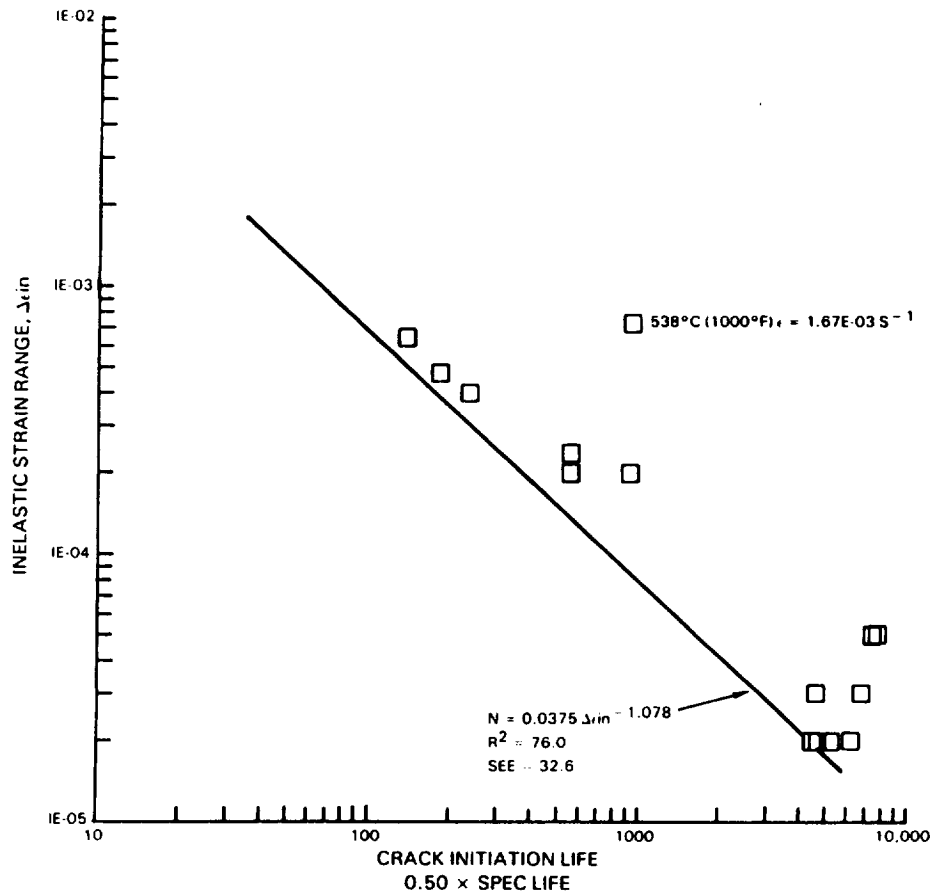
Figure 44   Coffin-Manson Prediction of Verification Data (C)
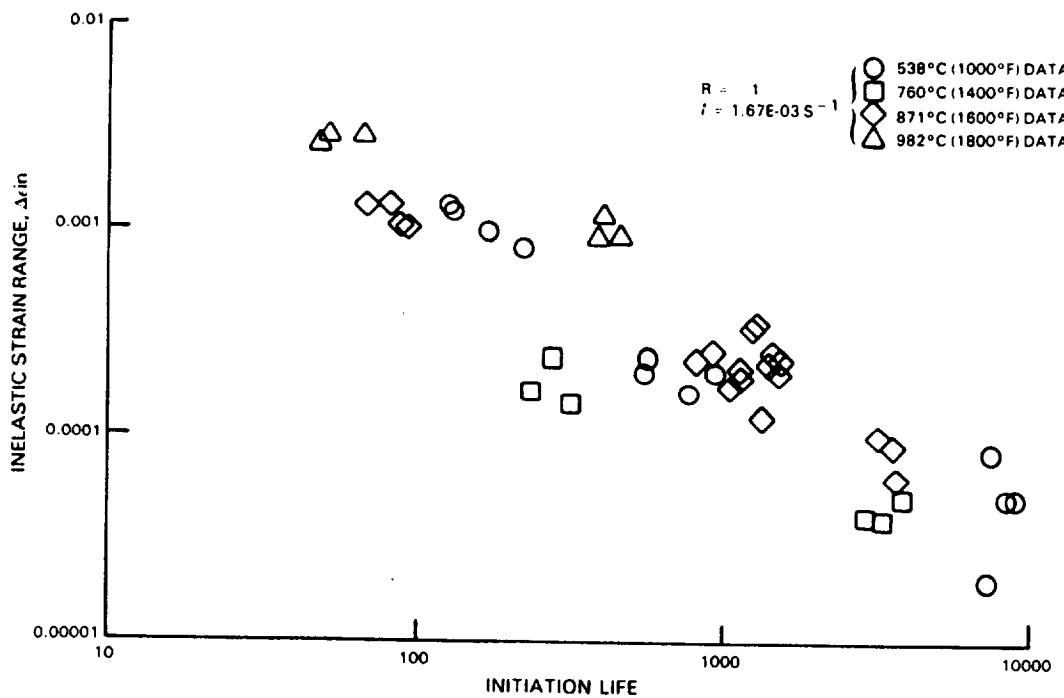
Figure 45   Variation of Initiation Life with Inelastic Strainrange and Temperature

where: a = crack length
        c = cavity length
        t = time
       ϵ_{in} = inelastic strain
       $\dot{\epsilon}_{in}$ = inelastic strain rate
       T, C, G, m, K, Kc = constants

For the current evaluation, a predictive form of the model appropriate to continuous cycling at a constant strain rate was used:

$$Nf = B\left(\frac{\Delta\epsilon_{in}}{2}\right)^{-(m+1)} (\dot{\epsilon}_{in})^{(1-k)} \qquad (3)$$

This form is determined by integrating equations 1 and 2 over an ideal cycle which contains equal (tensile and compressive) peak stresses and inelastic strains, and constant inelastic strain rate. In the model development, it is assumed that the primary cavity growth mechanism is associated with tensile or compressive hold times. Thus, the continuous cycling form of the model does not include cavity growth. This was considered to be consistent with the observed transgrannular process in the tests used for the evaluation.

Regression of the model (Equation 3) to data set A indicated that the two-parameter model was able to better fit the baseline data than the Coffin-Manson Model discussed above. A comparison of the baseline data and the prediction for various inelastic strain rates (constant total strain rate) is shown in Figure 46.

Application of the model to data set B results in predicted lives that are significantly smaller than the experimental data. This is due to the lack of a strain rate effect on crack initiation life for the conditions tested (see Figure 47). A similar situation exists in the prediction of the 538°C (1000°F) tests in data set C (see Figure 48) using the 871°C (1600°F) model constants. The preliminary results obtained with both the Coffin-Manson and Continuous Damage Models indicate that the use of single valued macroscopic parameters (inelastic strain range and rate) are not sufficient to predict fatigue lives at various temperatures. Furthermore, the data used in this initial evaluation was developed at zero mean strain ($R\epsilon = -1$). The predictive capability of each model was not evaluated on non-zero mean strain.
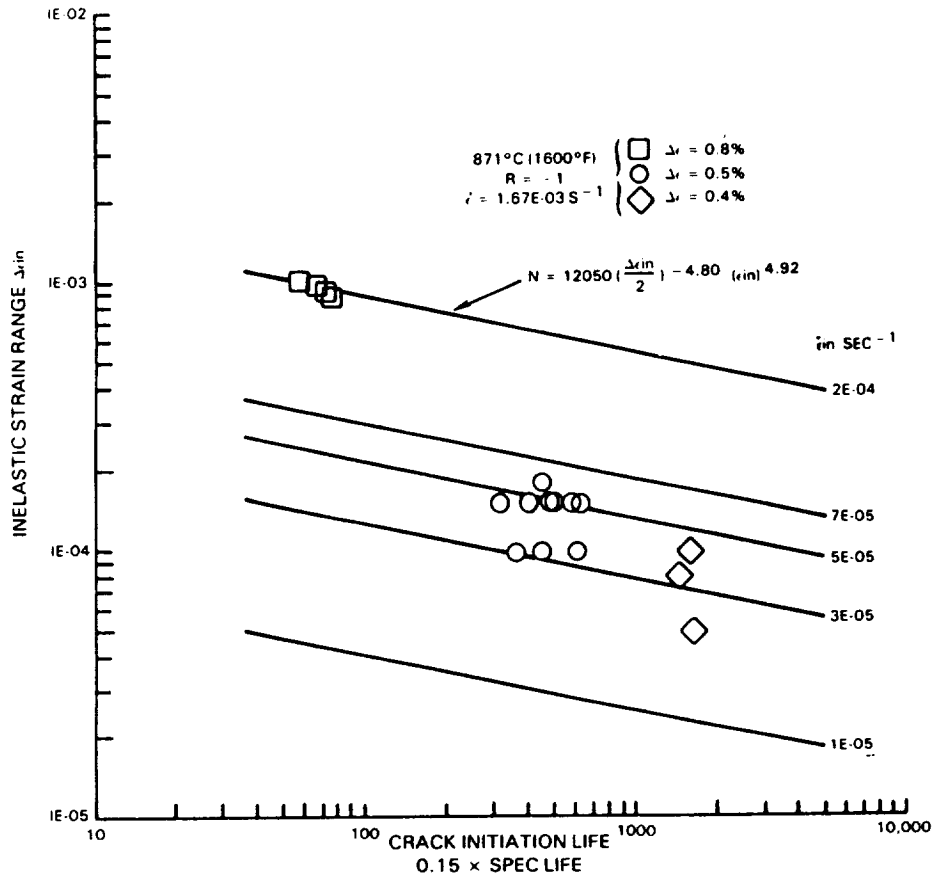
Figure 46 Regression of Baseline Data With Damage Rate Model
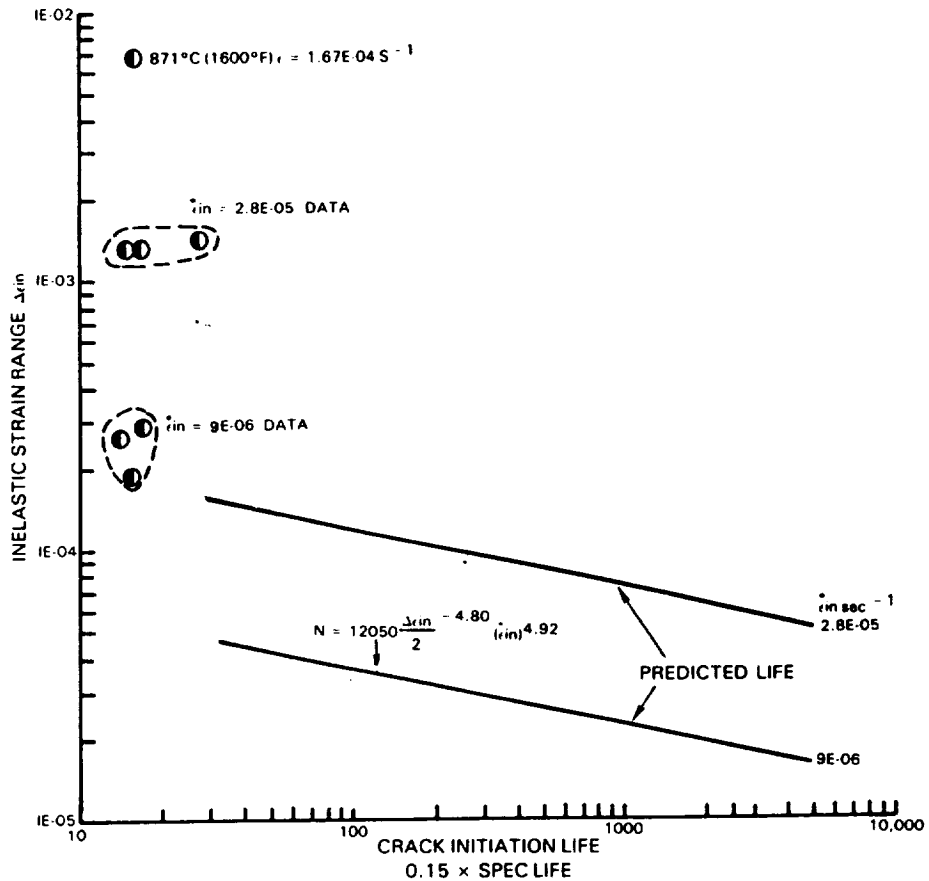
Figure 47 Prediction of Data Set B by Damage Rate Model
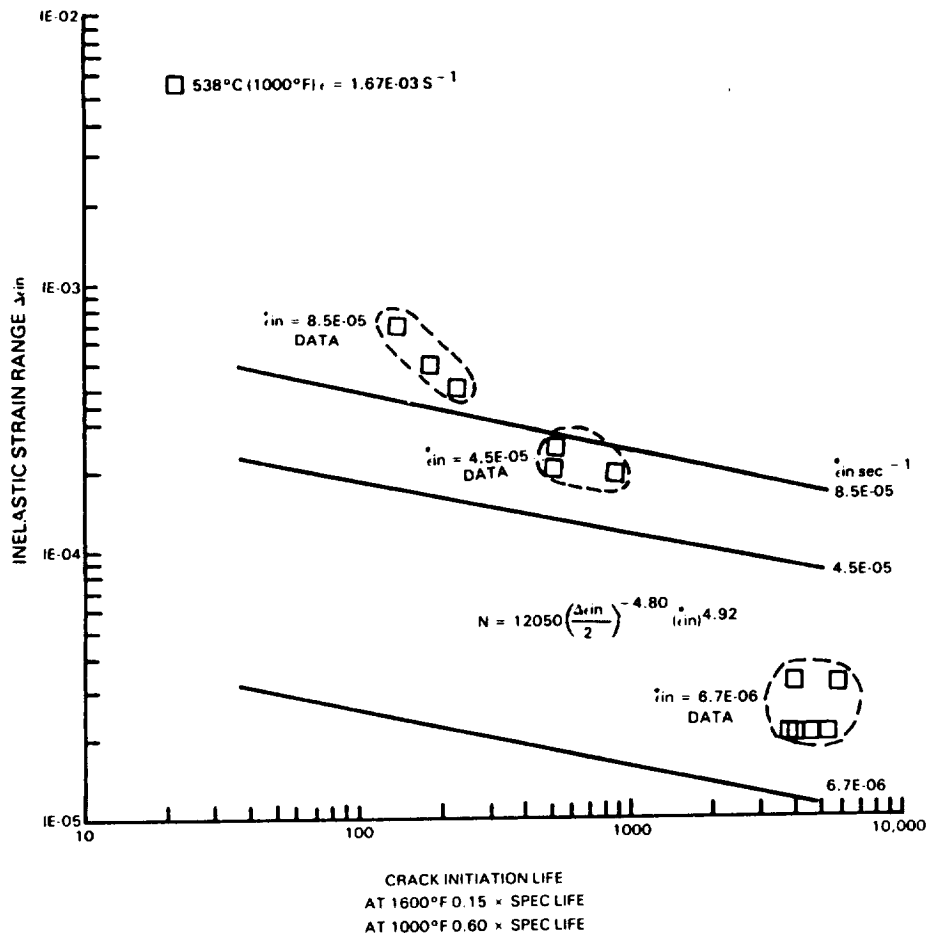
Figure 48   Prediction of Data Set C by Damage Rate Model

3.2.4   Tensile Hysteresis (Ostergren) Fatigue Model

General observations of the complete fatigue data set and experience with two previous models suggested that a single independent parameter ($\Delta\epsilon$ in, $\Delta\sigma$, etc.) is not sufficient to correlate the fatigue life at all test conditions. It appeared that some combination of stress and inelastic strain would be a better parameter. To investigate this assumption, a data set of nine tests run at either 871°C (1600°F) or 932°C (1800°F) with various strain rates was selected. As a baseline, a regression of the data using inelastic strain range, as the independent parameter, and specimen separation life was performed and is shown in Figure 49. The data tends to segregate with temperature and is reflected in the poor correlation coefficients (R^2 = 0.77, SEE = 0.23). Considering the product of the stress range and inelastic
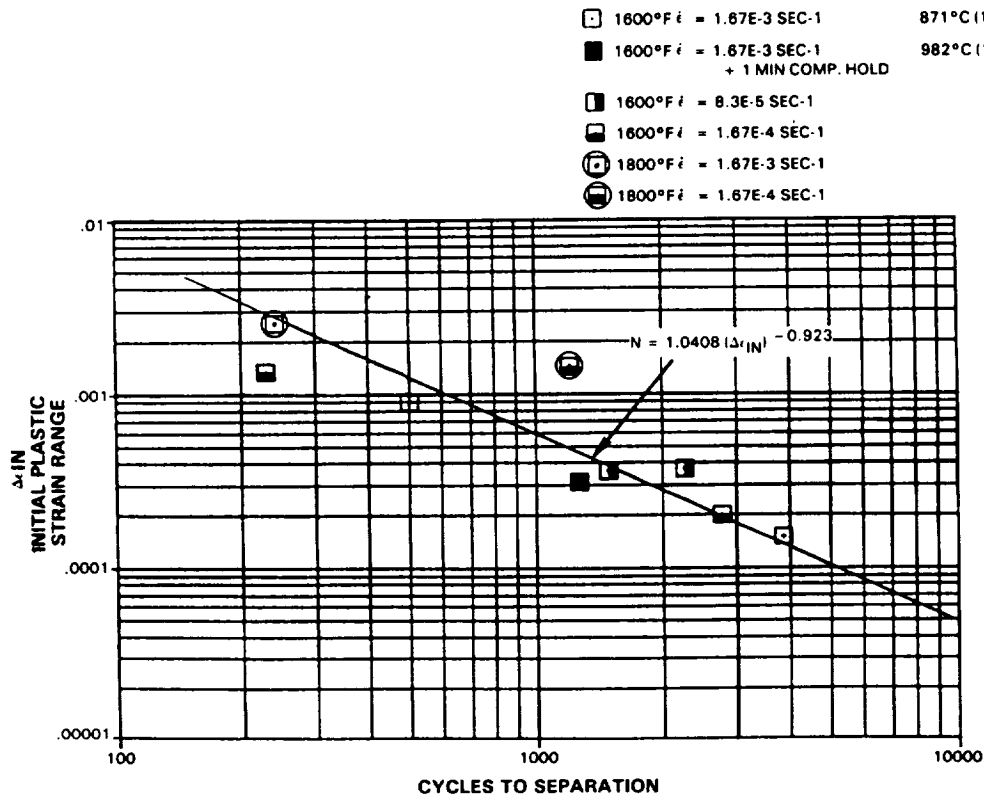
Figure 49 Life vs Initial Inelastic Strain Range

strain range ($\Delta\sigma \times \Delta\epsilon$ in) as the correlating parameter, results in improved regression coefficients, as shown in Figure 50 (R^2 = 0.90, SEE = 0.15). The 871°C (1600°F) is slightly more ordered with respect to strain rate and not as much segregation of the 932°C (1800°F) data is observed. Following an approach analogous to the Ostergren Fatigue Model [14], it was assumed that the hysteresis loop area might be a better correlating parameter. This results in the regression shown in Figure 51 which has the best coefficients of the models considered (R^2 = 0.93, SEE = 0.13). In this correlation, the hysteresis loop area was calculated for each test and the cycle frequency (as suggested by Ostergren), not included in the model regression. This parameter provided the best ordering of the 871°C (1600°F) data considering three strain rates and the effect of a one minute compressive dwell. In addition, the smallest amount of temperature segregation was observed. Based on the preliminary results, further investigation of this approach to a larger data set appeared worthwhile.

62

Figure 50   Life vs Stress Range x Inelastic Strain Range

Figure 51   Life vs Hysteresis Loop Area

Evaluation of the tensile hysteresis loop area as a correlating parameter was then evaluated on a larger data set. A baseline data set consisting of rapid cycle ($\dot{\epsilon}$=1.67E-03 S^{-1}), fully reversed (R=-1) tests at 760°C (1400°), 871°C (1600°F), and 932°C (1800°F) (20 points) was established to determine regression constants. Two models were regressed, the first considered only the 871°C (1600°F) baseline data (5 points):

$$N_1 = 36932 \ (Area)^{-1.504} \qquad (4)$$
$$(R^2 = 95.1, \ SEE = 0.21)$$

The second considered the entire baseline data set (20 points):

$$N_2 = 14592 \ (Area)^{-1.1704} \qquad (5)$$
$$(R^2 = 84.5, \ SEE = 0.31)$$

Life (N) in equations 4) and 5) is defined as the crack initiation life. The "Area" term was calculated as the average of the initial and stabilized tensile hysteresis response. A verification data set consisting of 20 data points was used to evaluate the predictive capability of both equations. This data set was specifically selected to evaluate the uniqueness of the tensile hysteresis area for creep fatigue and non-zero mean strain conditions. Test conditions included in the data set were:

1. 871°C (1600°F), R_ϵ=-1, $\dot{\epsilon}$ = 1.67E-04, 0.833E-04 S^{-1}
2. 871°C (1600°F), R_ϵ=-1, 1 minute compression hold
3. 871°C (1600°F), R_ϵ=-1, 1 minute tension hold
4. 982°C (1800°F), R_ϵ=-1, 1 minute compression hold
5. 760°C (1400°F), R_ϵ=0, $\dot{\epsilon}$=1.67E-04 S^{-1}

Correlation of the actual vs. predicted lives for conditions 1, 3, 5 is shown in Figure 52. The consistent under-prediction of the lives suggests that the total tensile hysteresis area is not damaging. This is particularly evident for the tensile hold (3) and Rϵ=0 (5) conditions where a significant amount of mean stress relaxation occurs. A portion of the cyclic response must be non-damaging or anelastic based on the above observation. Prediction of the complete verification data set by equation 5 is shown in Figure 53. Again the general trend is to under-predict the actual lives.

64
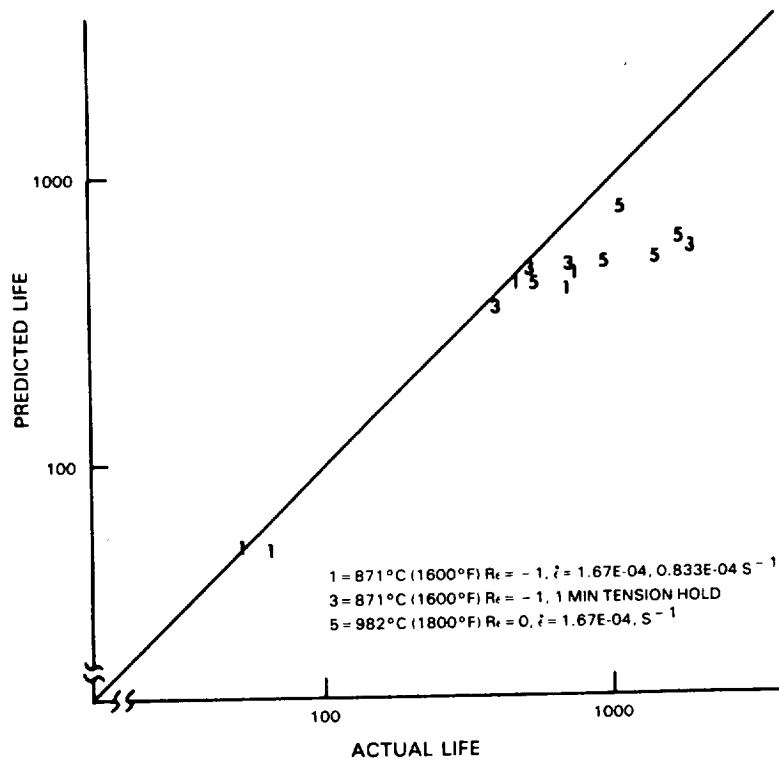
Figure 52   Prediction of 871°C (1600°F) Verification Data Set by Tensile Hysteresis Loop Area
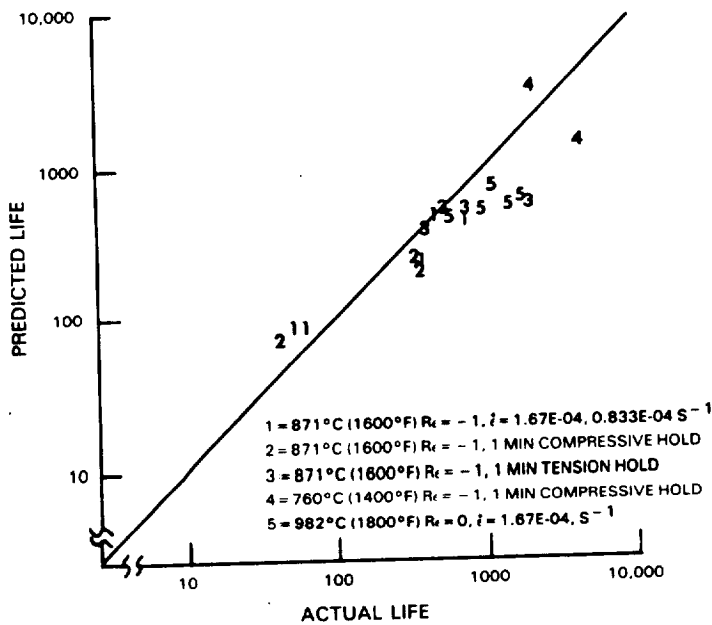
Figure 53   Prediction of Total Verification Data Set by Tensile Hysteresis Loop Area

An estimate of the maximum error in calculating the hysteresis loop area was made by repeatedly analyzing a 538°C (1000°F), $\epsilon = \pm 0.25\%$ test. This represented the narrowest hysteresis response encountered to date. A calculated variation in the area of $\pm 20\%$ from the mean value was observed. This was considered to be too large a variation for life prediction evaluation. Based on the predictive capability discussed above, and the uncertainty in the area calculation, this life prediction approach was not considered a viable candidate for future consideration.

3.2.5 Local Crack Tip Parameter Models

The experience with the three models (approaches) discussed above suggested that the "far field" macroscopic hypteresis response may not be representative of the local conditions which result in creep-fatigue crack initiation. This resulted in the evaluation of two approaches in which local crack tip conditions were used as correlation parameters for fatigue initiation. The results reported in [15] indicated that crack tip opening displacement (CTOD) was partially successful in correlating elevated temperature fatigue crack growth. As a preliminary assessment for this work, it was assumed that the fatigue life could be correlated with CTOD, i.e.:

$$N = K \, (CTOD)^{\beta} \tag{6}$$

where the McMeeking [16] relationship was used to define the CTOD as:

$$CTOD = \frac{0.55J}{2\ \sigma_0} \left[\frac{2}{\sqrt{3}} \ (1 + \nu) \ (1 + n) \ \frac{\sigma_0}{nE} \right]^n \tag{7}$$

where: n = strain hardening exponent in stress-strain representation
       σ_0 = yield stress
       E = Young's Modulus
       ν = Poisson's Ratio

66

Calculation of the J integral considered the sum of elastic and plastic components following Shih and Hutchinson [17] and assumed that the tensile portion of the cyclic hysteresis loop could be used to estimate the cyclic parameter.

$$J = J_{el} + J_{pl} \tag{8}$$

$$J = \frac{\sigma_{max}^2}{E} \pi a \left(\frac{2}{\pi}\right)^2 + \alpha \left(\frac{2}{\pi}\right)^2 \sigma_0 \epsilon_0 a \left[\frac{1}{1.276\eta}\right]^{n+1} h_1 \left[\frac{\sqrt{3}}{2} \frac{\sigma_{max}}{\sigma_0}\right]^{n+1} \tag{9}$$

where: h_1, η = functions of crack geometry

a = 1/2 crack length

α, n = parameters in Ramberg Osgood stress strain representation

σ_0 = yield stress

ϵ = yield strain

Initial calculations of J at 871°C (1600°F) for fully reversed (Rϵ=-1) strain range of $\pm$0.4%, $\pm$0.25% and $\pm$0.2%, shown in Table I, indicated that Jpl is less than 30% of the total J.

TABLE I

PREDICTED J AT 871°C (1600°F)

$\Delta\epsilon(\%)$	Jel	Jpl
$\pm$0.4	0.0203	0.0070
$\pm$0.25	0.0100	0.0004
$\pm$0.20	0.0075	0.0003

Therefore, for this exercise, J was calculated as:

$$J \approx Jel \approx \frac{\sigma_{max}^2 \, a}{E \, \sigma_0} \tag{10}$$

67

For the regression it was assumed that the CTOD associated with the "initiated" 0.030-inch crack characterized the entire growth process up to this crack length. Regression to a 871°C (1600°F) data set (Rϵ=-1, ϵ=1.67E-03 S^{-1}) with an "initiation" life associated with a 0.030-inch surface crack resulted in the model:

$$N = 5.72E-11 \ (CTOD)^{-2.94} \tag{11}$$

Experience with this model is summarized in Figure 54 where the predicted and actual initiation lives for the baseline data set and two validation data sets (871°C (1600°F), Rϵ=-1, $\dot{\epsilon}$=1.67E-04 S^{-1} and 538°C (1000°F), Rϵ=-1, $\dot{\epsilon}$=1.67E-03 S^{-1}) are shown. As indicated, the predicted lives for both validation data sets are consistently longer than the actual data. For the 871°C (1600°F) slow strain rate tests, this is the result of a reduction of the crack tip J (CTOD) due to a reduction of the maximum tensile stress relative to the yield stress (σmax vs. σo in equation 10). This would appear to be contrary to the time dependent damage and subsequent reduction on life of the slower strain rate. For the 538°C (1000°F) data set, the predictions also suggest a reduction in the predicted value of J; however, this is associated with the small difference between the maximum tensile stress and yield stress (σmax vs. σo in Equation 10) consistent with a reduced degree of plasticity at 538°C (1000°F) relative to 871°C (1600°F). Based on these two predictions, it appears that the single parameter J is clearly underpredicting the local damage which produces initiation.

Use of a "classical" linear elastic fracture mechanics for prediction of the initiation life from a small flaw (carbide or porosity) to the 0.76 mm (0.030") surface crack length was also considered. For the two-dimensional surface crack the value of the stress intensity factor (K) was determined based on finite element results presented in [18]. As a conservative approach the value of K at the free surface was assumed to exist along the entire crack face and was calculated as:

$$\Delta K = \frac{2.4}{\pi} \sigma max \ \sqrt{\pi a} \tag{12}$$
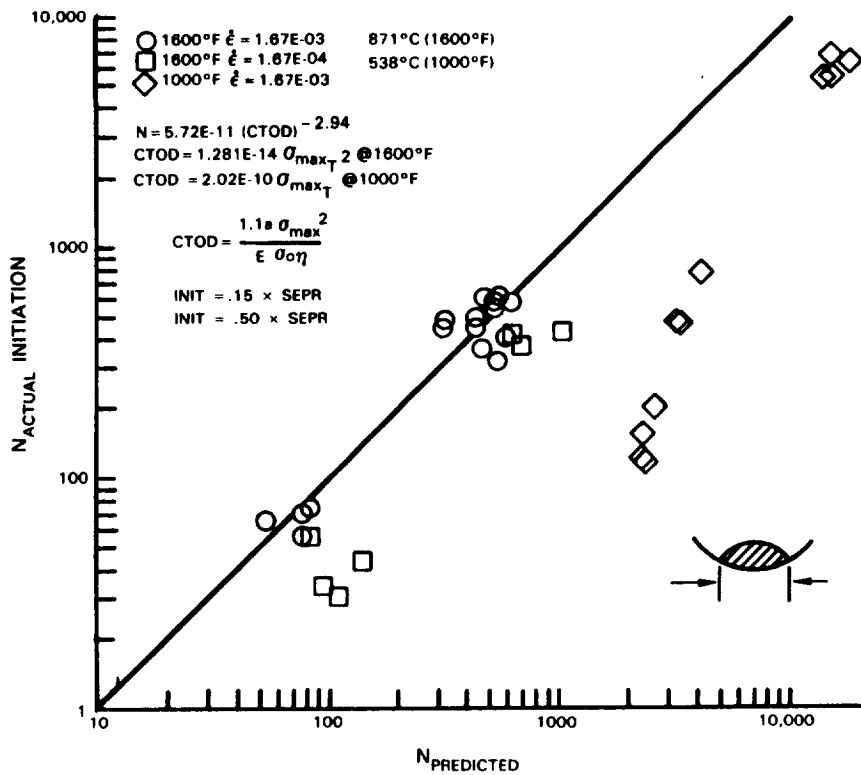
Figure 54   Correlation/Prediction of Life to a .030 Surface Crack by a "Characteristic" CTOD

which assumes that the crack opens at zero stress. Application of this approach together with available crack growth rate data consistently produced predicted lives much longer than the actual lives. Average predictions at temperatures for fully reversed ($R\epsilon$=-1) rapid cycle testing (Figure 55) indicate that better predictions were obtained at the higher temperatures and for crack growth from 0.015 to 0.100" in half length, however the predictions are at least a factor of 2 longer than the actual average life. A portion of the overprediction may be associated with the fact that the ΔK levels of the small crack size was below the range of the test data used to determine the growth rate, thus there may be some uncertainty in the actual growth rate at low values of ΔK. It was also judged that generation of reliable crack growth rate data for the relevant ΔK levels associated with the initiated crack size represented a significant burden for development of a life prediction model.

Based on these results, the use of a CTOD parameter and linear elastic fracture mechanics were not considered as practical approaches for the prediction of creep-fatigue initiation of B1900+Hf.

69
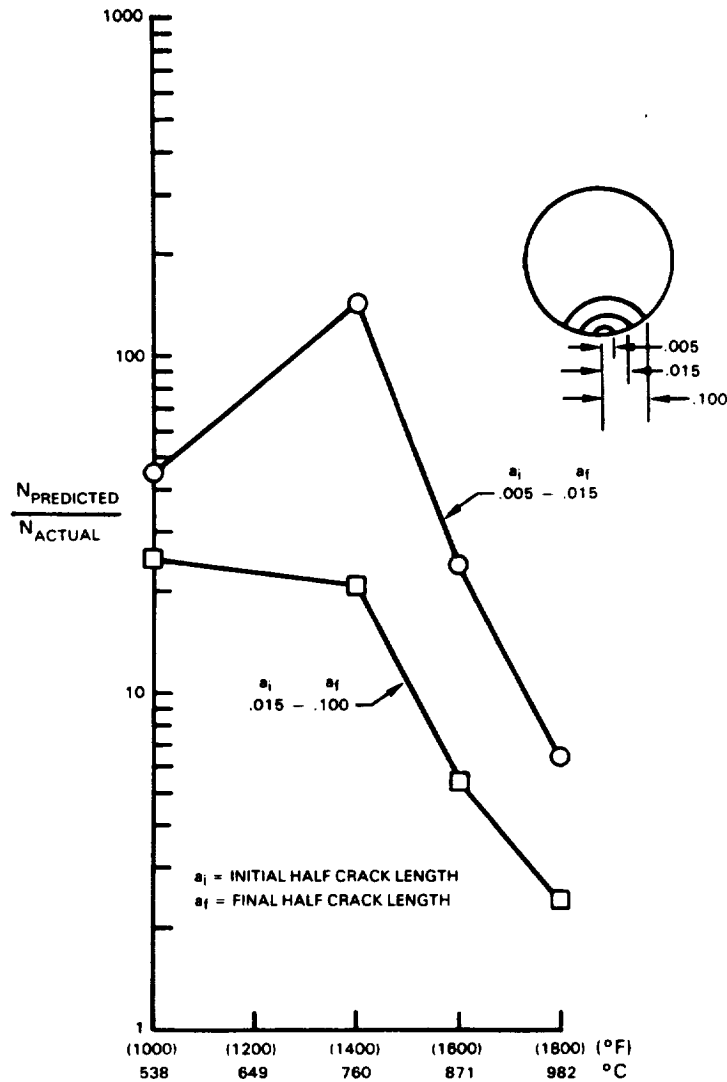
Figure 55 Best Prediction at Larger Crack Size and Hotter Temperatures

3.2.6 Total Strainrange Partitioning

All of the approaches (models) evaluated up to this point have used a single correlating parameter. The experience discussed above has indicated that these models have not been able to properly account for the relevant effects associated with creep-fatigue interaction (strain rate and strain hold time effects), mean strain and temperature. Therefore, several models that explicitly included separate damage and mean stress correction terms were considered. The first of these was based on the concept of strain range partitioning.

70

The concept of strain range partitioning [3] assumes the existence of separate time independent and time dependent damage life relationships and includes a method of predicting fatigue life from a combination of these independent relationships. Most of the early application and success of this approach has been with materials and loading conditions in which the critical cyclic hysteresis loop included a measurable amount of inelastic strain. For cycles in which the cyclic inelastic strain is small or non-existent, Halford and Saltsman [19] have proposed a method which extends the concept to the use of total strain-range. Following the above method, and including an explicit mean stress correction as proposed in [20], the life relationships for a B1900+Hf 871°C (1600°F) data set were determined with subsequent application to a separate data set for determination of the predictive capability of the approach. The method is based on the decomposition of total mechanical strain into elastic and inelastic (plastic) components, i.e.:

$$\Delta \epsilon = \Delta \epsilon_{elastic} + \Delta \epsilon_{inelastic} \tag{13}$$

It is assumed that the fatigue life relationships can also be combined to represent a relationship between total strain range and life. For the 871°C (1600°F), $R\epsilon=-1$, rapid cycle data set, inelastic and elastic life relationships for time independent initiation life (pp in strain-range partitioning nomenclature) were determined as:

$$\Delta \epsilon in = 0.291 \ (Npp)^{-0.892} \tag{14}$$

$$\Delta \epsilon el = 0.0203 \ (Npp)^{-0.179} \tag{15}$$

The total strain-range relationship is now written as:

$$\Delta \epsilon_{TOTAL} = 0.0203 \ (Npp)^{-0.179} + 0.291 \ (Npp)^{-0.892} \tag{16}$$

and is shown in Figure 56. In a similar manner, time dependent life relationships were determined with the tensile and compressive strain hold tests. These tests were conducted with a transient strain rate equal to the rapid cycle tests but included a one minute strain hold period. This was considered representative of pc and cp fatigue damage in strain-range partitioning nomenclature. The life relationships were determined from the test data as:

for pc: $\Delta \epsilon_{TOTAL} \ pc = 0.0185 \ (Nf)^{-0.179} + 0.407 \ (Nf)^{-0.892}$ (17)

for cp: $\Delta \epsilon_{TOTAL} \ cp = 0.0185 \ (Nf)^{-0.179} + 0.698 \ (Nf)^{-0.892}$ (18)

and are shown in Figure 57. These equations reflect the assumptions that all of the inelastic strain observed in the tests was either pc or cp (not pp) in nature and that the elastic life relationship was the same for both tensile and compressive hold tests.
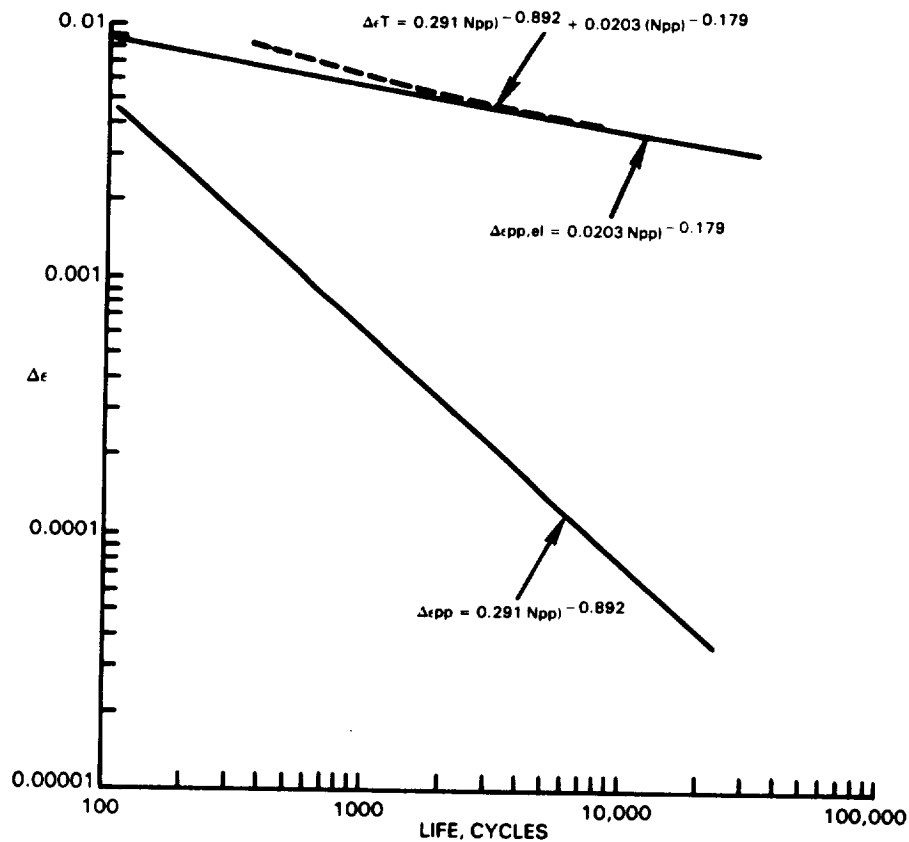
Figure 56 Strain Range Partitioning Life Relationships for B1900+Hf Tests
($\dot{\epsilon}$ = 1.67E-03 s^{-1})

72

The figure contains these labeled equations:

$\Delta\epsilon_{pc,\,el} = 0.0185(N_{pc})^{-0.179}$

$\Delta\epsilon_{pp,el} = 0.0203\,(N_{pp})^{-0.179}$

$\Delta\epsilon_{cp} = 0.698\,(N_{cp})^{-0.892}$

$\Delta\epsilon_{pc} = 0.407\,(N_{pc})^{-0.892}$

$\Delta\epsilon_{pp} = 0.291\,(N_{pp})^{-0.892}$

Vertical axis: $\Delta\epsilon$ (0.0001, 0.001, 0.01)

Horizontal axis: LIFE, CYCLES (10^2, 10^3, 10^4, 10^5)
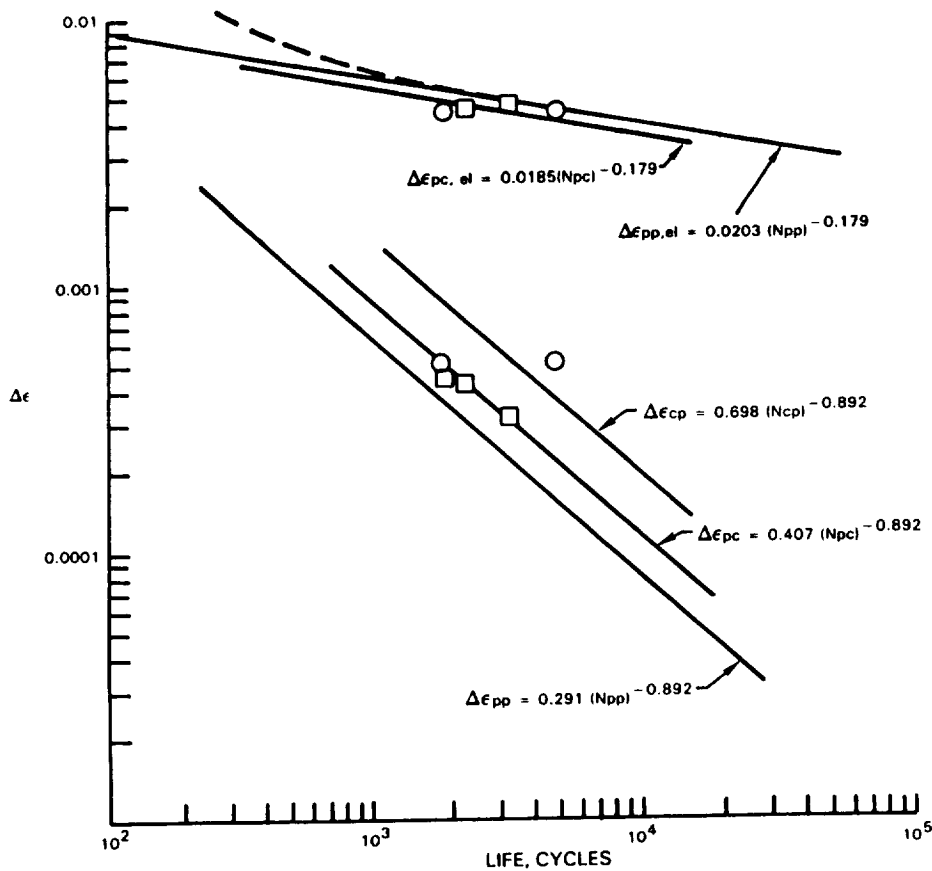
Figure 57   Time Dependent Life Relationships Used for Total Strain - Strainrange Partitioning Model

The above equations were derived for tests whose duration was 66 sec (6 second transient and 60 hold). The elastic portion of the life relationship is considered to be time dependent. An approach used to adjust the relationship with time was proposed in [19] and used here. Basically, the elastic life relationship is assumed to be written as:

$$\Delta\epsilon el,\ ij = Bij\ (Nij)^{c} \tag{19}$$

where ij = refer to the various SRP cycle types pp, pc, cp, cc.

A time dependent relationship between the coefficients is assumed as:

$$\ln\ (Bpp/Bij) = Aij\ (t)^{a} \tag{20}$$

From the available data, constants were determined for the above equation as:

$$\ln\ (Bpp/Bij) = .0333t^{0.25} \tag{21}$$

73

where t = holdtime, seconds. The exponent (0.25) is based on AF2-IDA and Rene'95 data reported in (19).

The elastic portion of the total life relationship can now be determined for various cycle periods.

Evaluation of the predictive capability of this life approach considered three different data sets as verification data. These are:

1. 1600°F, R_ϵ=-1, $\dot\epsilon$=1.67E-04 S^{-1}
2. 1600°F, R_ϵ=-1, $\dot\epsilon$=8.33 -05 S^{-1}
3. 1600°F, R_ϵ= 0, $\dot\epsilon$=1.67 -03 S^{-1}

Prediction of the continuous cycling tests (1 and 2) was made with two different assumptions concerning the nature of the damage. In the first calculation, the damage was assumed to be equally split between pc and cp damage.

In the second, it was assumed that all of the damage was pp in nature. A comparison of the predicted vs. actual lives for both calculations is shown in Figure 58. The second method of calculation (all pp damage) produces a slightly better correlation but both sets of results fall within the scatter band of the regression data used to determine the model constants. Prediction of the R_ϵ=0 tests (3) considered that the damage is characterized as pp in nature with equation 16 representing the total strain range life relationship. This represents a zero mean stress equation since fully reversed (R_ϵ=-1) data was used for the model constants. Adjustment of the life for the observed mean stress used the approach discussed in [20] which states that the effect of mean stress on fatigue life can be expressed as:

$$N_f^{\ b} = N_{fo}^{\ b} - \frac{\sigma m}{\sigma a} \tag{22}$$

where: N_f = fatigue life at observed mean stress

N_{fo} = fatigue life at zero mean stress

σm = observed mean stress

σa = cyclic stress amplitude

b = exponent determined from $N_{fo} = A(\Delta\sigma)^{-b}$

74

A comparison of the predicted vs. actual lives indicates a consistent underprediction by the model (Figure 58). These Rϵ=0 tests were somewhat of an anomaly for most of the life models considered since the data indicates an increase in the median life relative to the Rϵ=-1 tests. The approach used for the mean stress correction would clearly predict a decrease in life with increasing positive mean strains and contributed to the conservative prediction of these tests. Despite these predictions, the total strain range approach demonstrated encouraging positive capability on a complex verification data set. The incorporation of two damage parameters and a separate mean strain correction are responsible for the improved predictive capability. The disadvantage of the approach is the need for complex baseline data to determine model constants. The strain hold tests required for the pc and cp coefficients are lengthly (costly) and generation of a sufficient number of data points for development of a fatigue design system was considered an unattractive data requirement. Therefore, the method was not considered as the best overall life prediction approach but several of its characteristics were considered in future model evaluations.
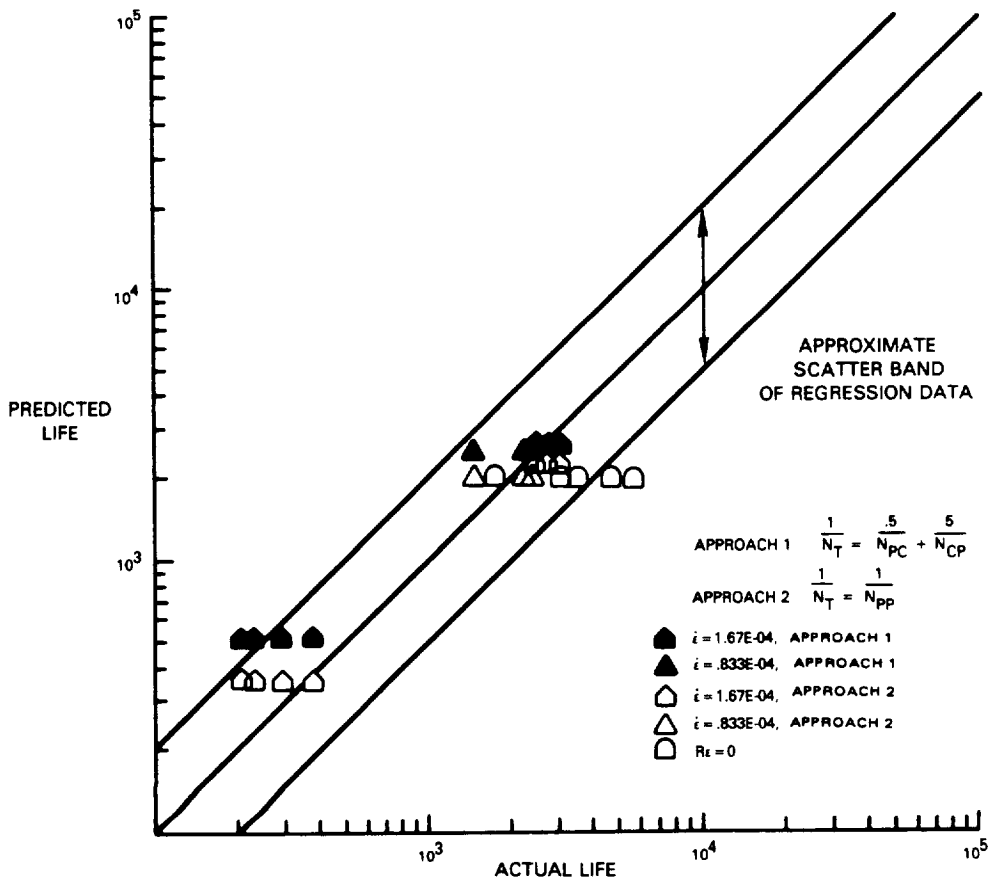
Figure 58   Prediction of Continuous Cycling and R ϵ = 0 Tests by Total Strain Range Partitioning Method

75

3.2.7 Ductility Exhaustion Model

One of the less desirable aspects of the total strain-range Partitioning model discussed in Section 3.2.6 was the requirement for complex strain hold testing to determine the time dependent damage component. This led to consideration of models in which the time dependent damage component could be determined from monotonic creep data. Models which fell into this category are Ductility Exhaustion [21] and Chaboche's Continuous Damage [22, 23, 24]. Fundamental to the Ductility Exhaustion model is the assumption that a decrement in available ductility, resulting from a period of fatigue cycling, can be represented directly as an increment of creep damage. The fatigue component is represented as a log-linear relationship between total strain range and life:

$$\Delta \epsilon_T = K \left(N_f \right)^{-1/a} \tag{23}$$

where:
$$K = \left[\left(2 \, \epsilon_F \right)^a / \, 4 \right]^{1/a}$$

$$2 \, \epsilon_F = 1/4 \text{ cycle ductility}$$

The decrease in available ductility produced by one fatigue cycle is then written as:

$$\Delta \epsilon = \epsilon_{FR} \left\{ 1 - \left[1 - 4n \left(\frac{\Delta \epsilon_T}{2 \, \epsilon_{FR}} \right)^a \right]^{1/a} \right\} \tag{24}$$

Assuming that creep increment can be described by a power law relationship as:

$$\Delta \epsilon_{CR} = At^b \tag{25}$$

The equivalent fatigue time increment is

$$t_f = \left(\frac{\Delta \epsilon}{A} \right)^{1/b} \tag{26}$$

the decrease in the total ductility associated with creep and fatigue damage assumes that the time increments can be combined as:

$$\epsilon_{FR} = \epsilon_{Fi} - A(t_f + t_{creep})^b \tag{27}$$

76

where: ϵ_{FR} = residual ductility at end of increment i

ϵ_{Fi} = initial ductility at beginning of increment i

Equations 24, 26 and 27 are evaluated on a cycle by cycle basis until the original ductility is exhausted. Because of the combined time increments raised to a power, the exhaustion process is highly non-linear.

This approach was originally developed for a situation of gross section (load controlled) creep super imposed on fatigue cycling. Application to an integrated time dependent (creep-fatigue) strain controlled loading cycle required several assumptions on the interpretation of the creep damage equation. These cycles represent a variable stress loading cycle. In addition, the times associated with the various fatigue cycles are significantly shorter than the typical time normally associated with steady state creep. For generality, the creep law used in the model was written as

$$\epsilon_{CR} = C\sigma^m t^{B\sigma^n} \qquad (28)$$

where B, C, m, n are temperature dependent constants. During the course of the evaluation, several measures of the stress and time values of the fatigue cycles were considered. As an example, consider the prediction of the data set shown in Table V below.

Table V
Data Set for Evaluation of Ductility Exhaustion Model
871°C (1600°F), R_ϵ=-1, $\Delta\epsilon$=0.5%

$\dot{\epsilon}$ = 1.67E-04 sec^{-1} 7 points
$\dot{\epsilon}$ = 0.83E-04 sec^{-1} 3 points

From the observed cycle hysteresis loops, the value of the stress for determination of the creep damage was calculated as:

$$\sigma\,eff = \frac{\sigma_T - 20}{2} \qquad (29)$$

Where: σ_T = maximum tensile stress at 1/2 N_f

This represented an average tensile stress for these cycles. A time increment equal to 1/2 of the cycle period was used to calculate the creep damage increment per cycle. As shown in Figure 59, the prediction agrees closely with the tests run at a strain rate of $\dot{\epsilon}$=1.67 -04 S^{-1} while the slower tests ($\dot{\epsilon}$=.83E-04 Sec^{-1}) are consistently overpredicted. These results suggested that the increase in time dependent (creep) damage per cycle was not sufficiently predicted by equation 28, the average tensile stress and the larger cycle period alone. Use of a larger stress magnitude would increase the time dependent damage and improve the correllation between predicted and actual lives for these cycles, but would also reduce the predicted lives for the faster strain rate test points as well. Further evaluation of the stress for calculation of the creep damage considered the Larson-Miller Parameter.
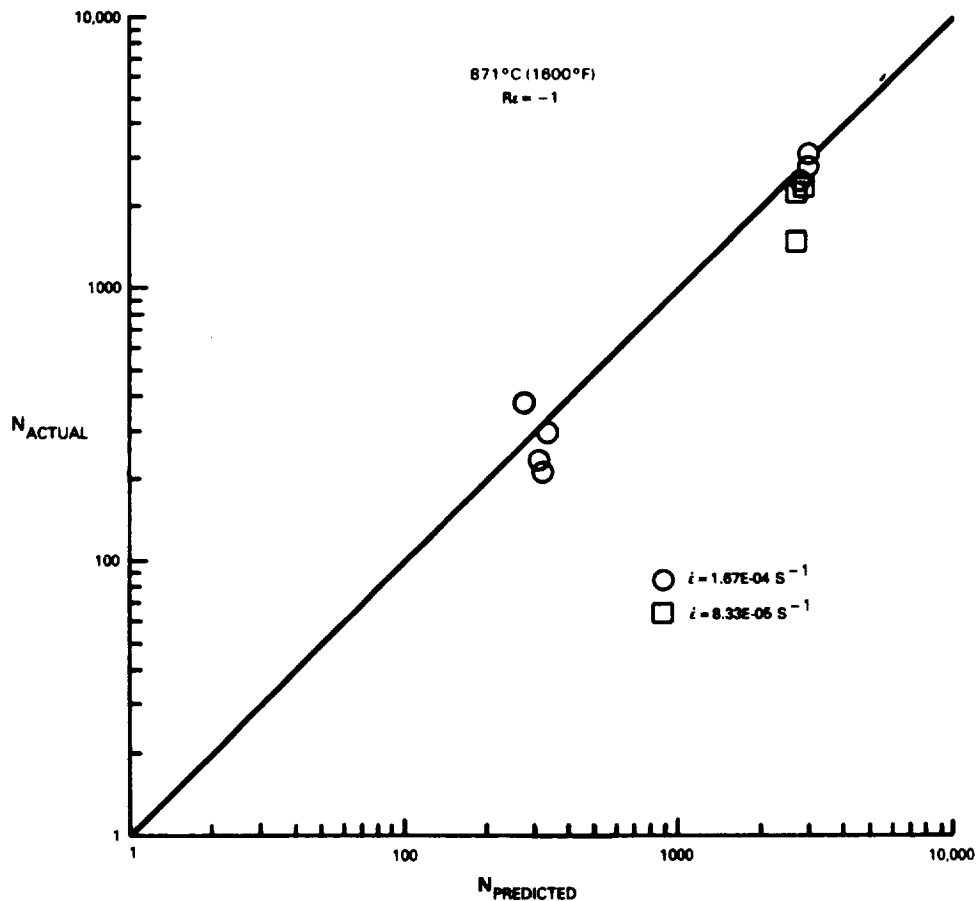
Figure 59 Prediction of Continuous Cycling Tests by the Ductility Exhaustion Approach

In Figure 60, the Larson-Miller parameter (P) for all fully reversed fatigue tests are plotted vs. maximum tensile stress. The time constant (t) used in P represents the time to a 0.030" crack as determined from replica data. Also
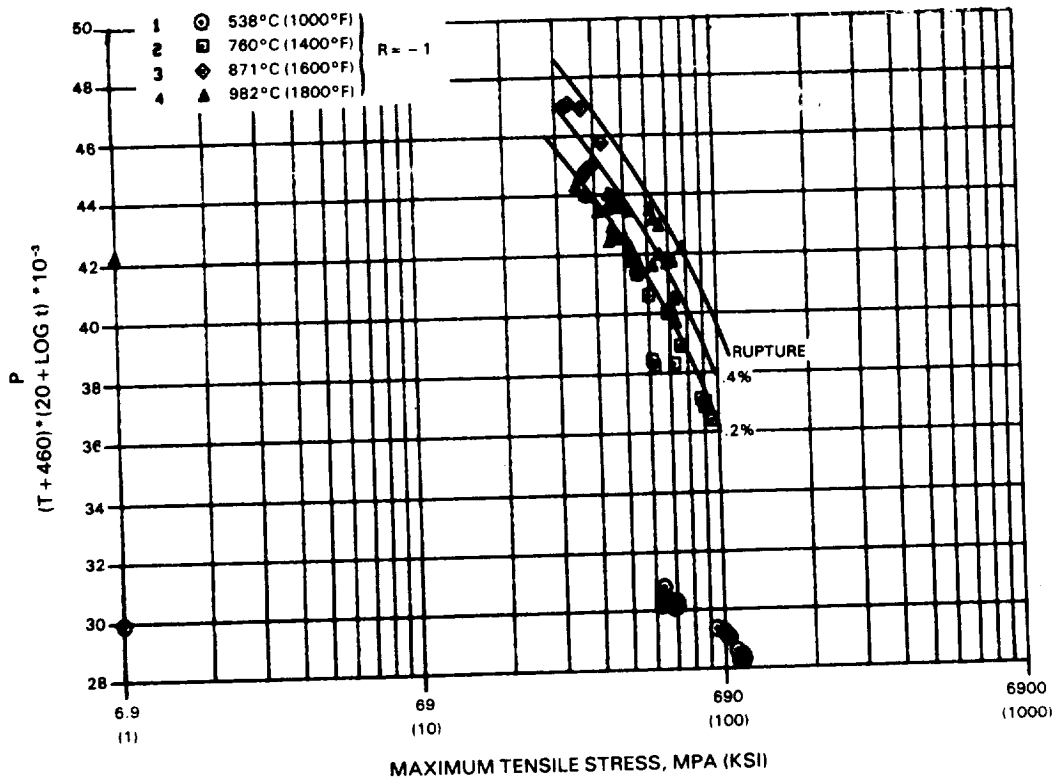
Figure 60   Larson-Miller Curve Representation of Fatigue Data Using Maximum
Tensile Stress

shown in the figure are the creep curves representing 0.2%, 0.4% and rupture
as determined from the monotonic creep tests. The 0.2% and 0.4% creep limits
are considered to represent the approximate magnitude of the grain "ductility"
that is exhausted prior to transgrannular crack initiation. As shown, the
higher temperature tests clearly fall within the creep curves while the lower
temperature tests have a lower P parameter relative to the creep lives. Not
surprisingly, this indicates that the fatigue lives are less influenced by
creep at lower temperatures. In Figure 61, the same data is shown, however,
the stress associated with each test is the average of the mean and maximum
tensile stresses. The reduction in the stress magnitudes shifts the points
away from the creep curves and would be consistent with a much smaller grain
"ductility". Varying the definition of initiation time (t) does not have a
significant effect on the position of the data points relative to the creep
curves as a change in the parameter (P) of 2 points is associated with an
order of magnitude change in the time. Based on these observations and the
assumption of the magnitude of the grain ductility, the maximum tensile stress
appeared to be the more appropriate stress level for calculating the creep
damage increments.
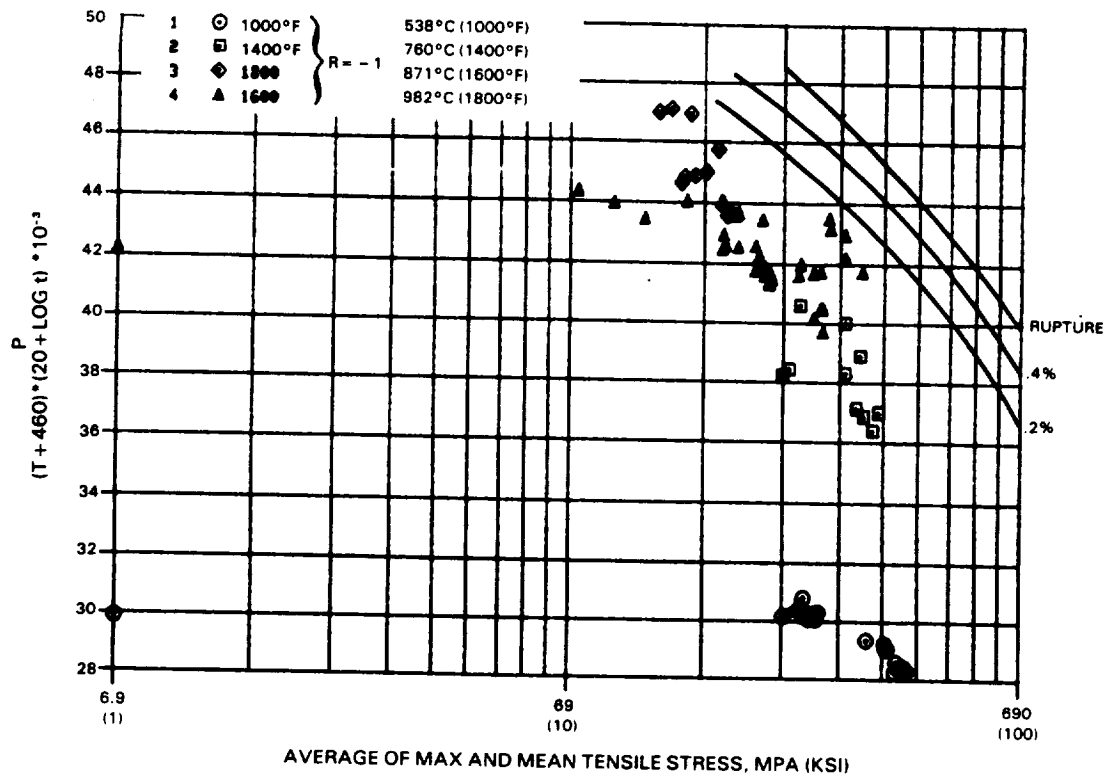
Figure 61   Larson-Miller Representation of Fatigue Data Using Average Tensile Stress

Further evaluation of the model was based on the expanded data set shown in Table VI below. This was considered representative of the life trends throughout the specimen test program. Relative to the fully reversed, rapid cycle tests, life decreases at lower strain rates, is reduced by a compressive strain hold, but increases with a tensile strain hold. The life also generally decreases with increasing (more positive) R ratio with the single exception between R = -1 and R = 0. This effect was associated with a longer nucleation life at R = 0, as a result of the denser dislocation structure produced by the loading to a higher value of stress and is discussed in more detail in Section 3.3.2.

Application of the Ductility Exhaustion Model to this data set is shown in Figures 62 and 63. The fatigue model component was determined from fully reversed (R = -1) rapid cycle ($\dot{\epsilon}$= 1.67-03 Sec^{-1}) data. It was assumed that the creep damage component was produced by the maximum tensile stress in the cycle acting through one-half the transient period plus any strain hold

80

periods. Application of the model to the prediction of a data set, consisting of the slower continuous cycling and strain hold tests from Table VI, is shown in Figure 62. The overall trend in the life is predicted although the consistent underprediction is most likely associated with a too large creep damage component. The model also does not differentiate between the fully reversed tests (R = -1) run at two different frequencies (1 cpm vs. 0.5 cpm)*.

*identified by the filled in symbols

TABLE VI
SUMMARY OF MEDIAN FATIGUE LIVES AT 871°C (1600°F)
$\Delta\epsilon_T = 0.5\%$

Test Condition		Life to 0.030" Crack	Life to 50% Load Drop	Variable
R = -1	1.67-03S^{-1}	1250	3300	Strain Rate
R = -1	1.67-04S^{-1}	920	2750	↓
R = -1	8.33-05S^{-1}	690	2050	
R = -1	1.67-03S^{-1} Compression Hold	570	1700	Hold Times
R = -1	1.67-03S^{-1} Tension Hold	1290	3870	↓
R = 0	1.67-03S^{-1}	1780	4000	R$_{ratio}$
R = 0	8.33-05S^{-1}	510	1525	R$_{ratio}$ (Strain Rate)
R = 1/3	1.67-03S^{-1}	1260	2970	↓
R = -∞	1.67-03S^{-1}	3040	6750	

Application to the rapid cycle tests run at three different R ratios (0, +1/3, -∞) from Table VI is shown in Figure 63. The mean strain effect is clearly not predicted by the model. The lack of predictive capability was expected since the model formulation does not contain a specific "mean strain correction term" or recognize the difference in maximum stress and stress amplitude of these tests relative to a fully reversed test. Prediction of the slower rate (creep dominated) tests but not the rapid cycle mean strain tests or vice versa is characteristic of most life models containing two damage terms. Experience with the Continuous Damage model on the prediction of Hastelloy X creep fatigue tests [25] indicated similar predictive capability. Here, this model contains a explicit mean strain (stress) correction, enabling prediction of these effects; however, the sensitivity of the results to the

81
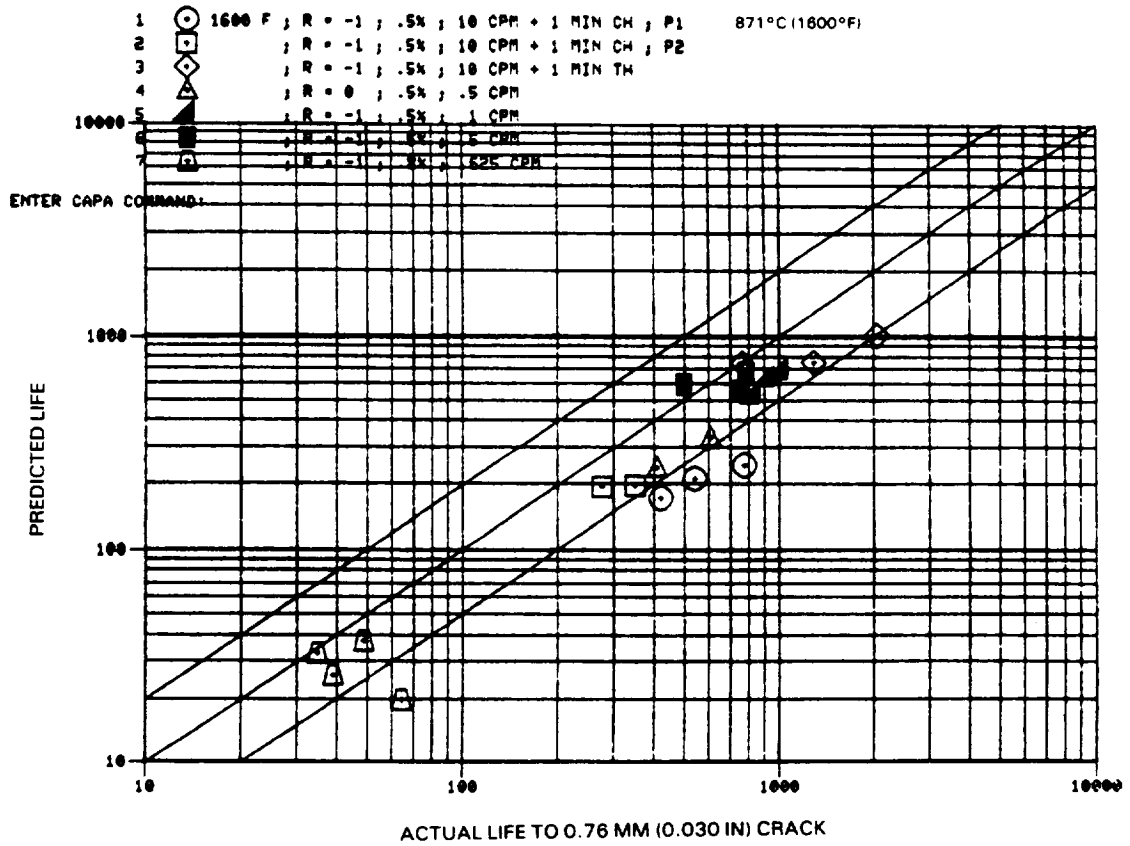
Figure 62 Prediction with Ductility Exhaustion Model
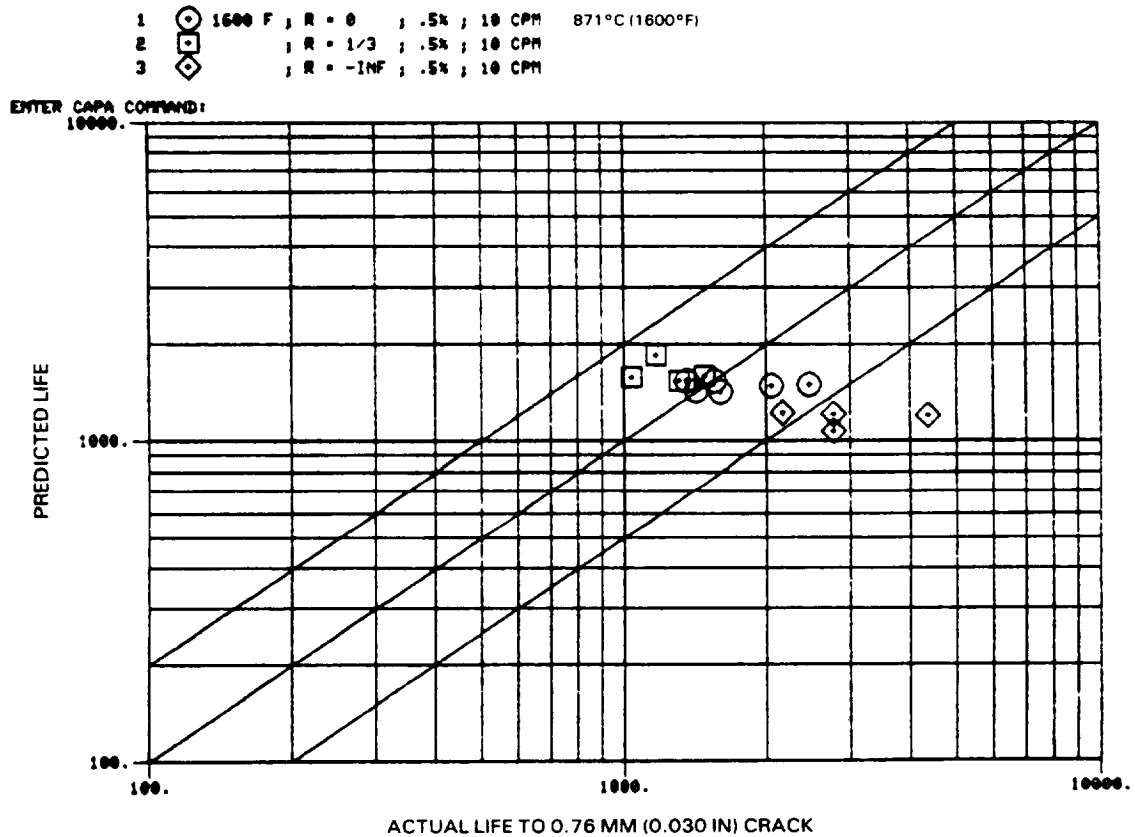
Figure 63 Prediction with Ductility Exhaustion Model

stress and time increments for the creep damage made the continued use of the model unattractive. These observations led to the model proposed in the next section based on the concept of a cyclic damage capability (ductility) that is loading history dependent which is exhausted by the independent and time dependent damage.

3.2.8 Summary of Model Evaluations

The experience with the models, discussed in Sections 3.2.2 to 3.2.7 relative to the ranking criteria presented in Section 3.2.1, suggested that an accurate and useable model for the prediction of crack initiation under creep-fatigue loading conditions should have the following features:

1. Two damage parameters recognizing both time independent and time dependent fatigue mechanisms. As such time (t) should be explicitly included as opposed to frequency or strain ratio.

2. An explicit correction for mean strain or stress. This could also be included in a function which is loading history (path) dependent.

3. Use total mechanical strain range, stress (mean, range, tensile, ...) and temperature as the key variables. For the material (B1900+Hf) and relevant loading cycles considered here, the macroscopic inelastic strain is small and would introduce an additional level of uncertainty in the calculations.

4. Be formulated with damage ratios as opposed to specific damage increments. This would make the prediction relative to a well-defined reference fatigue condition. Use of ratios would reduce the potential error associated with calculation of specific damage, e.g., cyclic time dependent damage using monotonic creep rupture data.

5. Constants for the model should be completely determinable from simple, economic tests, e.g., fully reverse fatigue, tensile, and creep tests.

All of these considerations were used in the development of the model presented in the next section.

3.3 Task III - Evaluate Best Candidate Life Prediction Approach

3.3.1 Basis for Proposed Model

The discussion presented in Section 3.2 indicated that none of the models were able to sufficiently predict all of the trends in life. It was concluded that a more accurate approach could be developed, within the data requirements, by selecting certain characteristics of the previous models and interpreting the available metallographic analysis results. This would not only provide a model for the specific material considered in the base program (B1900+Hf) but potentially be extended to other materials through a qualitative understanding of the critical deformation and damage processes. The metallographic analyses conducted on many of the fatigue specimens indicated that the initiation process (development of cracks up to 0.030" surface length) is primarily transgrannular. This effect is clearly a function of the applied strain rate and temperature as shown by the failure map constructed from the creep, tensile and fatigue tests (Figure 64). From these observations, the fundamental assumption for the development of the model is that the critical fatigue damaging processes occur within the grains. Conversely, the critical process occurs (or accumulates) within the grain boundaries for those failures that are intergrannular. Given these assumptions, a substantial amount of examination was conducted to establish a qualitative assessment of the deformations observed in various fatigue, tensile and creep tests. This information was used to develop a procedure for a quantitative measure of the grain (and grain boundary) ability to absorb cyclic damage. The crack initiation process is then considered to be an exhaustion of the capability by the subsequent fatigue cycling.

3.3.2 Proposed Interpretation of Material Deformation

The damage capability is assumed to be related to the grain dislocation structure and, as such, the entire loading history must be considered in its determination. As an example, fully reversed fatigue tests ($R\epsilon$= -1) of B1900+Hf conducted at relevant strain ranges display little macroscopic inelastic strain. Examination of specimens shows a sparse dislocation network
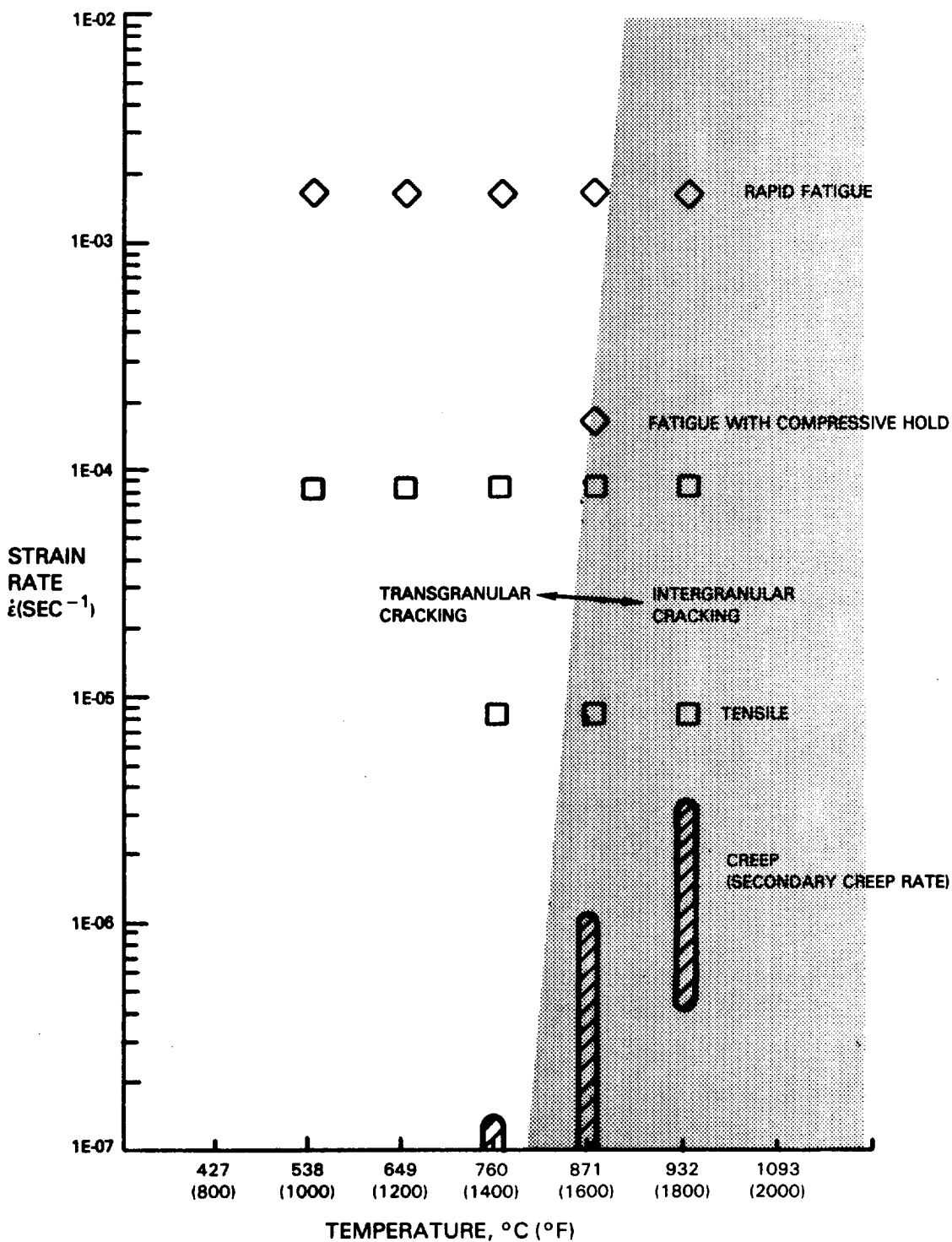
Figure 64 Preliminary Cracking Map for B1900+Hf

within the grains, e.g., Figure 65 A, 871°C (1600°F), $\Delta\epsilon$ = 0.5%, $\dot\epsilon$ = 1.67E-03 sec^{-1}. For this cycle, the initial straining out to maximum or minimum strain ($\pm$ 0.25%) results in local dislocations within the grains. The symmetrical nature of the cyclic loading does not create additional dislocations and in effect "works" the original structure ultimately producing a crack within the grain. For an unsymmetric cycle (Figure 65 B, R = 0) the initial loading out to the maximum strain limit produces significantly more macroscopic inelastic strain consistent with a denser dislocation structure. If the subsequent cycling does not exceed the previous maximum stress (shear), additional dislocations are not produced and the fatigue damage accumulates on the existing structure. This might be seen in Figures 66 (A, B, C) for a cycle between zero and +0.5% strain. During the initial load cycle (Figure 66 A) a dense structure is generated consistent with the macroscopic inelastic strain. This structure is considerably different than that produced by a fully reversed test of the same strain range; e.g., compare Figure 66 C with Figure 65 A. Subsequent cycling of another specimen for 70 fatigue cycles (Figure 66 B) shows an intensification of the dislocations but effectively no additional networks. Finally, cycling of a third specimen for 3450 cycles (Figure 66 C) shows effectively the same structure. Thus, it was assumed that the dislocation network which "absorbs" the fatigue damage is established during the initial loading prior to the cycling.

Fatigue cycles that include a large component of time dependent damage (e.g. strain holds or lower strain rates) displayed a grain dislocation structure resembling that observed in a monotonic creep test. As an example, Figure 67 compares the dislocation structures for a 871°C (1600°F), $\Delta\epsilon$= 0.5% with a one minute compressive strain hold vs a creep test and a slow continuous cycle test. These observations suggested that 1) the material grains experience a significant amount of deformation during creep and 2) a potential relationship exists between the dislocation structure that develops during fatigue cycling and that which evolves during the creep deformation. Development of a quantitative function for the determination of grain cycle capability from creep data further considered the fact that the dislocation structure is a function of the applied stress level. Figure 65 A and 66 A showed the increase

86

(A)
982°C (1600°F), R = 1

(B)
982°C (1600°F), R = 0

Figure 65   Comparison of Dislocation Structures at Two Mean Strains

(1600°F, $\Delta\epsilon$ = 0.5%, R = 0, $\dot{\epsilon}$ = 1.67E-03 S^{-1})

(A)

1 cycle

σ 90 ksi ϵ

(B)

70 cycles

σ 70 ksi ϵ

(C)

3450 cycles

σ 70 ksi ϵ
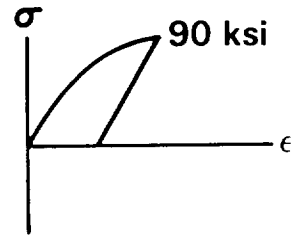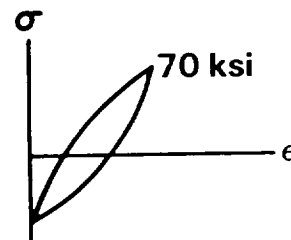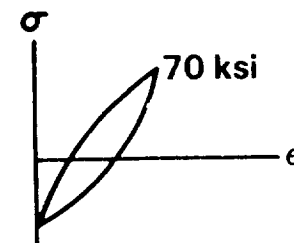
Figure 66   Character of Dislocation Structure Determined by Maximum Stress

● 871°C (1600°F) creep and fatigue are similar
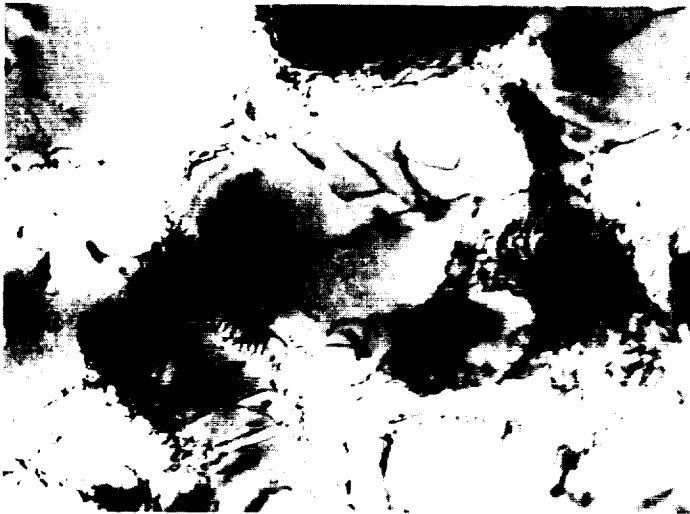
Creep

$\Delta\epsilon = 0.5\%$
$\dot{\epsilon} = 8.3E{-}05\,S^{-1}$
$R = -1$

$\Delta\epsilon = 0.5\%$
1 min hold
$R = -1$

Figure 67 Grain Deformation Observed in Creep

88

in dislocation structure with stress level associated with the first loading cycle of a fatigue test. Interpretation of the monotonic creep response assumed that the nonlinear or primary creep was associated with grain deformation. Evidence that primary creep strain is dominated by grain damaging mechanisms is cited by several authors. Min [26] suggests that the grain matrix deformation process at high temperature is a non-linear time dependent response which is a good description of the primary creep response. Chambers et al [27], in studying the effect of prior creep exposure on fatigue life for IN738 concludes that pre-exposure to creep strain levels equivalent to the point where transition to minimum creep strain rate occurs (e.g., end of primary creep response) is the strain level required to seriously degrade the fatigue properties.

A review of the B1900+Hf creep response at 760°C (1400°F), 871°C (1600°F), and 932°C (1800°F) indicated that a linear relationship existed between the applied stress level and the amount of primary creep strain. These results are presented in Figure 68 and indicates that the amount of primary creep is an inverse function of the temperature. This would appear to be consistent with the notion of relative grain and grain boundary strengths (equicohesive temperature) and the observation that lower temperature failures are almost exclusively transgrannular. Thus, one of the fundamental assumptions of the proposed approach is that the grain cyclic capability can be calculated from the maximum stress attained in the initial loading cycle and the amount of primary creep strain that could have been developed if the stress level were held constant. Since the observed primary strain is bounded at lower stress levels, it seems reasonable that higher stress levels (produced by cycles with larger positive or negative mean strains) would saturate the grain and then produce deformation in the grain boundaries. This assumption was supported by two observations. At 871°C (1600°F), stress levels approaching 95 KSI resulted in "slip bursts" in the stress-strain response (see Figure 69). This was interpreted as an indication of saturation of the grain and discontinuous movement of the grain boundaries. At 760°C (1400°F), the boundaries are considered to be significantly stronger than the grains. In both the tensile and creep tests (see Figure 20b), twins were observed in the grains at
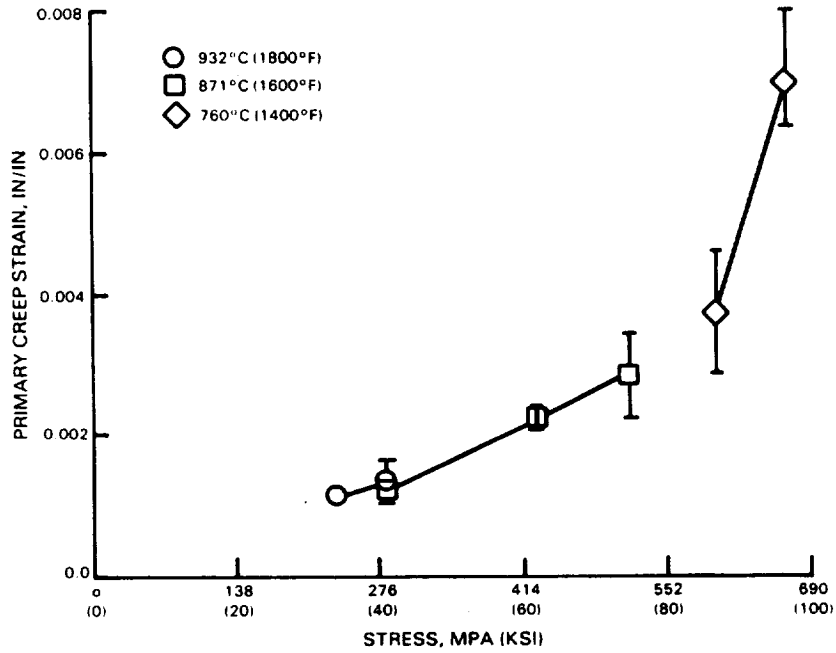
Figure 68   Primary Creep Strain is a Linear Function of Stress
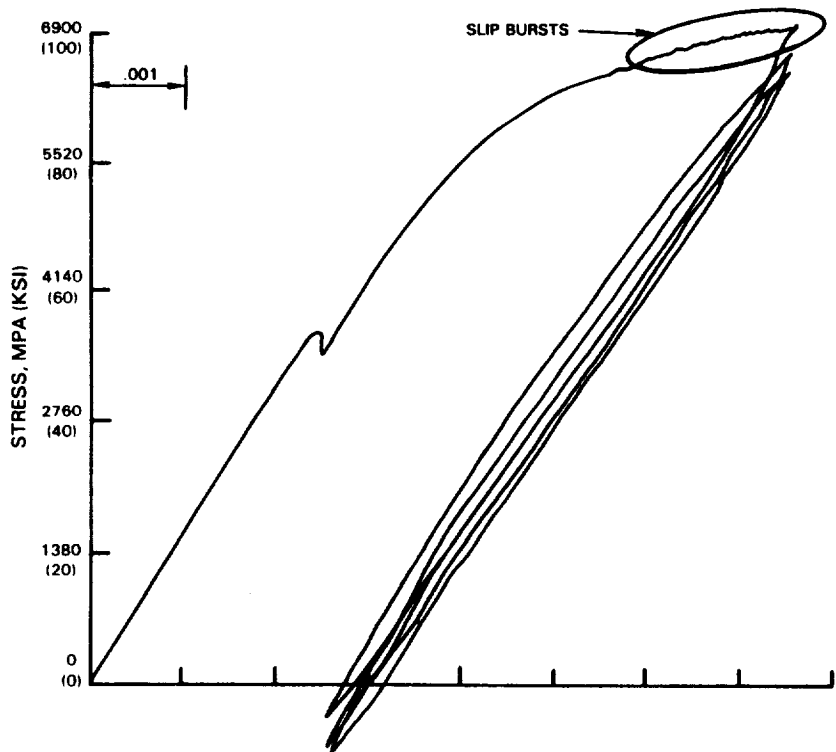
Figure 69   Observation of Slip Bursts at High Stress Levels

moderate levels of inelastic strain. This was interpreted as a relief mechanism in light of the strong grain boundaries. Thus, the determination of the grain cyclic capability required a partitioning of the initial deformation to reflect both grain and grain boundary deformation.

At temperatures ≤ 649°C (1200°F), creep within the context of the fatigue cycles is non-existent. Comparisons of the lower temperature fatigue dislocation structures indicated some similarities with the monotonic tensile tests (see Figure 70). It was therefore assumed that the residual inelastic strain (percent elongation) measured after a tensile test could be considered as a measure of the grain cyclic capability. This was considered independent of stress level within the fatigue test. A representation of the assumed grain cyclic capability vs temperature and stress is presented in Figure 71.

3.3.3 Grain Damage Equation

Since a grain based capability has been assumed, it seems reasonable that a ductility exhaustion (or damage accumulation) approach be utilized for modeling the initiation process.

A primary assumption for the development is that the fatigue damage processes which create transgrannular cracks at a given temperature are similar among all transgranularly initiated test conditions, and a single test condition can be used to set a reference cyclic damage rate. Any other cyclic damage rate can then be calculated by ratioing the reference cyclic damage rate to the new condition.

The proposed functional form of the damage accumulation model is therefore:

$$\text{Cyclic Capability} - \int \underbrace{\frac{dD}{dN}}_{\text{Cyclic Damage Rate}} dN = 0 \tag{30}$$

$$\text{Where } \frac{dD}{dN} = \left.\frac{dD}{dN}\right]_{Ref} \times [\text{Damage Ratios}]$$

91

538°C (1000°F)
tensile
$\epsilon = 1.5\%$

538°C (1000°F)
$\Delta\epsilon = 0.5\%$
$\dot{\epsilon} = 1.67E\text{-}03\ S^{-1}$
$R = -1$

Figure 70   Low Temperature Fatigue and Tensile Deformation are Similar

92
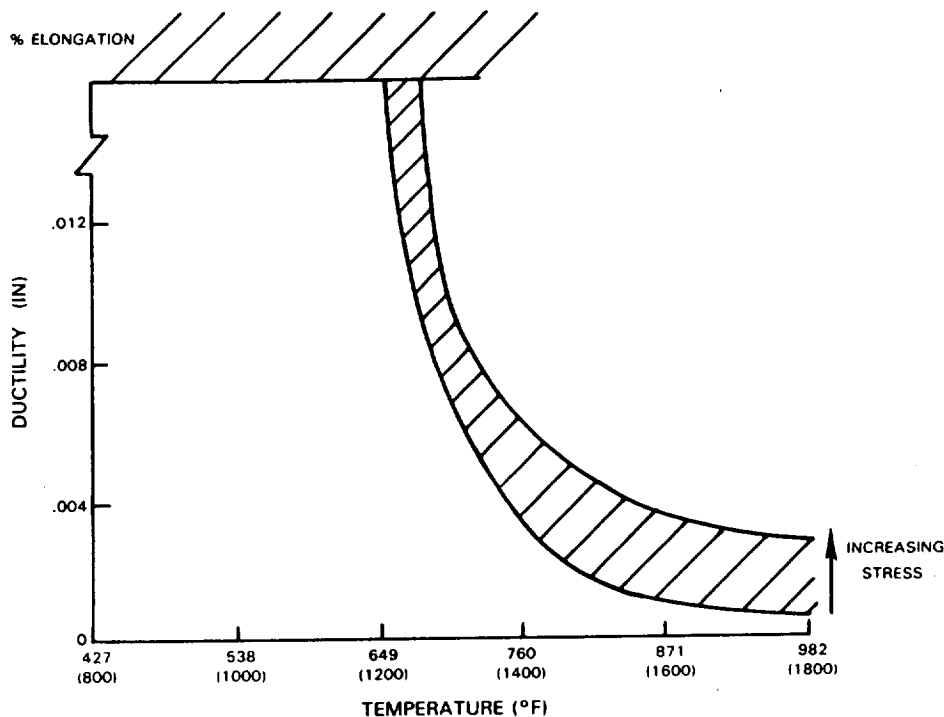
Figure 71   Assumed Grain Cyclic Fatigue Capability

The reference damage rate is determined from fully reversed (R_ϵ = -1) fatigue tests and is illustrated in Figure 72. The maximum tensile stress (σ_T), stress amplitude ($\Delta\sigma$), and observed crack initiation life (N) for these cycles are considered as reference parameters. The grain capability ($\bar{\epsilon}$ p) associated with the cycle is determined from $\sigma_{T\ Ref}$ and Figure 71. Thus the reference damage rate is the only parameter in the proposed model requiring fatigue test data and is calculated as:

$$\left.\frac{dD}{dN}\right]_{Ref} = \left.\frac{\bar{\epsilon}p}{N}\right]_{Ref} \tag{31}$$

This damage rate is obviously a function of the total strain range and can be represented as:

$$\left.\frac{dD}{dN}\right]_{Ref} = A\ \Delta\epsilon_T^{\ B} \tag{32}$$

Determination of the damage rate for other fatigue conditions evolved from examination of the trends in fatigue life with major cycle parameters. As an example, a plot of 871°C (1600°F) rapid fatigue data, at a strain rate of $\dot{\epsilon}$ = 0.001667 in/in/sec for various mean strain levels, shown in Figure 73(A) suggests that time independent fatigue damage is proportional to maximum tensile stress (σ_T) and stress range ($\Delta\sigma$).

93

$$\frac{dD}{dN}\bigg]_{Ref} = \frac{\bar{\epsilon}P(\sigma R)}{N_R} = f(\Delta\epsilon)$$
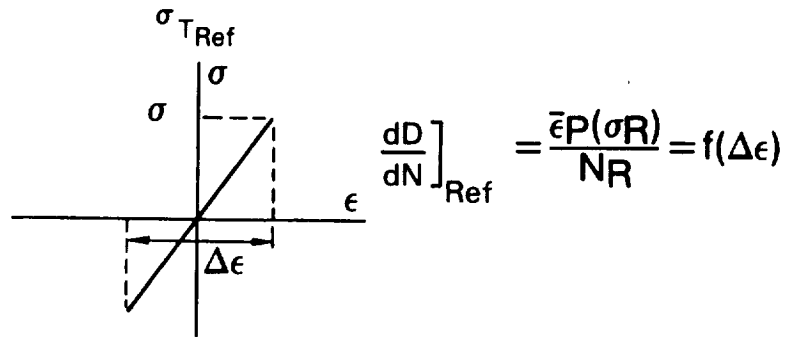
Figure 72 Fundamental Form of Reference Cyclic Damage

$$\frac{1}{N} \; \alpha \; D_{Ind} \; \alpha \; \sigma_T \; \Delta\sigma \tag{33}$$

As shown, a fixed value of stress amplitude combined with increasing maximum tensile stress produces lower initiation life. From 73 B, this is associated with shifting the hysteresis loop to a more positive mean strain which intuitively results in lower life. Conversely, maintaining a constant maximum stress, but decreasing the stress amplitude produces an increase in life. This is possible by decreasing the strain range which again is consitent with longer life. Thus, the total time independent cycle damage expression is assumed to be related to the reference condition as:

$$\frac{dD}{dN} = \frac{dD}{dN}\bigg|_{Ref} \left(\frac{\sigma_T}{\sigma_T}\bigg|_{Ref}\right)\left(\frac{\Delta\sigma}{\Delta\sigma}\bigg|_{Ref}\right) \tag{34}$$

For fatigue cycles in which time dependent damage is considered to be important, a review of the data suggests a different damage parameter. Shown in Figure 74 is a summary of the 871°C (1600°F) time dependent and rapid cycle baseline (R ε= -1) tests. These results suggest that the damage is proportional to maximum tensile stress (σ_T) and inversely proportional to stress range ($\Delta\sigma$) and maybe written as:

$$\frac{1}{N} \; \alpha \; D_{Dep} \; \alpha \; \sigma_T \frac{1}{\Delta\sigma} \tag{35}$$

(A)
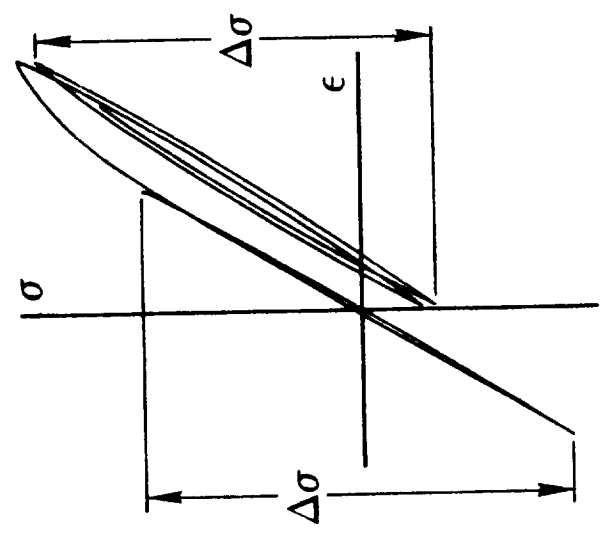
O R = −1; 10 cpm (baseline)
□ R = 0; 10 cpm
◇ R = ⅓; 10 cpm
△ R = −∞; 10 cpm
△ R = −1; 12.5 cpm; $\Delta \epsilon_T = 0.4\%$

(B)
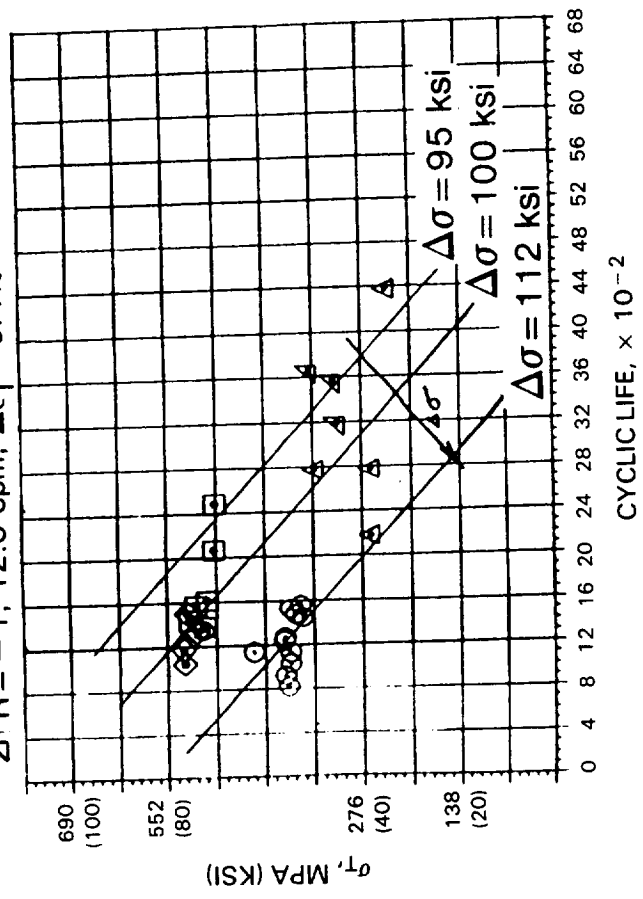
$$D \alpha \, \Delta\sigma \, \sigma_T$$

$$\text{Cycle damage} = \frac{dD}{dN_R} \left(\frac{\sigma_T}{\sigma_{TR}}\right) \left(\frac{\Delta\sigma}{\Delta\sigma_R}\right)$$

Figure 73 Time Independent Damage Ratio Related to $\Delta\sigma$ and σ_T

C-2

Figure 74 Time Dependent Damage Ratio Related to $\Delta\sigma$ and Creep

(A)

o R = –1; 10 cpm (baseline)
□ R = –1; 10 cpm + 1 min C. hold
◇ R = –1; 10 cpm + 1 min T. hold
△ R = 0; 0.5 cpm
⊿ R = –1; 1 cpm
▯ R = –1; 0.5 cpm

(B)

$$D\,\alpha\,\frac{1}{\Delta\sigma}\,\sigma_T$$

$$\text{Cycle damage} = \frac{dD}{dN_R} \left[\left(\frac{\Delta\sigma_R}{\Delta\sigma}\right)\left(\frac{\sigma_T}{\sigma_{TR}}\right)\right]^{B'} \cdot \left[\left(\frac{t}{t_R}\right)^{C'} - 1\right]$$

For these tests, a fixed value of stress amplitude together with increasing maximum tensile stress is consistent with lower initiation life. This agrees with the time independent damage relationship. However, decreasing stress amplitude, at a fixed tensile stress, is consistent with lower life rather than higher life. This is a result of the time dependent damage processes and suggests that the stress parameters do not solely define the damage.

Because primary creep strain is assumed to be a good measure of grain ductility, it was assumed that a creep power law equation correctly represented the relationship between stress, time and damage. Starting with the primary creep relationship:

$$\epsilon_p = A \sigma^B t^C \tag{36}$$

where C can be a function of stress (i.e., $C = D\sigma^E$) and replacing with the time dependent stress ratios from equation 35, the time dependent damage rate term is written as:

$$\frac{dD}{dN} = \frac{dD}{dN}\bigg]_{Ref} \left[\frac{\sigma T}{\sigma T_{Ref}} \left(\frac{\Delta \sigma Ref}{\Delta \sigma} \right) \right]^{B'} \left[\left(\frac{t}{t_{Ref}} \right)^{C'} - 1 \right] \tag{37}$$

Where: $t \equiv 1/2$ of the cycle transient period plus hold times. This expression assumes that cycles in which the time is equivalent to the time of a reference cycle do not contain time dependent damage. This is accomplished by the -1 in the expression in the right hand side of the equation. The exponents B' and C' in equation (37) may not be the same as B and C in equation (36).

Determination of the exponents B' and C' is based on data generated in monotonic creep tests but with the following two considerations. The exponent on stress, B', is determined from strain vs time data in which the origin is set at the beginning of the constant load position of the creep test, as is the normal convention. This reflects the sensitivity of the inelasic strain on the stress. For the exponent on time, C', the same data is used, however, the time origin is shifted back to the beginning of the loading history. This results in the elastic (/E) and inelastic strain being included in the regression.

This has several effects, 1) inelasticity that occurs in uploading at elevated temperatures is included, 2) the measure of time is consistent with that used in the baseline reference tests, and 3) the time plays a greater role in determination of the damage ratio than if the conventional origin were selected. During the course of the model evaluation, use of the exponent C', determined from the conventional origin did not predict the life trends as well as when C' was determined using the shifted time origin. Thus, this approach was considered to represent the time dependent damage relative to the baseline tests. Combining equations 31 and 37 yields the following damage accumulation equation.

$$\int_0^N \frac{dD}{dN}\ dN = \frac{dD}{dN}\Big]_{Ref} \left\{ \left(\frac{\sigma T}{\sigma T_{Ref}} \times \frac{\Delta\sigma}{\Delta\sigma_{Ref}}\right) + \left(\frac{\sigma T}{\sigma T_{Ref}}\frac{\Delta\sigma_{Ref}}{\Delta\sigma}\right)^{B'}\left[\left(\frac{t}{t_{Ref}}\right)^{C'} -1\right] \right\} dN \quad (38)$$

where a cycle by cycle integration is performed to account for evolution of the hysteresis loop.

The entire model can now be written as:

$$\overline{\epsilon}_p - \int_0^N \frac{dD}{dN_{Ref}}\right] \left\{ \left(\frac{\sigma T}{\sigma_{TR}}\right)\left(\frac{\Delta\sigma}{\Delta\sigma_R}\right) + \left[\left(\frac{\Delta\sigma_R}{\Delta\sigma}\right)\left(\frac{\sigma T}{\sigma_{TR}}\right)\right]^{B'}*\left[\left(\frac{t}{t_R}\right)^{C'} - 1\right] \right\} dN = 0 \quad (39)$$

where: $\overline{\epsilon}_p$ primary creep strain ductility

$\frac{dD}{dN}\Big)_{Ref}$ = reference cyclic damage rate

σT = maximum tensile stress

$\Delta\sigma$ = stress range

t = time (total cycle period + hold times)/2

N = cycle number

R = reference condition

B' = exponent on stress in primary creep power law

C' = exponent on time in primary creep power law with shifted time origin

98

This model has been designated as Cyclic Damage Accumulation (CDA). The use of the damage ratios has the advantage of not having to evaluate absolute damage increments per cycle. This is considered to be important for cycles that include significant amounts of time dependent damage due to the uncertainty associated with relating the monotonic creep to the cyclic fatigue process. The equation represents a linear damage accumulation approach as the reference damage rate is assumed constant through the cycle loading and the damage ratios are linearly added. This is considered a good starting point in the initial model evaluation. In addition, the available replica data suggested that the growth process which defined crack initiation appeared as more of a linear process (see Figure 75) as compared to the exponential damage growth equations used in the Ductility Exhaustion [21] or Continuous Damage Models [22].
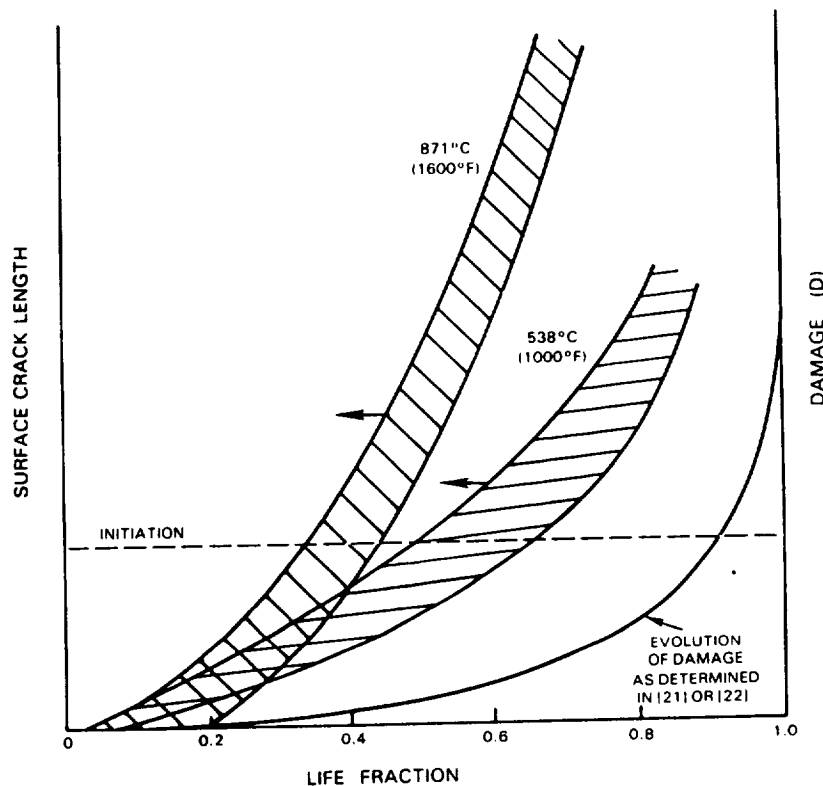
Figure 75   Comparison of Surface Crack Measurements and Evaluation of Damage Parameters

3.3.4 Model Predictions

The CDA model of Equation 39 was used to predict the cyclic crack initiation lives of various mean strain, strain rate, strain hold, and block loading verification tests as depicted in Figure 76. For the predictions, a 0.030" surface crack, which is ≈ 2 grains in depth, was chosen to define initiation.
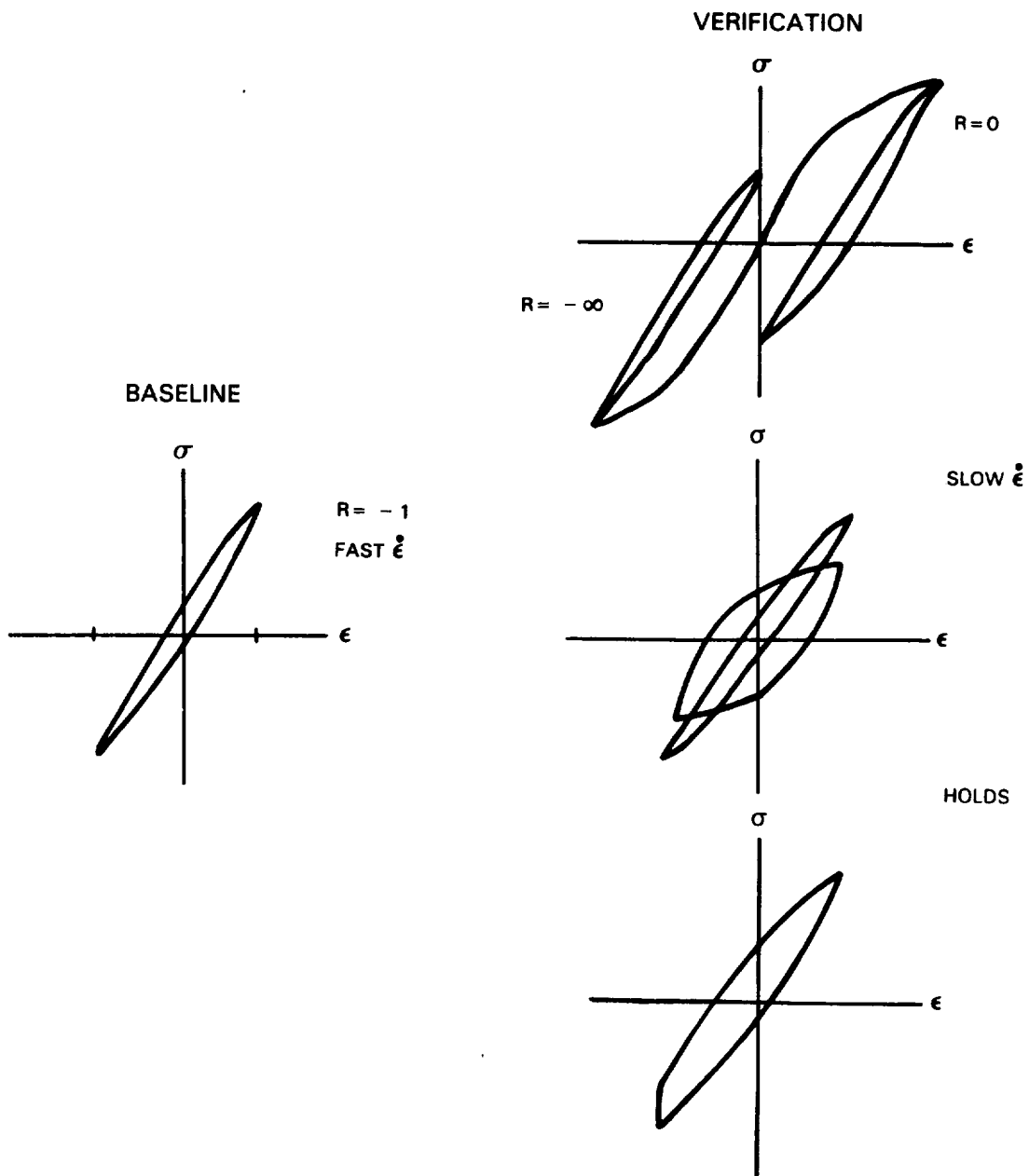
Figure 76   Types of Cycles Used to Demonstrate Model Predictive Capability

Application of Equation 39 to the prediction of B1900 + Hf 871°C (1600°F)
rapid cycle fatigue tests produced the results shown in Figure 77 A. The
prediction of various strain R ratios (ϵ min/ϵ max) demonstrates the trend of
longer life with decreasing mean strain. All test conditions are predicted
within a factor of +2. For test conditions which are not fully-reversed (i.e.,
R ≠ -1), a ductility debit was determined in evaluating the initial grain
capability to account for the non-reversed inelastic strain created in the
first cycle. The method used to determine the ductility debit is discussed in
Appendix II.

100
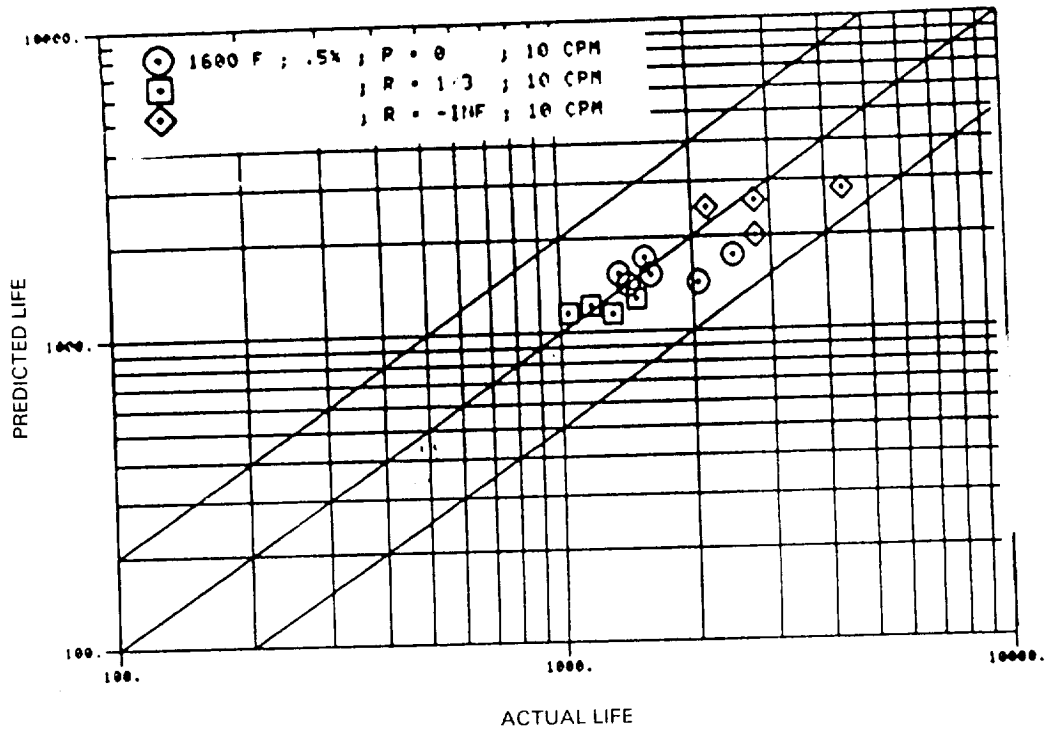
(A)
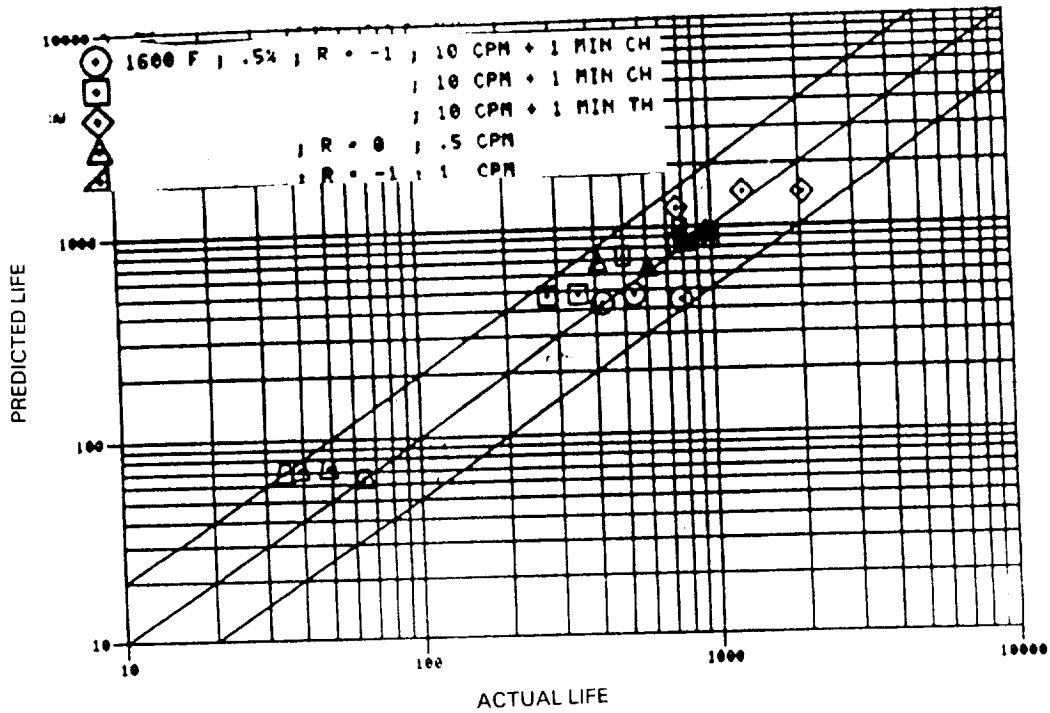
(B)

Figure 77 Mean Strain and Rate Effects Predicted at 871°C (1600°F) - Model
Verification Tests

The ability of the model to distinguish between different loading cycles is further demonstrated in Figure 78. Shown is the measured crack lengths (from replicas) vs. cycles for four (4) types of 871°C (1600°F) rapid cycle tests with a strain range of 0.5%. The data suggests that in the fully reversed (Rε=-1) test the cracks essentially start from the first load cycle. For the other three loading types (Rε=-∞, Rε=0, Rε=0.33), there is a distinct period of little or no crack generation followed by growth at rates that appear to be consistent with maximum tensile stress (i.e. Rε = .33 has the greatest rate, while Rε=- ∞ the lowest). Predictions with the proposed model for the generation of a .76mm (.030") crack are ordered consistent with the data. The net effect of the different time independent damage ratios and grain capabilities, determined for each cycle, may be seen in Table VII where calculated values for four representative specimens are presented. As shown, the initial grain capability varies as a function of the maximum absolute value of stress generated on the first cycle. The damage ratio of the R =-∞ test, which reflects the minimum tensile stress, is less than the fully reversed (R =-1) test due to the compressive mean stress while the ratio for the R =0 and 1/3 tests are greater. It is seen that the cycle with the greatest grain capability also had the largest damage ratio resulting in the lowest life.
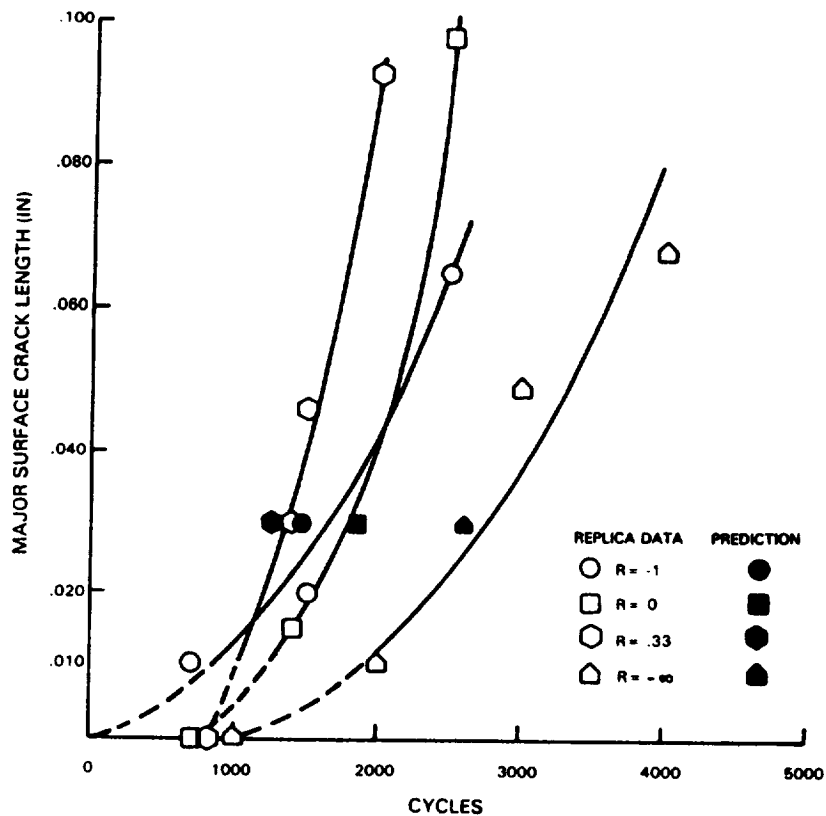
Figure 78 Modified Ductility Exhaustion Approach Predicts R$_{Ratio}$ Effects

102

TABLE VII
VARIATION OF DAMAGE RATIOS AND PREDICTED LIFE
FOR DIFFERENT R RATIO AT 871°C (1600°F)

Spec. ID.	$R\epsilon$ [1]	$\Delta\epsilon_T$ [2]	$\bar{\epsilon}_p$ [3]	$\frac{dD}{dN_{Ref}}$ [4]	DR_i [5]	$DR\ 1/2$ [6]	N_{Pred} [7]
23D	– ∞	.492-02	.295-02	.171-05	0.42	0.64	2560
6A	-1	.50-02	.192-02	.185-05	1.00	1.00	1165
32C	0	.497-02	.353-02	.179-05	1.31	1.04	1726
24A	1/3	.494-02	.375-02	.174-05	1.69	1.11	1141

1. $R\epsilon = \epsilon_{min}/\epsilon_{max}$
2. Total Strain Range, 871°C (1600°F), $\dot{\epsilon} = 1.67\text{-}03\ Sec^{-1}$
3. Grain Capability
4. Reference Damage Rate
5. Time Independent Damage Ratio on First Cycle
6. Time Independent Damage Ratio at Half Life
7. Predicted Initiation Life

Application of the model to the prediction of 871°C (1600°F) cycles which contain time dependent damage is shown in Figure 77 B. These cycles include both rapid transient straining with a one minute tensile or compressive hold period and continuously cycling tests with strain rates that are 10 or 20 times slower than the rapid cycle baseline tests. As shown, the current trends in life are predicted. These results can be further examined in Table VIII where results for one representative specimen of each test type are presented. Relative to a rapid cycle baseline test (specimen 6A), the model predicts the presence of both time independent and time dependent damage. The combination of the two ratios represents the total ratio of damage accumulation. Initially, all four test types are more damaging than the rapid cycle test. At half life, most of the tests still have a combined damage ratio greater than one, but the tensile hold test, due to mean stress relaxation, results in a damage rate that is smaller than the reference (R=-1) condition.

103

TABLE VIII
VARIATION OF DAMAGE RATIOS AND PREDICTED LIFE
FOR TIME DEPENDENT CYCLES AT 871°C (1600°F)

Spec. ID.	$\Delta\epsilon_T$	$\dot\epsilon$ [1]	$\frac{dD}{dN}_{Ref}$	$T_I/T_D i$ [2]	$T_I/T_D 1/2$ [3]	N_{Pred} [4]
6A	.50-02	1.67-03	.185-05	1.0/0	1.0/0	1165
37D	.50-02	1.65-04	.185-05	.79/.32	.75/.28	855
51A	.506-02	833-05	.196-05	.76/.43	.67/.44	728
27B[5]	.503-02	1.67-03	.191-05	.89/.58	.95/1.11	479
22C[6]	.498-02	1.67-03	.182-05	.99/.69	.63/.10	1455

1. Strain Rate Sec^{-1} ($\Delta\epsilon_{Total}$/Total Period)
2. Time Independent Ratio/Time Dependent Ratio on First Cycle
3. Time Independent Ratio/Time Dependent Ratio at 1/2 life
4. Predicted Initiation Life
5. One Minute Compressive Hold
6. One Minute Tensile Hold

Extension of the model to the prediction of fatigue tests conducted at 538°C (1000°F) and 932°C (1800°F) is presented in Figure 79 (A and B). At 538°C (1000°F) time dependent damage is not considered and the reduction in life associated with positive mean strain is correctly predicted. The variation in life with strain rate at 932°C (1800°F) is also predicted. While the 932°C (1800°F) results look encouraging, examination of the failure sites indicated an intergranular initiation mode. The form of the model used for these predictions is based on the exhaustion of a grain capability and theoretically would assume a transgranular mode. Modification of the model to address the failure mode is discussed in Appendix IV.

104
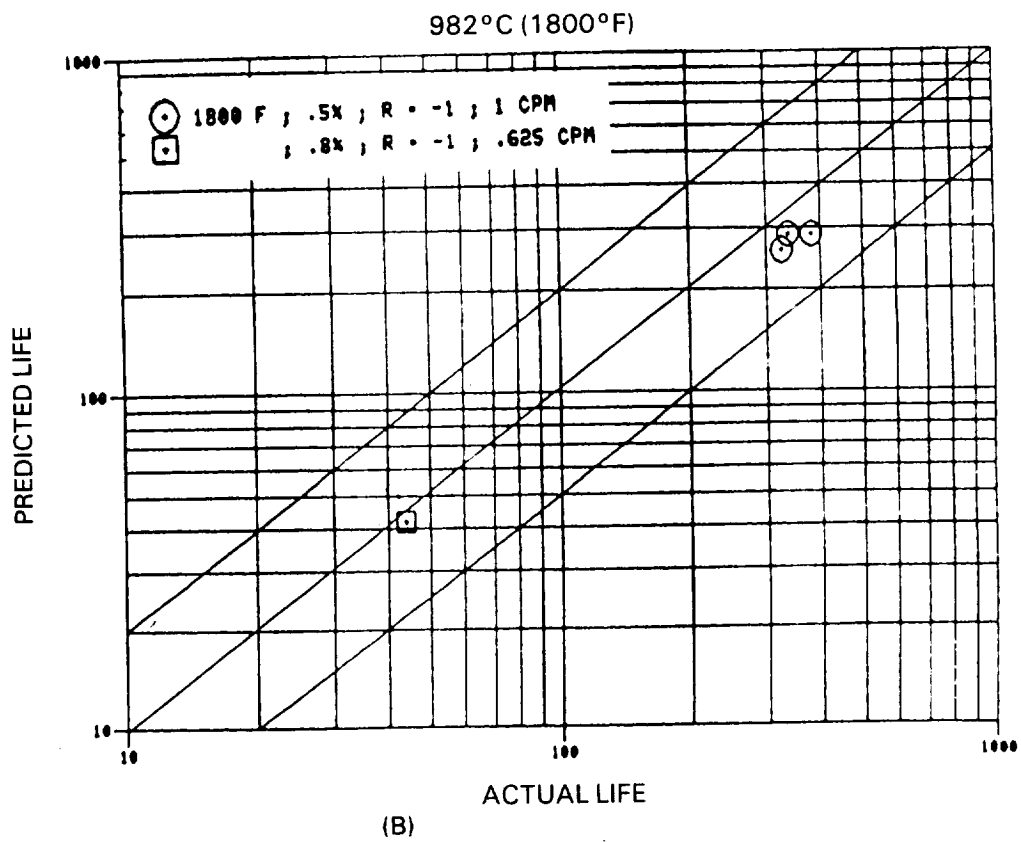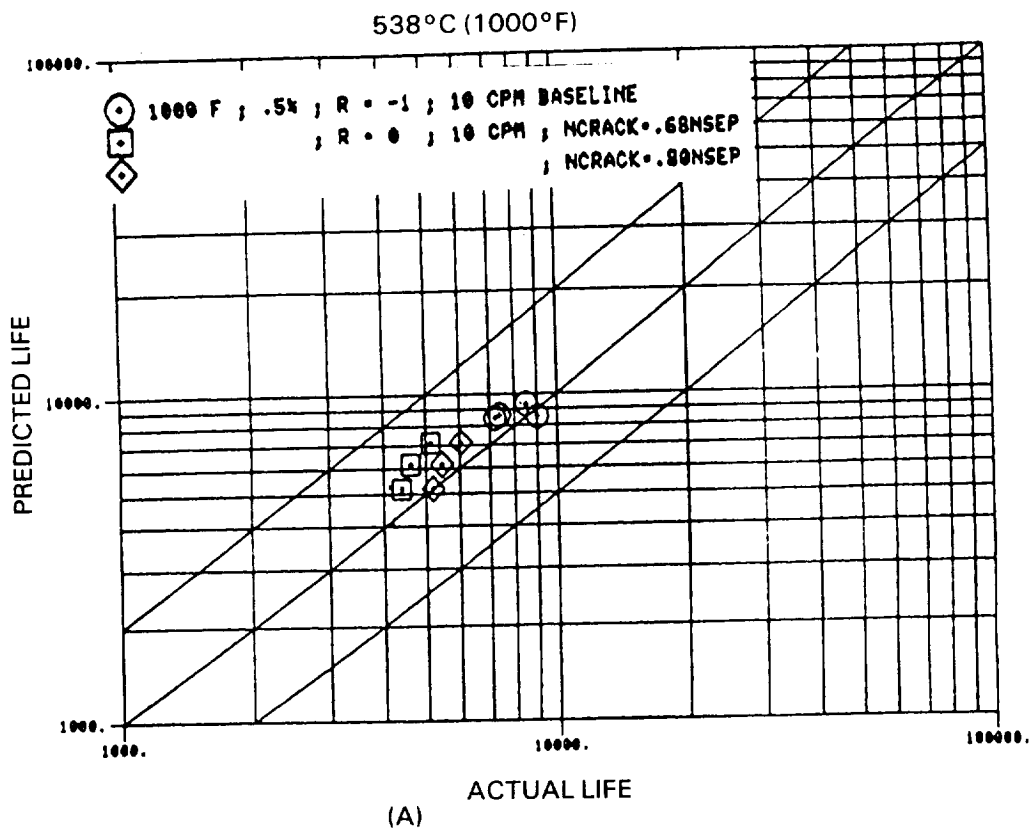
Figure 79   Similar Predictive Capability Delayed at Other Temperatures

To date the model has been applied to simple cycle isothermal fatigue tests and has demonstrated the ability to predict various loading effects, e.g., mean strain, strain rate, strain holds. Application of the model to the prediction of more complex loading cycles considered two types of sequence, or block loading, tests. Initially, four tests were conducted at 871°C (1600°F), at a strain rate of 1.67E-03 sec^{-1}, in which the first cycle was applied between 0 and +0.5% strain. The mean strain was then adjusted from +0.25% to 0% and all subsequent cycling occurred between strain limits ($\pm$0.28%) which produced a maximum tensile stress and stress amplitude consistent with the values that would have been obtained in a test with strain limits of $\pm$ 0.25% without the first cycle overload. This sequence was selected to test the assumption that the grain cyclic capability is determined by the maximum stress in the loading cycle. Per the model philosophy, the initial overload (0 to +0.5%) would result in an increased grain capability which, when coupled with a damage parameter consistent with the fully reversed parameter (equal maximum tensile stress and stress amplitude), would result in a longer initiation life. As shown in Figure 80, the initiation lives of the specimens are longer than would be expected without the first cycle overload and the model successfully predicts the trend in life.

In the second block loading test, the initial cycling at 0 to +0.5% was continued for 600 cylces before making an adjustment in mean strain from +0.25% to 0%, while maintaining the strain range at 0.5%. This series of tests investigated the rate of ductility exhaustion with variable loading. As shown in Figure 80, the model predicted the correct trend in life, however, the predictions are consistently conservative relative to the actual data. A probable cause of the conservative prediction is that the cyclic damage (dU/dN) in equation 39 is too large during the fully reversed position of the cycling. Further investigation of this portion of the model is required and will be considered in future work.

(A)

BLOCK LOADING
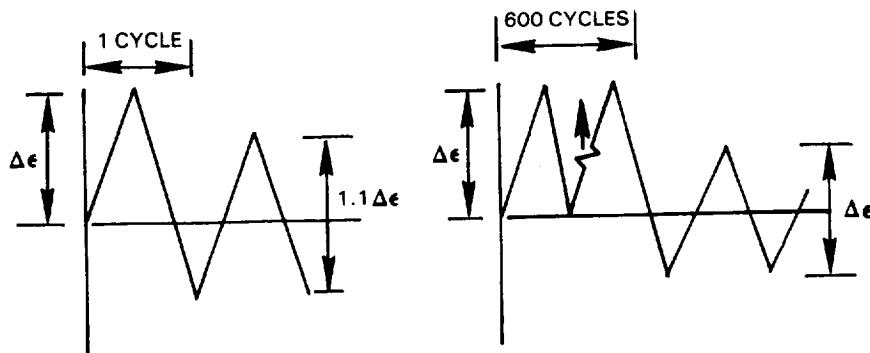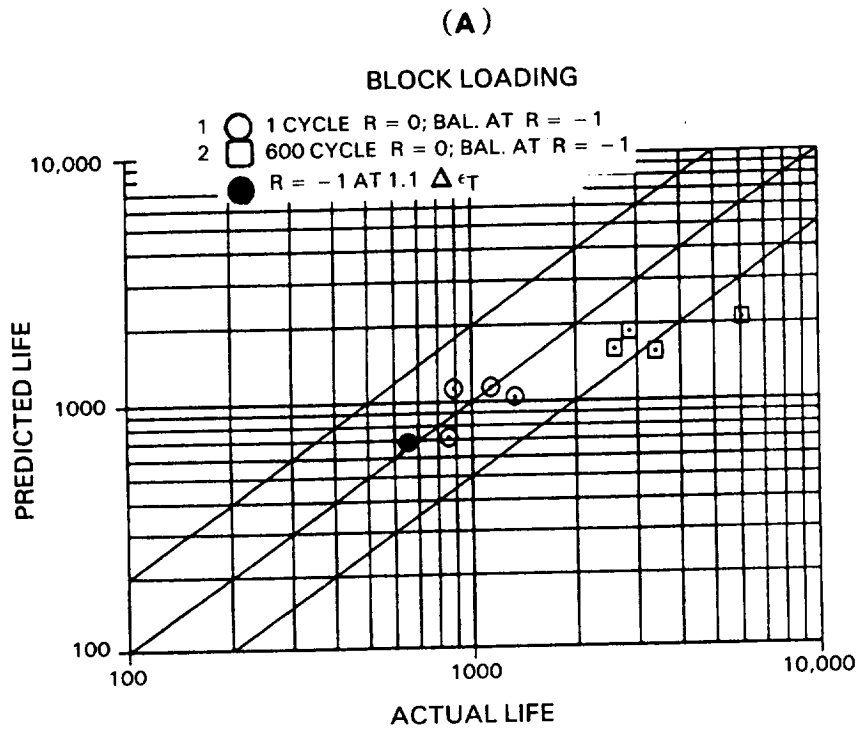
Figure 80 Prediction of Verification Test Cycles

3.3.5 Model Sensitivity Study

An important aspect of any life modelling technique is an understanding of how the prediction capability is influenced by assumptions and specific variables. During development, the following parametric studies were identified which provided insight to overall model performance.

1) Crack size - How does the model prediction capability change for various ratios of initiation crack size to grain size?

2) Crack initiation definition - How does the prediction capability vary as a function of the definition of initiation vs. total specimen separation life?

3) Reference condition - Can the model use an alternative reference condition to predict crack initiation lives?

4) Analysis requirements -How much prediction accuracy is lost if the cycle dependent hysteretic response is unavailable?

To present the results, the Weibull slope and median value of the ratio predicted life/actual life $(\overline{Np}/\overline{Na})$ were calculated for the 871°C (1600°F) data set presented in Figure 77 assuming a variation in each of the four sensitivity areas discussed above. As shown in Figure 81, a larger slope (β) is indicative of less scatter in the predictions. The median life ratio was included to identify consistent trends for under or over prediction.

Crack Size

In the experimental program, special efforts were taken during specimen casting to control grain size to insure specimen isotropy. In actual application, however, grain size may vary from .005" - .150" depending on the various casting constraints. It is, therefore, important to establish how the model predicts cracking lives over a wider range of crack to grain sizes. Utilizing replica data, life fractions for .015", .030" and .060" surface cracks (i.e. crack depths of approximately 1 to 4 grains) were defined to study prediction accuracy as a function of crack size.

The model predictions for a 871°C (1600°F) data set that included both mean strain and creep fatigue conditions are shown in Figure 82. Crack depth to grain size in excess of 2 showed little variation in the predictive capability of the model. For a crack depth on the order of the grain size, a decrease in the Weibull slope and an increase in the median predicted to actual life ratio indicate a loss in prediction accuracy. This was attributed to local non-isotropic single grain effects. A qualitative estimate of model requirements to increase the prediction accuracy for a grain size crack indicated that the primary creep ductility would necessarily have to be larger and more sensitive to applied stress level.

108
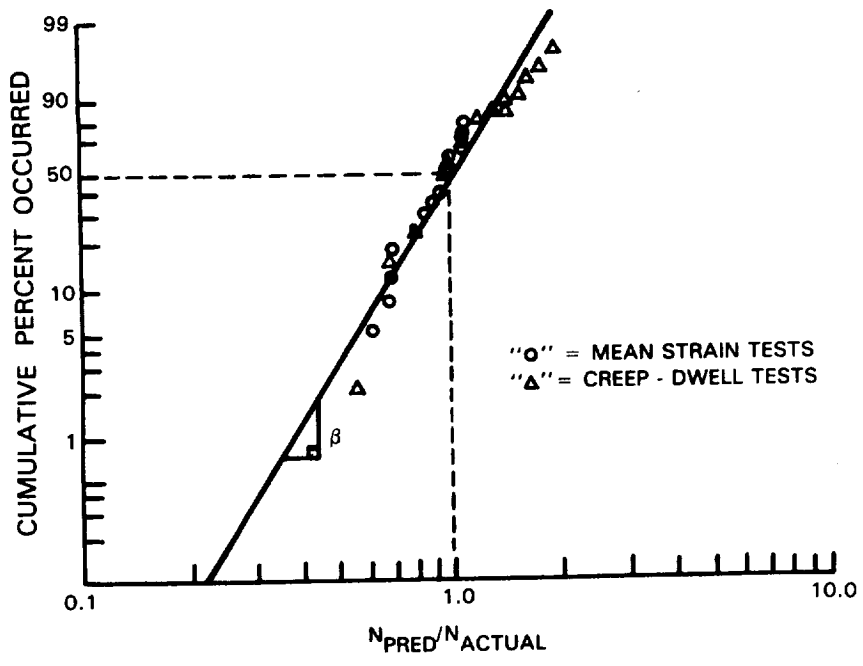
Figure 81   Parameters Used in Sensitivity Analysis
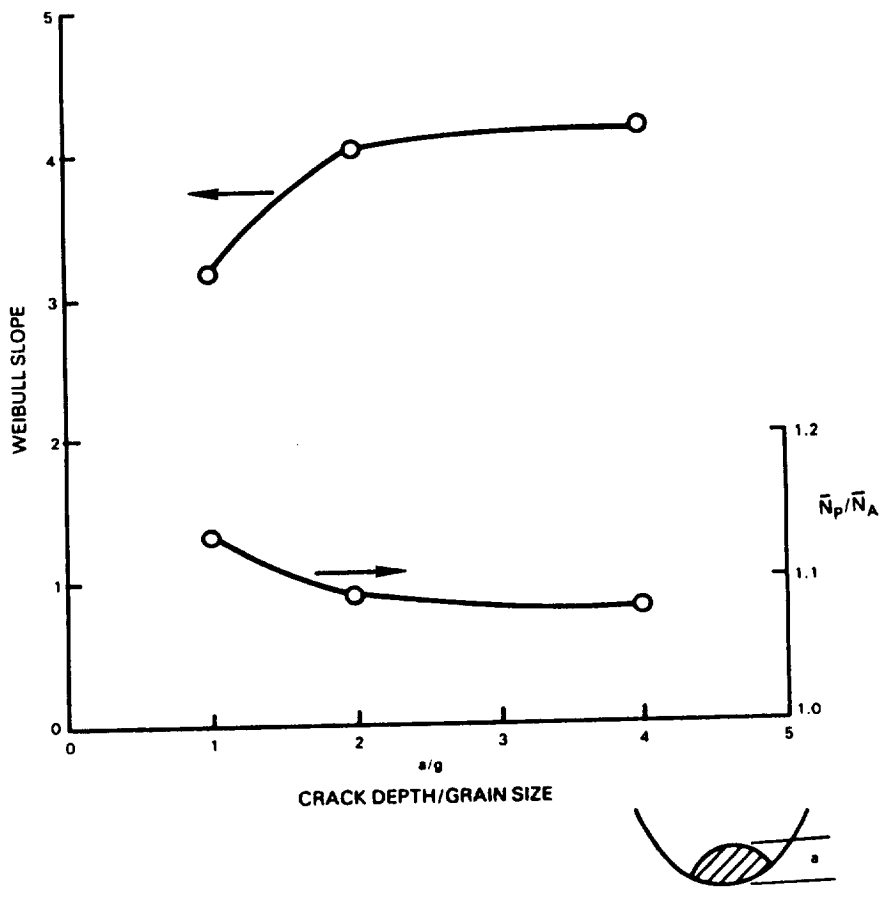
Figure 82   Variation of Predictive Capability with Crack/Grain Size Ratio

Crack Initiation Definition

The crack initiation life for each test specimen was determined from replica data, i.e., several specimens of each test type were inspected to determine an average life fraction (cycles to initiation/cycles to 50% load drop) which was then applied to all specimens tested at that condition. The observed life fractions were similiar but not equal for all test conditions.

To access the change in model prediction accuracy, the 871°C (1600°F) data set (i.e. data of Figure 77 (A and B) was recalculated assuming a .030" surface crack initiated at a constant 38% of the 50% load drop life for all test conditions. This resulted in effectively no change in the Weibull slope and median life ratio. This would suggest that specific life fractions are not necessary for accurate predictions with the model, however, these results may be influenced by the types of loading cycles and the range of life data generated in the program. It is recommended that inspections for definition of crack initiation be continued until the sensitivity of the model can be further investigated.

Reference Condition

The current model assumed fully reversed testing (R = -1) as the reference condition. If this is not available, an alternative reference condition would be required. To quantify the change in the predictive capability with the use of an alternative reference condition, the 871°C (1600°F), R = 0, $\dot{\epsilon}_t$ = .001667 in./in./sec test condition was chosen as a new reference and predictions made of the remaining 871°C (1600°F) data. As shown in Figure 83, the change in reference condition results in a significant loss of predictive capability. A review of the specific test types included in the data set indicated that a large part of the loss of predictive capability was associated with the slow strain rate, creep fatigue tests. This trend is associated with the stress ratio in the time dependent damage term of Equation 39. Since the new σ_{TRef} is high, the stress quantity is $\ll 1$ for the slow cyclic rates. In reviewing Figures 74 and 75, it is evident that the monotonic data responses which allowed the simple ratios of Equations 33 and 35 to be written are not present when the new reference condition is used. Therefore, it was considered necessary to use R = -1, fast cyclic rate data as the reference condition for the current form of the proposed model.

110
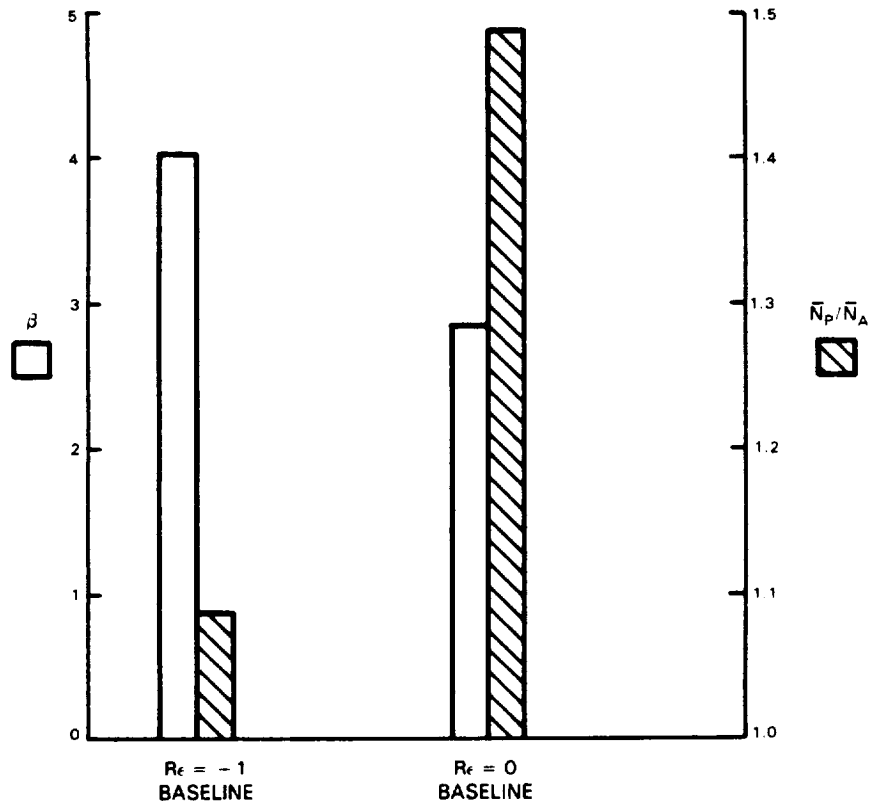
Figure 83   Variation of Predictive Capability with Reference Condition

Analysis Requirements

Within the context of the structural analysis of an actual component, the determination of the complete cyclic hysteresis history may be impractical. More likely, only the cyclic response for the first one or two cycles and an estimate of the stabilized response may be available.

To evaluate the effect of the cyclic response definition on prediction accuracy, the first cycle response and a typical 1/2 life cycle response were individually analyzed for the data of Figure 77 (A and B). As presented in Figures 84, some prediction accuracy is lost by ignoring the cyclic relaxation, however, the model still provides an accurate representation of the data trends.
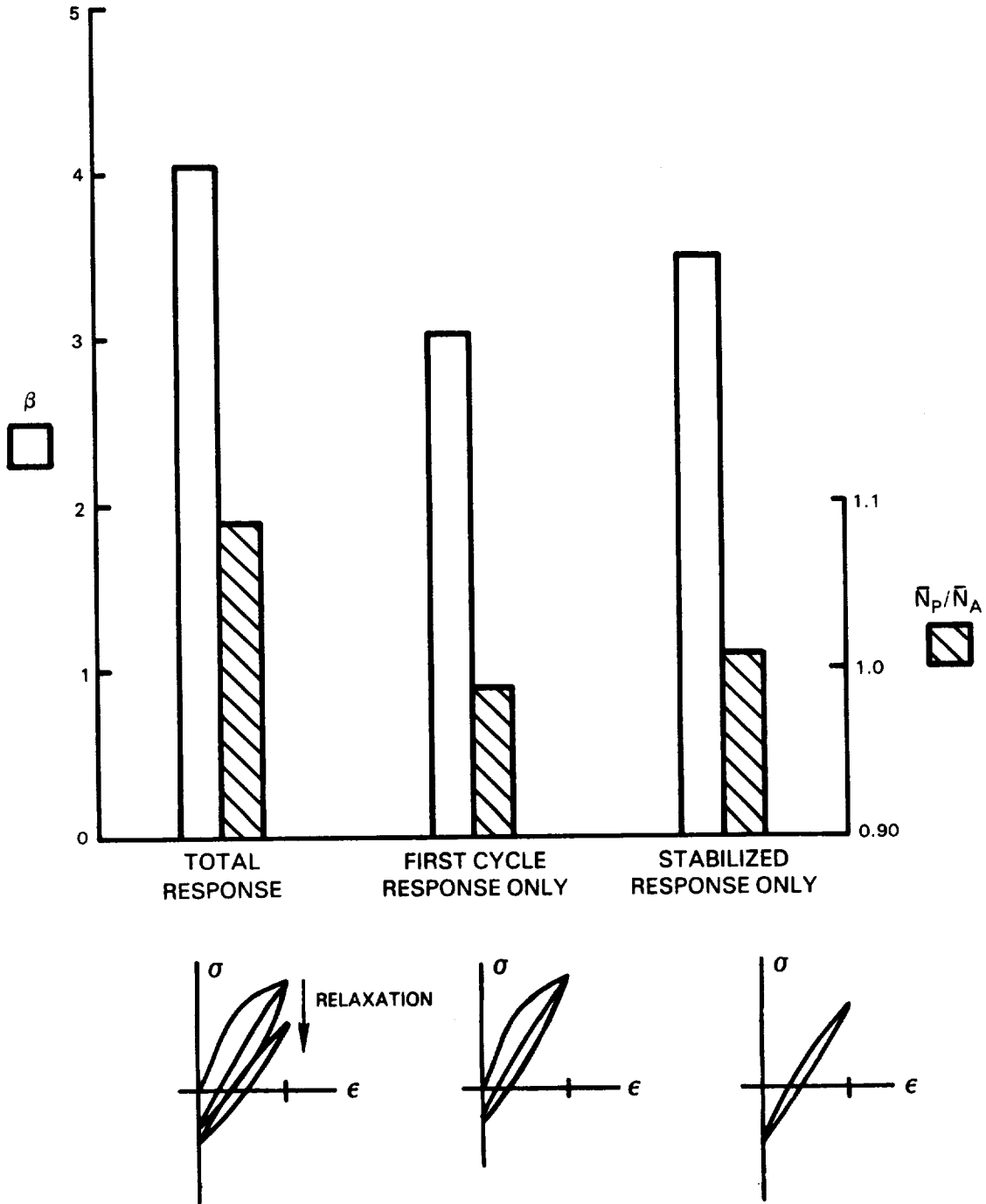
Figure 84   Variation in Prediction Accuracy with Cyclic Response Definition

4.0 Future Work

In the option portion of this contract the evaluation of creep fatigue life models will be extended to more complex loading cycles. Testing, metallographic examinations and model evaluations will include:

1. Thermomechanical loading cycles
2. Multi-axial stress and strain states
3. Cumulative damage loading cycles
4. Environmental effects on fatigue life
5. The interaction of oxidation resistant coatings and the underlying base metal on initiation life.

In addition, life prediction approaches evaluated for the cast material (B1900+Hf) will be applied to the prediction of crack initiation of a wrought material. This will give an indication of the degree of "transportibility" of the models from one material system to another in which the deformation and damage processes differ. A wrought model base alloy (IN718) will be used for the alternate material evaluation.

The CDA approach described in Section 3 will form the basis for these evaluations but other model approaches will be included to address specific aspects of the tests.

REFERENCES

1. Coffin, L.F., "A Review of Fatigue Prediction Methods in the Regime Where Inelastic Strains Dominate", ASME Winter Annv. Meeting, N.Y., N.Y., Dec. 2-7, 1979, pp 1-24.

2. Coffin, L.F., "The Concept of Frequency Separation in Life Prediction for Time-Dependent Fatigue", Symposium on Creep Fatigue Interaction, 1976, pp 349-363.

3. Manson, S.S., Halford G.R., and Hirschberg, M.H., "Creep Fatigue Analysis by Strain Range Partitioning. Symposium on Design for Elevated Temperature Environment, ASME, 1971, pp 12-28. (NASA TM X-67838, 1971).

4. Manson, S.S., "The Challenge to Unify Treatment of High Temperature Fatigue - A Partisan Proposal Based on Strain Range Partitioning. STP 520, ASTM, 1973, pp 744-782.

5. Halford, G.R., Saltsman, J.F., and Hirschberg, M.H., "Ductility Normalized Strainrange Partitioning Life Relations for Creep-Fatigue Life Prediction. Proceedings of Conf. on Environmental Degradation of Engineering Materials. Virginia Tech. Printing Dept., V.P.I. and State University, Blacksburg, VA, 1977, pp599-612.

6. Chaboche, J.L., "Thermodynamic and Phenomenological Description of Cyclic Visco-Plasticity with Damage", European Space Agency Technical Translation, May 1979.

7. Chaboche, J.L., Policella, H., Kaczmarek, H, "Applicability of the SRP Method and Creep Fatigue Damage Approach to the LCHTF Life Prediction of In-100 Alloy", AGARD-CP-243, Technical Editing and Reproduction Limited, London, 19789, pp 4-1 to 4-20.

8. Lemaitre, J., and Chaboche, J.L., "A Nonlinear Model of Creep Fatigue Damage and Accumulation and Interaction". Presented at the Symposium at IUTAM, Sur La Mechnique Des Milieux et Des Cor Viscoelatiques, Gothenburg, Sweden, September 2-6th, 1974.

9. Maiya, P.S., and Majumdar, S., "Elevated-Temperature Low Cycle Fatigue Behavior of Different Heats of Three Type 304 Stainless Steel", Metallurgical Transactions A, Volume 8a, November 1977, pp. 1651-1660.

10. Majumdar, S., and Miaya, P.S., "Wave Shaped Effects in Elevated Temperature Low Cycle Fatigue on Type 304 Stainless Steel", Chang, T.Y., and Krempl, E. (eds.), Inelastic Behavior of Pressure Vessel and Piping Components, PVP-PD-028, ASME, New York, pp. 43-54.

11. Majumdar, S., and Maiya, P.S., "An Interactive Damage Equation for Creep-Fatigue Interaction", Volume 2, ICM3, Cambridge, England, August 1979, pp. 101-109.

12. Bernstein, H.L., "An Evaluation of Four Current Models to Predict the Creep-Fatigue Interaction in Rene' 95", AFML-TR-79-4075, June 1979.

114

13. Manson, S.S., "Behavior of Materials Under Conditions of Thermal Stress. NACA TN-2933, 1953.

14. Ostergren, W.J., "A General Damage Equation for Low Cycle Fatigue Life Predictionat Elevated Tempeature," Rensselaer Polytechnic Institue, Xerox University Microfilms, Ann Arbor Microfilms, No. 76-27,203.

15. Meyers, G.J., "Fracture Mechanics Criteria for Turbine Engine Hot Section Components," NASA CR-167896, May 1982.

16. McKeekiny, R.M., "Finite Deformation Analysis of Crack Tip Opening in Elastic-Plastic Materials and Implications for Fracture," Journal of the Mechanics and Physics of Solids, Vol. 25, 1977, pp. 357-381.

17 Shih, C.F., and Hutchinson, J.W., "Fully Plstic Solutions and Large Scale Yielding Estimates for Plane Stress and Problems," Journal of Engineering Materials and Technology, October 1976, pp 289-295.

18. Trantina, G.G., de Lorenzi, H.G., and Wilkening, W.W., "Three Dimensional Elastic-Plastic Finite Element Analysis of Small Surface Crack," Engineering Fracture Mechanics, Vol. 18, No. 5, pp 925-938, 1983.

19. Halford, G.R., and Saltsman, J.F., "Strainrange Partitioning - A Total Strainrange Version," ASME International Conference on Advances in Life Prediction Methods, 1983, pp 17-26.

20. Halford, G.R., and Nachtigall, A.J., "Strainrange Partitioning Behavior of an Advanced Gas Turbine Disk Alloy, AF2-1DA", Journal of Aircraft, Vol. 17, No. 8, 1980, pp 598-604.

21. Polhemus, J.F., Spaeth, C.E., Vogel, W.H., "Ductility Exhaustion Model Prediction of Thermal Fatigue and Creep Interaction", Fatigue at Elevated Temperature ASTM STP520, American Society for Testing and Materials, 1973, pp 6250636.

22. Chaboche, J.L., "Thermodynamic and Phenomenological Description of Cyclic Viscos-Plasticity with Damage", European Space Agency Technical Translation, May 1979.

23. Chaboche, J.L., Policella, H., and Kaczmarek, H., "Applicability of the SRP Method and Creep Fatigue Damage Approach to the LCHTF Life Prediction of IN-100 Alloy", AGARD-CP-243, Technical Editing and Reproduction Limited, London, 1978, pp 4-1 to 4-20.

24. Lamaitre, J. and Chaboche, J.L., "A Nonlinear Model of Creep Fatigue Damage and Accumulation and Interaction", presented at the Symposium at IUTAM, Sur La Mecanique Des Milieux et Des Corp Viscoelastiques, Gothenburg, Sweden, September 2-6th, 1974.

25. Moreno, V., "Combustor Liner Durability Analysis", National Aeronautics and Space Administration Report, NASA CR 165250, 1981.

26. Min, B.K., "Deformation and Intergrannular Fracture During High Temperature Creep and Creep Fatigue", Vol. 2, ICM 3, Cambridge, England, August 1979, pp 151-162.

27. Chambers, W.L., Ostergren, W.J. and Wood, J.H.", Creep Failure Criteria in High Temperature Alloys", Journal of Engineering Materials and Technology, Vol. 101, October 1979, pp. 374 - 378.

APPENDIX I

SUMMARY OF B1900+Hf FATIGUE TESTS IN BASE PROGRAM

871°C (1600°F) BASELINE SPECIMEN TEST - LIST 1

COLUMN HEADING	- DESCRIPTION	COLUMN HEADING	- DESCRIPTION
SPEC	- SPEC ID	TYPE	- SPEC TYPE 71=A, 76=B, 75=C (see Figure 22)
TEMP	- TEMP.(DEG. F)	DELE	- DEL STRAIN IN/IN
RE::	- RE (EMIN/EMAX)	ERAT	- DEL STRAIN RATE SEC-1
DWLT	- DWELL T (SEC)	DWLC	- DWELL C (SEC)
DEPO	- PSTRAIN RANGE 0	DEPH	- PSTRAIN RANGE 1/2

SPEC	TYPE	TEMP	DELE	RE::	ERAT	DWLT	DWLC	DEPO	DEPH
1B	MERL 71	1600.	0.00500	-1.00	1.67D-03	0.0	0.0	0.00015	0.00023
3B	MERL 75	1600.	0.00500	-1.00	1.67D-03	0.0	0.0	0.00015	0.00023
4B	MERL 76	1600.	0.00500	-1.00	1.67D-03	0.0	0.0	0.00015	0.00032
5B	MERL 71	1600.	0.00500	-1.00	1.67D-03	0.0	0.0	0.00011	0.00033
6A	MERL 76	1600.	0.00500	-1.00	1.67D-03	0.0	0.0	0.00011	0.00022
6B	MERL 76	1600.	0.00500	-1.00	1.67D-03	0.0	0.0	0.00013	0.00017
6C	MERL 75	1600.	0.00500	-1.00	1.67D-03	0.0	0.0	0.00015	0.00025
6D	MERL 75	1600.	0.00500	-1.00	1.67D-03	0.0	0.0	0.00010	0.00018
33B	MERL 76	1600.	0.00500	-1.00	1.67D-03	0.0	0.0	0.00012	0.00025
35B	MERL 76	1600.	0.00500	-1.00	1.67D-03	0.0	0.0	0.00010	0.00020
49A	MERL 75	1600.	0.00500	-1.00	1.67D-03	0.0	0.0	0.00010	0.00012
53C	MERL 75	1600.	0.00500	-1.00	1.67D-03	0.0	0.0	0.00018	0.00021
34A	MERL 76	1600.	0.00500	-1.00	1.67D-04	0.0	0.0	0.00020	0.00040
36A	MERL 76	1600.	0.00500	-1.00	1.67D-04	0.0	0.0	0.00028	0.00035
37D	MERL 76	1600.	0.00500	-1.00	1.67D-04	0.0	0.0	0.00026	0.00033
15D	MERL 75	1600.	0.00509	-1.00	8.48D-05	0.0	0.0	0.00038	0.00067
30C	MERL 75	1600.	0.00500	-1.00	8.33D-05	0.0	0.0	0.00028	0.00062
51A	MERL 75	1600.	0.00506	-1.00	8.40D-05	0.0	0.0	0.00036	0.00059
34C	MERL 76	1600.	0.00350	-1.00	1.67D-03	0.0	0.0	0.00005	0.00007
33D	MERL 76	1600.	0.00400	-1.00	1.67D-03	0.0	0.0	0.00010	0.00009
36C	MERL 76	1600.	0.00400	-1.00	1.67D-03	0.0	0.0	0.00008	0.00010
52A	MERL 75	1600.	0.00400	-1.00	1.67D-03	0.0	0.0	0.00005	0.00006
34B	MERL 76	1600.	0.00800	-1.00	1.67D-03	0.0	0.0	0.00100	0.00130
35A	MERL 76	1600.	0.00800	-1.00	1.67D-03	0.0	0.0	0.00097	0.00103
35C	MERL 76	1600.	0.00800	-1.00	1.67D-03	0.0	0.0	0.00090	0.00100
37A	MERL 76	1600.	0.00800	-1.00	1.67D-03	0.0	0.0	0.00105	0.00129
17B	MERL 75	1600.	0.00800	-1.00	1.67D-04	0.0	0.0	0.00143	0.00140
31B	MERL 75	1600.	0.00803	-0.99	1.67D-04	0.0	0.0	0.00162	0.00166
48C	MERL 75	1600.	0.00800	-1.00	1.67D-04	0.0	0.0	0.00134	0.00150
50D	MERL 75	1600.	0.00800	-1.00	1.67D-04	0.0	0.0	0.00132	0.00147

871°C (1600°F) BASELINE SPECIMEN TEST - LIST 2

COLUMN HEADING - DESCRIPTION
SPEC - SPEC ID
SEPR - FAILURE (CYCLES)
DR5: - 5% LOAD DROP
MSO: - AVG STRESS 0 PSI
DLSO - DEL STRESS0 PSI

COLUMN HEADING - DESCRIPTION
FREQ - FREQUENCY (CPM)
CRAK - INITIAL CRACK
DR10 - 10% LOAD DROP
MSHF - AVG STRESS 1/2 psi
DLSH - DEL STRESS 1/2 psi

SPEC	FREQ	SEPR	CRAK	DR5:	DR10	MSO:	MSHF	DLSO	DLSH
1B	9.996	4089.	1554.	2700.	3300.	-353.	0.	109618.	105516.
3B	9.996	2125.	808.	2000.	2100.	-707.	707.	109618.	108910.
4B	9.996	3226.	1226.	2900.	3050.	-714.	0.	120086.	112223.
5B	9.996	3308.	1257.	2550.	3000.	-2225.	0.	114243.	111573.
6A	9.996	3793.	1441.	2500.	3500.	-356.	-356.	110398.	105270.
6B	9.996	2716.	1032.	2600.	2700.	-702.	1755.	108146.	106039.
6C	9.996	3659.	1466.	3200.	3600.	636.	1060.	107355.	105375.
6D	9.996	2965.	1127.	2800.	2900.	0.	-356.	113960.	110399.
33B	9.996	2400.	912.	2150.	2240.	-1793.	0.	112625.	111765.
35B	9.996	4000.	1520.	3300.	3780.	-712.	0.	112535.	109402.
49A	9.996	3519.	1337.	3380.	3420.	1435.	17216.	110473.	110473.
53C	9.996	2975.	1131.	2343.	2488.	-852.	2415.	120739.	119744.
34A	0.996	2756.	923.	2347.	2656.	-285.	-1959.	107123.	102208.
36A	0.996	2470.	827.	1707.	2110.	1151.	1655.	105324.	101439.
37D	0.996	3041.	1019.	2219.	2968.	783.	-712.	98433.	98006.
15D	0.498	2260.	757.	1991.	2120.	-1670.	-1419.	102626.	93683.
30C	0.500	2350.	787.	2000.	2160.	-1344.	-990.	96322.	91372.
51A	0.498	1489.	499.	1220.	1310.	341.	700.	96788.	90734.
34C	13.998	68000.	21760.	67322.	67580.	-574.	-717.	73458.	76040.
33D	12.498	11102.	3553.	0.	0.	139.	-1179.	94036.	93897.
36C	12.498	9964.	3188.	8802.	9252.	-142.	-855.	90313.	91311.
52A	12.498	11409.	3651.	6690.	8100.	1425.	1425.	98291.	98291.
34B	6.246	440.	81.	278.	383.	-1435.	0.	162123.	144907.
35A	6.246	475.	88.	459.	468.	-1068.	-570.	152564.	149287.
35C	6.246	500.	93.	410.	454.	-2152.	0.	150645.	146915.
37A	6.246	375.	69.	300.	330.	-1578.	-1585.	152367.	146500.
17B	0.624	376.	64.	255.	325.	2564.	3989.	150712.	147863.
31B	0.625	291.	49.	261.	272.	817.	-756.	135752.	133991.
48C	0.624	229.	39.	199.	208.	2137.	427.	147436.	142877.
50D	0.624	208.	35.	184.	189.	997.	0.	143447.	139601.

871°C (1600°F) R-RATIO EFFECTS - LIST 1

COLUMN HEADING - DESCRIPTION
SPEC - SPEC ID
TEMP - TEMP.(DEG. F)
RE:: - RE (EMIN/EMAX)
DWLT - DWELL T (SEC)
DEPO - PSTRAIN RANGE 0

COLUMN HEADING - DESCRIPTION
TYPE - MAT. TYPE
DELE - DEL STRAIN IN/IN
ERAT - DEL STRAIN RATE
DWLC - DWELL C (SEC)
DEPH - PSTRAIN RANGE1/2

SPEC	TYPE	TEMP	DELE	RE::	ERAT	DWLT	DWLC	DEPO	DEPH
14A	MERL 75	1600.	0.00496	0.01	1.65D-03	0.0	0.0	0.00017	0.00019
14C	MERL 75	1600.	0.00493	0.01	1.64D-03	0.0	0.0	0.00036	0.00024
21D	MERL 75	1600.	0.00497	0.00	1.66D-03	0.0	0.0	0.00043	0.00027
22D	MERL 75	1600.	0.00497	0.00	1.66D-03	0.0	0.0	0.00032	0.00020
23B	MERL 75	1600.	0.00496	0.00	1.65D-03	0.0	0.0	0.00038	0.00023
25B	MERL 75	1600.	0.00493	0.01	1.64D-03	0.0	0.0	0.00039	0.00025
32C	MERL 75	1600.	0.00497	0.00	1.66D-03	0.0	0.0	0.00036	0.00022
21A	MERL 75	1600.	0.00503	-0.00	8.38D-05	0.0	0.0	0.00065	0.00057
26A	MERL 75	1600.	0.00505	0.00	8.42D-05	0.0	0.0	0.00070	0.00058
23A	MERL 75	1600.	0.00490	0.33	1.61D-03	0.0	0.0	0.00044	0.00015
24A	MERL 75	1600.	0.00494	0.34	1.65D-03	0.0	0.0	0.00042	0.00023
25C	MERL 75	1600.	0.00525	0.31	1.75D-03	0.0	0.0	0.00043	0.00031
26C	MERL 75	1600.	0.00491	0.34	1.64D-03	0.0	0.0	0.00043	0.00023
27A	MERL 75	1600.	0.00495	0.34	1.65D-03	0.0	0.0	0.00044	0.00023
23D	MERL 75	1600.	0.00492	-153.73	1.64D-03	0.0	0.0	0.00030	0.00028
25D	MERL 75	1600.	0.00494	-151.26	1.65D-03	0.0	0.0	0.00031	0.00024
27D	MERL 75	1600.	0.00495	-219.02	1.65D-03	0.0	0.0	0.00030	0.00023
28A	MERL 75	1600.	0.00492	-88.02	1.64D-03	0.0	0.0	0.00030	0.00026

871°C (1600°F) R-RATIO EFFECTS - LIST 2

COLUMN HEADING - DESCRIPTION
SPEC - SPEC ID
SEPR - FAILURE (CYCLES)
DR5: - 5% LOAD DROP
MSO: - AVG STRESS 0 PSI
DLSO - DEL STRESS0 PSI

COLUMN HEADING - DESCRIPTION
FREQ - FREQUENCY (CPM)
CRAK - INITIAL CRACK
DR10 - 10% LOAD DROP
MSHF - AVG STRESS 1/2
DLSH - DEL STRESS1/2

SPEC	FREQ	SEPR	CRAK	DR5:	DR10	MSO:	MSHF	DLSO	DLSH
14A	9.999	3500.	1558.	3309.	3359.	41328.	25523.	100392.	96998.
14C	10.000	3055.	1359.	2896.	2941.	31578.	20914.	101938.	102634.
21D	10.000	1750.	779.	1678.	1698.	29702.	21517.	98660.	100330.
22D	9.999	3610.	1606.	3518.	3533.	32566.	23422.	96993.	96458.
23B	10.000	4618.	2055.	4414.	4500.	30450.	20520.	97793.	99445.
25B	10.000	3200.	1424.	3110.	3142.	30615.	26156.	98794.	98237.
32C	10.000	5558.	2473.	5293.	5347.	35505.	23396.	92509.	93201.
21A	0.500	1236.	414.	1130.	1234.	22078.	4379.	98130.	95918.
26A	0.500	1813.	607.	1700.	1752.	21358.	3835.	92971.	90935.
23A	10.000	2757.	1172.	2510.	2740.	50698.	26238.	100284.	100566.
24A	9.997	3090.	1313.	3032.	3056.	42148.	21906.	103787.	103951.
25C	10.000	1715.	729.	1674.	1686.	41729.	24298.	105889.	109251.
26C	9.998	2446.	1040.	2389.	2410.	42409.	24336.	102689.	104069.
27A	10.001	3504.	1489.	3318.	3392.	42417.	27496.	95660.	96710.
23D	10.000	6155.	2770.	5841.	5914.	-25713.	-14822.	102707.	105896.
25D	10.000	4828.	2173.	3976.	4316.	-23404.	-14197.	102250.	104422.
27D	10.000	9700.	4365.	8991.	9304.	-24514.	-14761.	97614.	98832.
28A	10.000	6160.	2772.	5054.	5629.	-20360.	1048.	98401.	96946.

871°C (1600°F) DWELL TESTS - LIST 1

COLUMN HEADING	- DESCRIPTION
SPEC	- SPEC ID
TEMP	- TEMP.(DEG. F)
RE::	- RE (EMIN/EMAX)
DWLT	- DWELL T (SEC)
DEPO	- PSTRAIN RANGE 0

COLUMN HEADING	- DESCRIPTION
TYPE	- MAT. TYPE
DELE	- DEL STRAIN IN/IN
ERAT	- DEL STRAIN RATE
DWLC	- DWELL C (SEC)
DEPH	- PSTRAIN RANGE1/2

SPEC	TYPE	TEMP	DELE	RE::	ERAT	DWLT	DWLC	DEPO	DEPH	Δσi	(psi) Δσ1/2
14B	MERL 75	1600.	0.00499	-0.99	1.51D-04	60.0	0.0	0.00034	0.00054	8500	5700
15A	MERL 75	1600.	0.00500	-1.00	1.51D-04	60.0	0.0	0.00033	0.00052	5700	5700
22C	MERL 75	1600.	0.00498	-0.99	1.51D-04	60.0	0.0	0.00068	0.00063	12900	7100
12D	MERL 75	1600.	0.00506	-0.98	1.53D-04	0.0	60.0	0.0	0.00067	5000	5700
27B	MERL 75	1600.	0.00503	-0.99	1.52D-04	0.0	60.0	0.00025	0.00065	1400	5700
27C	MERL 75	1600.	0.00504	-0.99	1.53D-04	0.0	60.0	0.00049	0.00068	4300	5700
49D	MERL 75	1600.	0.00500	-1.00	1.51D-04	0.0	60.0	0.00029	0.00043	2850	5000
52B	MERL 75	1600.	0.00500	-1.00	1.51D-04	0.0	60.0	0.00059	0.00045	3600	5000
53D	MERL 75	1600.	0.00500	-1.00	1.51D-04	0.0	60.0	0.00027	0.00032	2350	3600
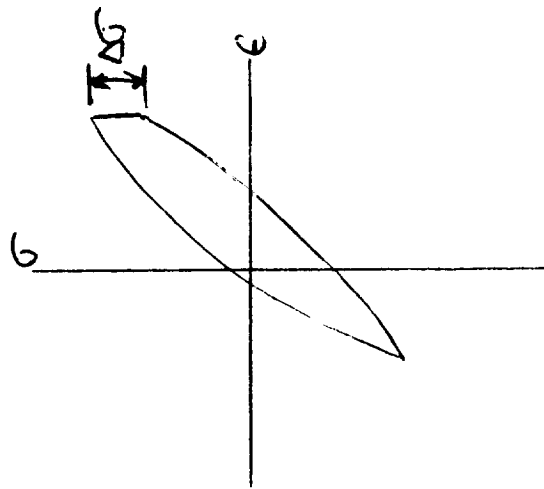
871°C (1600°F) DWELL TESTS - LIST 2

COLUMN HEADING - DESCRIPTION
SPEC - SPEC ID
SEPR - FAILURE (CYCLES)
DR5: - 5% LOAD DROP
MSO: - AVG STRESS 0 PSI
DLSO - DEL STRESS0 PSI

COLUMN HEADING - DESCRIPTION
FREQ - FREQUENCY (CPM)
CRAK - INITIAL CRACK
DR10 - 10% LOAD DROP
MSHF - AVG STRESS 1/2
DLSH - DEL STRESS1/2

SPEC	FREQ	SEPR	CRAK	DR5:	DR10	MSO:	MSHF	DLSO	DLSH
14B	0.909	6113.	2048.	5659.	5911.	1414.	-13976.	101839.	97635.
15A	0.909	2280.	764.	2130.	2260.	-1420.	-11790.	109660.	105966.
22C	0.909	3871.	1297.	0.	0.	-1602.	-13276.	105917.	103186.
12D	0.909	840.	185.	818.	824.	0.	10091.	0.	103789.
27B	0.909	1055.	285.	960.	1110.	3406.	11531.	102298.	98239.
27C	0.909	830.	224.	803.	812.	4793.	12042.	101421.	97576.
49D	0.909	1625.	439.	1440.	1545.	2030.	13034.	101353.	99573.
52B	0.909	1265.	342.	1165.	1197.	2556.	16051.	102841.	100000.
53D	0.909	2320.	626.	1880.	2007.	2066.	14031.	95869.	94444.

538°C (1000°F) SPECIMEN TESTS - LIST 1

COLUMN HEADING	-	DESCRIPTION
SPEC	-	SPEC ID
TEMP	-	TEMP.(DEG. F)
RE::	-	RE (EMIN/EMAX)
DWLT	-	DWELL T (SEC)
DEPO	-	PSTRAIN RANGE 0

COLUMN HEADING	-	DESCRIPTION
TYPE	-	MAT. TYPE
DELE	-	DEL STRAIN IN/IN
ERAT	-	DEL STRAIN RATE
DWLC	-	DWELL C (SEC)
DEPH	-	PSTRAIN RANGE1/2

SPEC	TYPE	TEMP	DELE	RE::	ERAT	DWLT	DWLC	DEPO	DEPH
1C	MERL 71	1000.	0.00500	-1.00	1.67D-03	0.0	0.0	0.00002	0.00002
3A	MERL 76	1000.	0.00500	-1.00	1.67D-03	0.0	0.0	0.00003	0.00003
3C	MERL 76	1000.	0.00500	-1.00	1.67D-03	0.0	0.0	0.00002	0.00002
3D	MERL 75	1000.	0.00500	-1.00	1.67D-03	0.0	0.0	0.00005	0.00005
4A	MERL 75	1000.	0.00500	-1.00	1.67D-03	0.0	0.0	0.00002	0.00002
4C	MERL 76	1000.	0.00500	-1.00	1.67D-03	0.0	0.0	0.00003	0.00003
4D	MERL 75	1000.	0.00500	-1.00	1.67D-03	0.0	0.0	0.00005	0.00005
5C	MERL 71	1000.	0.00500	-1.00	1.67D-03	0.0	0.0	0.00002	0.00002
17D	MERL 75	1000.	0.00493	-0.99	1.64D-03	0.0	0.0	0.00006	0.00008
33A	MERL 76	1000.	0.00500	-1.00	1.67D-03	0.0	0.0	0.00002	0.00002
33C	MERL 76	1000.	0.00500	-1.00	1.67D-03	0.0	0.0	0.00002	0.00002
22A	MERL 75	1000.	0.00473	0.02	1.61D-03	0.0	0.0	0.00004	0.00004
24B	MERL 75	1000.	0.00482	0.03	1.68D-03	0.0	0.0	0.00003	0.00001
24C	MERL 75	1000.	0.00497	0.01	1.69D-03	0.0	0.0	0.00002	0.00002
35D	MERL 76	1000.	0.00800	-1.00	1.67D-03	0.0	0.0	0.00058	0.00020
36B	MERL 76	1000.	0.00800	-1.00	1.67D-03	0.0	0.0	0.00058	0.00024
37B	MERL 76	1000.	0.00800	-1.00	1.67D-03	0.0	0.0	0.00046	0.00020
50B	MERL 75	1000.	0.00800	-1.00	1.60D-03	0.0	0.0	0.00034	0.00016
34D	MERL 76	1000.	0.01000	-1.00	1.67D-03	0.0	0.0	0.00164	0.00080
36D	MERL 76	1000.	0.01000	-1.00	1.67D-03	0.0	0.0	0.00184	0.00096
37C	MERL 76	1000.	0.01000	-1.00	1.67D-03	0.0	0.0	0.00224	0.00130
50A	MERL 75	1000.	0.00997	-0.98	1.66D-03	0.0	0.0	0.00223	0.00121

538°C (1000°F) SPECIMEN TESTS - LIST 2

COLUMN HEADING - DESCRIPTION
SPEC - SPEC ID
SEPR - FAILURE (CYCLES)
DR5: - 5% LOAD DROP
MS0: - AVG STRESS 0 PSI
DLS0 - DEL STRESS0 PSI

COLUMN HEADING - DESCRIPTION
FREQ - FREQUENCY (CPM)
CRAK - INITIAL CRACK
DR10 - 10% LOAD DROP
MSHF - AVG STRESS 1/2
DLSH - DEL STRESS1/2

SPEC	FREQ	SEPR	CRAK	DR5:	DR10	MS0:	MSHF	DLS0	DLSH
1C	9.996	7931.	5393.	0.	0.	-351.	125.	135610.	137015.
3A	9.996	7775.	5287.	0.	0.	-500.	2658.	130466.	131927.
3C	9.996	8877.	6036.	8133.	8560.	-1140.	-1425.	141595.	140313.
3D	10.000	13300.	9044.	12625.	13050.	-497.	1776.	125994.	124290.
4A	10.002	10650.	7242.	10300.	10520.	-929.	177.	125645.	126382.
4C	9.996	11400.	7752.	10630.	11020.	-1792.	1219.	135484.	137491.
4D	10.000	12560.	8541.	0.	0.	-354.	4059.	116690.	117043.
5C	9.996	8774.	5966.	7040.	7840.	-115.	169.	140621.	139986.
17D	10.000	10890.	7405.	0.	0.	481.	4673.	122546.	124940.
33A	9.996	7640.	5195.	5890.	6660.	-2226.	445.	137685.	135905.
33C	9.996	9050.	6154.	8934.	8986.	-1424.	-1994.	129630.	128775.
22A	10.002	7529.	5120.	7262.	7343.	47174.	46604.	107621.	112007.
24B	10.001	6792.	4619.	6750.	6789.	44117.	42107.	110485.	120202.
24C	9.993	6480.	4406.	6420.	6436.	38189.	40594.	123055.	123620.
35D	6.246	920.	556.	907.	0.	-507.	0.	198116.	205797.
36B	6.246	930.	562.	868.	875.	-712.	-1068.	200855.	208689.
37B	6.250	1550.	936.	1481.	1518.	-719.	-2086.	187050.	192662.
50B	6.000	1278.	772.	0.	0.	-1839.	1344.	185290.	197878.
34D	4.998	397.	222.	385.	390.	-712.	-2208.	206553.	223789.
36D	5.010	305.	171.	300.	0.	-698.	-2095.	210893.	233240.
37C	4.998	227.	127.	223.	0.	-2146.	-3934.	210300.	229614.
50A	5.000	238.	133.	0.	0.	-1220.	-1407.	214226.	233094.

649°C (1200°F) and 760°C (1400°F) SPECIMEN TEST - LIST 2

COLUMN HEADING - DESCRIPTION
SPEC - SPEC ID
TEMP - TEMP.(DEG. F)
RE:: - RE (EMIN/EMAX)
DWLT - DWELL T (SEC)
DEPO - PSTRAIN RANGE 0

COLUMN HEADING - DESCRIPTION
TYPE - MAT. TYPE
DELE - DEL STRAIN IN/IN
ERAT - DEL STRAIN RATE
DWLC - DWELL C (SEC)
DEPH - PSTRAIN RANGE1/2

SPEC	TYPE	TEMP	RE::	DELE	ERAT	DWLT	DWLC	DEPO	DEPH	Δσi (psi)	Δσ1/2
17C	MERL 75	1200.	-0.99	0.00791	2.64D-03	0.0	0.0	0.00046	0.00021		
32D	MERL 75	1400.	-1.00	0.00500	1.67D-03	0.0	0.0	0.00005	0.00004		
48B	MERL 75	1400.	-1.00	0.00500	1.67D-03	0.0	0.0	0.00004	0.00004		
51C	MERL 75	1400.	-1.00	0.00500	1.67D-03	0.0	0.0	0.00004	0.00005		
29D	MERL 75	1400.	-1.00	0.00800	1.67D-03	0.0	0.0	0.00030	0.00016		
31C	MERL 75	1400.	-1.00	0.00800	1.67D-03	0.0	0.0	0.00033	0.00023		
50C	MERL 75	1400.	-1.00	0.00800	1.60D-03	0.0	0.0	0.00023	0.00014		
15B	MERL 75	1400.	-1.01	0.00499	1.51D-04	0.0	60.0	0.00016	0.00016	700	700
32B	MERL 75	1400.	-1.00	0.00500	1.52D-04	0.0	60.0	0.00007	0.00008	700	700

649°C (1200°F) and 760°C (1400°F) SPECIMEN TEST - LIST 1

COLUMN HEADING - DESCRIPTION
SPEC - SPEC ID
SEPR - FAILURE (CYCLES)
DR5: - 5% LOAD DROP
MSO: - AVG STRESS 0 PSI
DLSO - DEL STRESS0 PSI

COLUMN HEADING - DESCRIPTION
FREQ - FREQUENCY (CPM)
CRAK - INITIAL CRACK
DR10 - 10% LOAD DROP
MSHF - AVG STRESS 1/2
DLSH - DEL STRESS1/2

SPEC	FREQ	SEPR	CRAK	DR5:	DR10	MSO:	MSHF	DLSO	DLSH
17C	10.000	931.	418.	876.	916.	888.	1811.	188280.	190206.
32D	9.996	7816.	3283.	7515.	7539.	0.	9972.	128205.	123932.
48B	9.996	6931.	2911.	6730.	6756.	-2849.	-2422.	128205.	129202.
51C	9.996	8990.	3776.	8850.	8864.	284.	852.	120455.	119886.
29D	6.240	784.	231.	672.	723.	-1709.	427.	177778.	178490.
31C	6.240	942.	278.	858.	910.	15670.	7123.	172365.	166667.
50C	6.000	1075.	317.	908.	958.	-356.	-499.	175926.	175641.
15B	0.909	11634.	4654.	11184.	11339.	232.	5467.	109954.	108676.
32B	0.909	5621.	2248.	5600.	5620.	712.	13300.	110000.	111000.

932°C (1800°F) SPECIMEN TESTS - LIST 1

COLUMN HEADING - DESCRIPTION
    SPEC - SPEC ID
    TEMP - TEMP.(DEG. F)
    RE:: - RE (EMIN/EMAX)
    DWLT - DWELL T (SEC)
    DEPO - PSTRAIN RANGE 0

COLUMN HEADING - DESCRIPTION
    TYPE - MAT. TYPE
    DELE - DEL STRAIN IN/IN
    ERAT - DEL STRAIN RATE
    DWLC - DWELL C (SEC)
    DEPH - PSTRAIN RANGE1/2

SPEC	TYPE	TEMP	RE::	DELE	ERAT	DWLT	DWLC	DEPO	DEPH
14D	MERL 75	1800.	-1.00	0.00500	1.67D-03	0.0	0.0	0.00112	0.00117
32A	MERL 75	1800.	-1.00	0.00496	1.65D-03	0.0	0.0	0.00084	0.00094
53A	MERL 75	1800.	-1.01	0.00514	1.71D-03	0.0	0.0	0.00093	0.00088
53B	MERL 75	1800.	-1.00	0.00500	1.67D-03	0.0	0.0	0.00119	0.00092
29A	MERL 75	1800.	-0.97	0.00506	1.69D-04	0.0	0.0	0.00132	0.00143
30B	MERL 75	1800.	-0.97	0.00501	1.67D-04	0.0	0.0	0.00140	0.00140
48A	MERL 75	1800.	-0.98	0.00505	1.68D-04	0.0	0.0	0.00132	0.00142
15C	MERL 75	1800.	-1.00	0.00800	1.67D-03	0.0	0.0	0.00258	0.00275
16B	MERL 75	1800.	-1.00	0.00800	1.67D-03	0.0	0.0	0.00253	0.00263
16C	MERL 75	1800.	-0.98	0.00814	1.68D-03	0.0	0.0	0.00265	0.00283
29B	MERL 75	1800.	-1.01	0.00804	1.68D-04	0.0	0.0	0.00310	0.00311

932°C (1800°F) SPECIMEN TESTS - LIST 2

COLUMN HEADING - DESCRIPTION
    SPEC - SPEC ID
    SEPR - FAILURE (CYCLES)
    DR5: - 5% LOAD DROP
    MSO: - AVG STRESS 0 PSI
    DLSO - DEL STRESS0 PSI

COLUMN HEADING - DESCRIPTION
    FREQ - FREQUENCY (CPM)
    CRAK - INITIAL CRACK
    DR10 - 10% LOAD DROP
    MSHF - AVG STRESS 1/2
    DLSH - DEL STRESS1/2

SPEC	FREQ	SEPR	CRAK	DR5:	DR10	MSO:	MSHF	DLSO	DLSH
14D	10.020	1450.	406.	1065.	1254.	0.	-427.	79772.	77920.
32A	10.000	1644.	460.	1365.	1478.	1447.	733.	76723.	77806.
53A	9.972	1100.	308.	560.	665.	-5120.	-1289.	84127.	76147.
53B	9.996	1390.	389.	1150.	1207.	2422.	-1567.	71652.	78490.
29A	0.999	1205.	337.	828.	978.	-192.	-550.	67208.	65159.
30B	0.999	1160.	325.	843.	911.	157.	394.	71950.	72804.
48A	0.999	1366.	382.	1229.	1332.	-562.	204.	68704.	66345.
15C	6.240	334.	67.	237.	293.	-712.	-2137.	99003.	96154.
16B	6.240	241.	48.	211.	233.	712.	-570.	97578.	92296.
16C	10.020	255.	51.	208.	241.	1154.	-720.	99209.	94160.
29B	0.625	218.	44.	204.	207.	18.	260.	85937.	84693.

APPENDIX II
EFFECT OF UNREVERSED INELASTIC STRAIN ON NET CYCLIC CAPABILITY

The cyclic damage accumulation model of Equation 39 is referenced to fully reversed, fast strain rate data (R=-1, $\dot{\epsilon}$ = .001667 in./in./sec) which effectively accounts for the cyclic fatigue damage process. Alternate mean strains (R$\neq$-1), produce large, relative to the cyclic inelastic strain, nonreversed inelastic strains during the initial loading, as shown in Figure II-1. It was assumed that this nonreversed inelastic strain should be deducted from the initial material cyclic capability value.

As defined, ϵ_{in} is a measure of the unreversed inelastic strain. At lower temperatures where time dependent deformation (creep) is not active, the inelastic strain is considered to occur exclusively within the grains. At elevated temperatures, the observed inelastic strain is considered a mixture of grain and grain boundary deformation and should be partitioned to determine the portion affecting the grain capability. In the initial evaluation, the partitioning was based on the ratio of primary and secondary creep rates. From creep data, the grain component(primary creep) is represented as:

$$\epsilon_p = A\sigma^B t^C$$
$$\text{where } C = D^E$$

(II-1)

and the grain boundary component (secondary creep) is:

$$\epsilon_s = A'\sigma^{B'} t$$

(II-2)

Now, assume ϵ_{in} of Fig II-1 can be represented by primary and secondary creep strains,

$$\epsilon_{in} = \epsilon_p + \epsilon_s$$

(II-3)

and from Equations II-1 and II-2
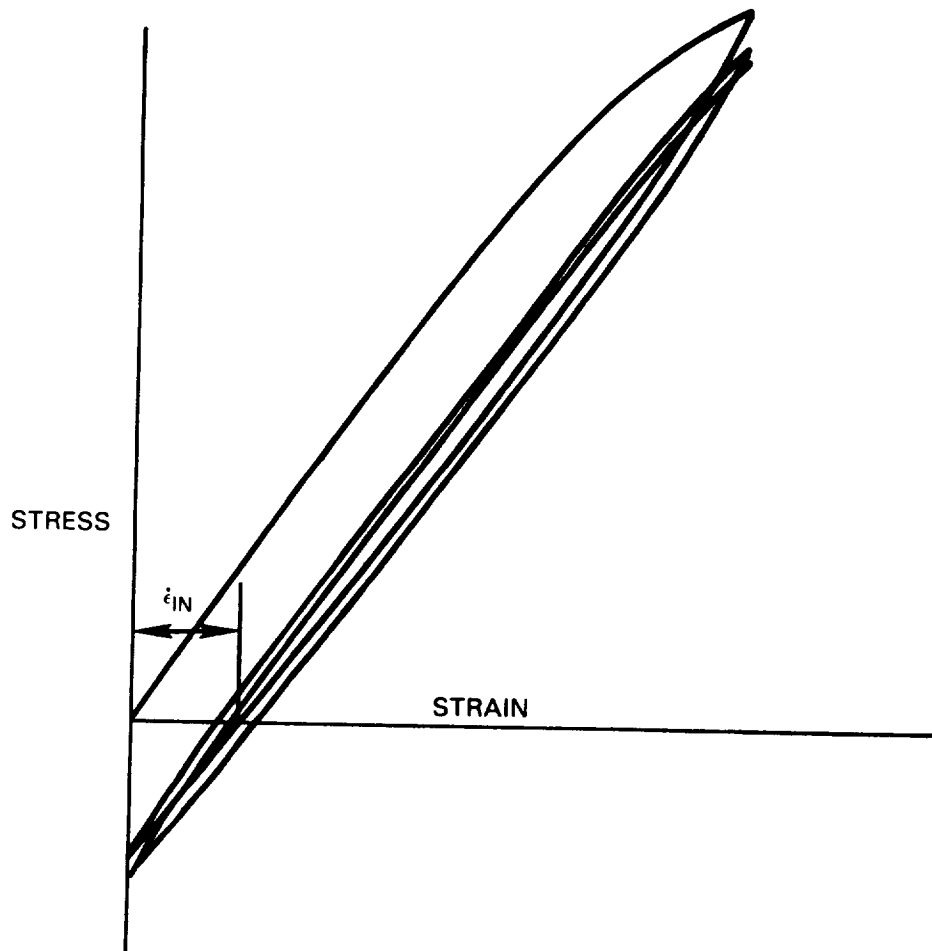
Figure II-1 Unreversed Inelastic Strain for Non-Zero Mean Strain Cycle

$$\epsilon_p \Big/ \epsilon_s = \frac{A\,\sigma^B\,t^{D\sigma^E}}{A'\,\sigma^{B'}\,t} \qquad\qquad\qquad\text{(II-4)}$$

or

$$\epsilon_p \Big/ \epsilon_s = \frac{A}{A'}\,\sigma^{(B-B')}\,t^{(D\sigma^E-1)} \qquad\qquad\text{(II-5)}$$

where $\sigma = \sigma_{MAX}$ of the first cycle

t = loading time + strain hold times which increase ϵ_{in}

Now let $X = \epsilon_p/\epsilon_s$ \qquad\qquad\qquad (II-6)

then $\epsilon_{in} = \epsilon_p + \epsilon_p \left(\dfrac{1}{x}\right)$

or $\epsilon_p = \epsilon_{in} \left(\dfrac{x}{x+1}\right)$ \qquad\qquad\qquad (II-7)

The primary creep strain can then be subtracted from the total grain capability ($\overline{\epsilon}_p$) to estimate a net cyclic capability for calculation of the initiation life.

For tests run at $R\epsilon = 1/3$ (.25% to .75%) or $-\infty$ (-.50% to 0), certain limitations of the experimental setup resulted in stress relaxation during the initial quarter cycle loading. This is seen in Figure II-2 for a $R\epsilon = 1/3$ test in which the relaxation occurs at a strain of 0.25%. For the $R\epsilon = -$ test (Figure II-3), the relaxation is integrated throughout the initial loading. The additional unreversed inelastic strain produced in these cycles was also considered as a debit to the grain cyclic capability and was therefore included in the determination of the net value prior to the calculation of the initiation life.
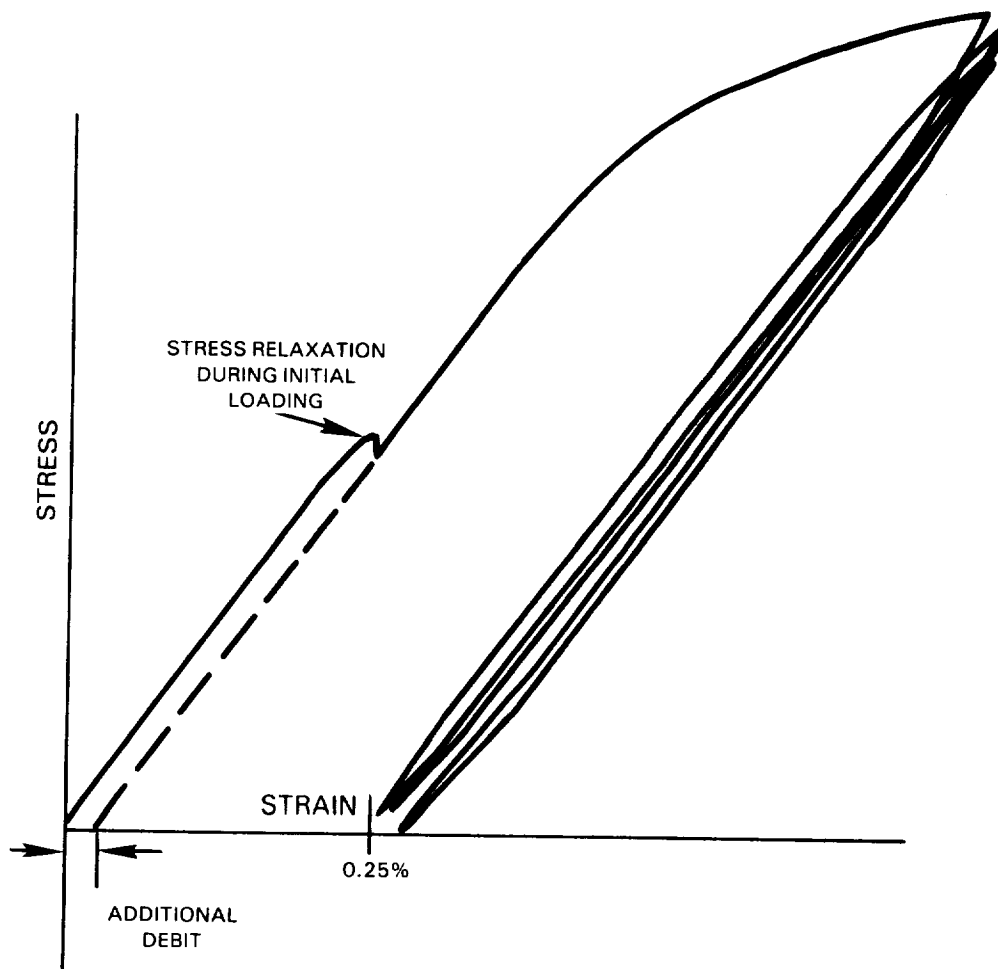
Figure II-2 Additional Inelastic Strain Produced in R = 1/3 Cycle
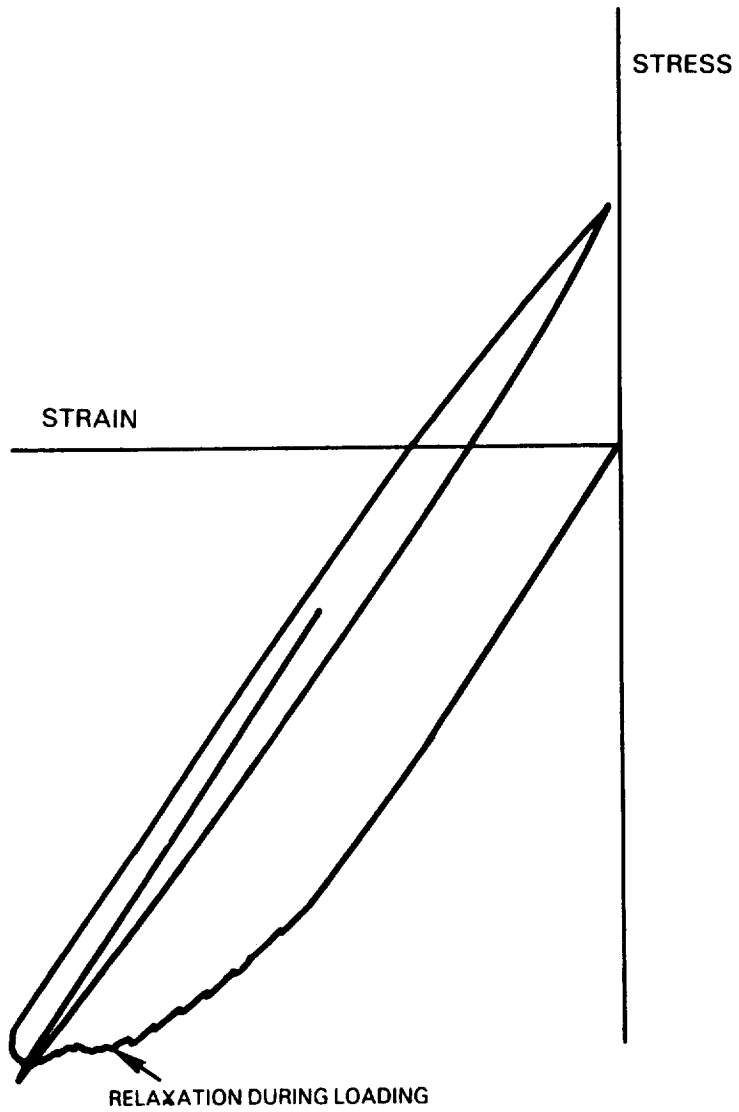
Figure II-3 Observed Relaxation During Loading of Rє = -∞

ALTERNATE FORMS OF THE MODEL

The complete creep fatigue equation proposed in section 3.3.3 is:

$$\bar{\epsilon}_p - \int_0^N \frac{dD}{dN}\Big]_{Ref} \left\{ \left(\frac{\sigma T}{\sigma T_R}\right)\left(\frac{\Delta\sigma}{\Delta\sigma_R}\right) + \left[\left(\frac{\Delta\sigma R}{\Delta\sigma}\right)\left(\frac{\sigma T}{\sigma T_R}\right)\right]^{B'} \times \left[\left(\frac{t}{t_R}\right)^{C'} - 1\right] \right\} dN = 0$$

(III-1)

This represents an approach based on a knowledge of the strain range and the local stress response and is considered a creep-fatigue interaction model. By considering two special cases, it can be seen that the model "brackets" generally accepted life approaches for both low and high temperature. For example, by considering only time independent fatigue and assuming that the stress response does not change throughout the cycling, the life equation can be written as:

$$C = a \ (\Delta\epsilon)^b \left(\frac{\sigma T \Delta\sigma}{\sigma T_{Ref} \Delta\sigma_{Ref}}\right) N$$

(III-2)

where: $C = \bar{\epsilon}_p$ represents a constant grain capability

$$\frac{dD}{dN}\Big]_{Ref} = a(\Delta\epsilon)^b$$

$\Delta\epsilon$ = total or inelastic strain range

a, b = regression constants

This form is similar to life models proposed for low temperature (time a wave shape independent) fatigue e.g. Coffin-Manson. The term containing the stress ratio can be considered as a mean stress correction.

For cycles in which time dependent damage dominants (slow, high temperature tests), a limiting value of the equation can be determined assuming:

1.   time independent damage is neglible.

2.   the stress ratio in the time dependent term is approximately 1.

3. the cycle time is $\gg$ the reference time.

With this assumptions equation III-1 can be written as:

$$C = \int a \, (\Delta\sigma)^b \left(\frac{t}{tRef}\right)^c \, dN \qquad\qquad (III-3)$$

where: $\Delta\sigma = E \Delta\epsilon$

t = loading time fo reference cycle

t_{Ref} = loading time of reference cycle

In this form, the equation appears as an integration of power law creep damage which has been shown to be an accurate life prediction method for very high temperature tests. Thus, equation III-1 represents a transition between low temperature time independent fatigue and high temperature creep dominated processes.

One of the stated desirable features of a reliable modeling procedure is to distinguish between transgranular and intergranular crack initiation modes. The bulk of development and evaluation was performed on the transgranular model since most of the test specimens failed transgranularly. However, transition towards intergranular initiation was observed at 932°C (1800°F) for slow cyclic rates.

Preliminarily, two intergranular models were considered. The first model is similar to the transgranular model given in Equation 39, except that all terms and constants are related to secondary creep which was considered to represent the grain boundary damaging process. This is referred to as method 1.

$$\bar{\epsilon}_S - \int \frac{dD}{dN}\bigg|_{Ref} \left\{ \left(\frac{\sigma T}{\sigma T Ref} \cdot \frac{\Delta\sigma}{\Delta\sigma Ref}\right) + \left(\frac{\sigma T}{\sigma T Ref} \times \frac{\Delta\sigma_{REF}}{\Delta\sigma}\right)^{B'} \left[\left(\frac{t}{t_{Ref}}\right)^{C'} - 1\right] \right\} \, dN = 0 \quad (IV-1)$$

where: $\bar{\epsilon}_S$ ≡ secondary creep strain ductility as shown in Figure IV-1

$\dfrac{dD}{dN}\bigg]_{Ref}$ ≡ reference cyclic damage rate

σ_T ≡ maximum tensile stress

$\Delta\sigma$ ≡ stress amplitude

t ≡ time
$t = 1/2$ (Ramp Time) + tensile hold

N ≡ cycle number

134

Ref $\equiv$ reference condition

B' $\equiv$ exponent on stress in secondary creep power law

C' $\equiv$ exponent on time in secondary creep power law

The second model considered was simply a secondary creep power law ductility exhaustion model. This is referred to as method 2.

$$\bar{\epsilon}_s - \int A\sigma_T^B \; t \; dN = 0$$

where

$\bar{\epsilon}_s \equiv$ secondary creep strain ductility

$\sigma_T \equiv$ maximum tensile stress

$t \equiv$ time
$\quad t = 1/2$ (Ramp Time) + tensile hold

A, B $\equiv$ coefficients of $\dot{\epsilon}_s = A\sigma^B$ (assuming linear secondary creep strain rate.)

N $\equiv$ cycle number

Application of these two approaches to fatigue cycles in which intergranular initiation was observed has shown the ability to predict the current trend in the failure mode, although the exhaustion of creep ductility (method 2) appears to give more accurate predictions at this point. These results are summarized in Figure IV-1 where the predicted ductility (cycle capability) exhaustion for four different cycles are presented. In each figure, the cyclic capability vs fatigue cycles are predicted using the grain (transgrannular) model (equation 39) and the two intergranular models. In Figure IV-1 (A and B) the predicted exhaustion for two 871°C (1600°F) tests are presented. Both tests were at a strain range of 0.5%, however, the second test (IV-1 B) was run at a strain rate one half of the first test. Examination of the fracture surfaces of the specimens indicated a greater tendency toward intergranular initiation at the slower rate. The predictions for both cycles show that the grain capability is exhausted before the grain boundary capability, however, the rate of exhaustion for the slower cycle indicated that a further reduction in strain rate would have resulted in a predicted intergranular initiation. The second observation on these two cycles is that method 1 (grain boundary form of CDA damage equation) is exhausting the available ductility at a faster rate than in the second method. This may have some physical significance as the second method would seem to be more appropriate at temperatures dominated by creep damage processes. This is seen in Figure IV-1 (C and D) for two 932°C (1800°F) cycles run at the same strain rate but for two different strain ranges. In IV-1C transgranular initiation is predicted but the capability of the grain boundary is being exhausted at a rapid rate by the second method. Examination indicated this test to produce transgranular initiation. At a larger strain range (Figure IV-D), intergranular initiation was predicted consistent with the observed failure mode. The linear creep exhaustion model (method 2) appears to be more representative of the failure process at these conditions, than the creep fatigue interaction equation represented by method 1.

Further testing and model evaluations are required before any final conclusions are drawn, but both methods may be useful in distinguishing failure mode for various fatigue cycles.
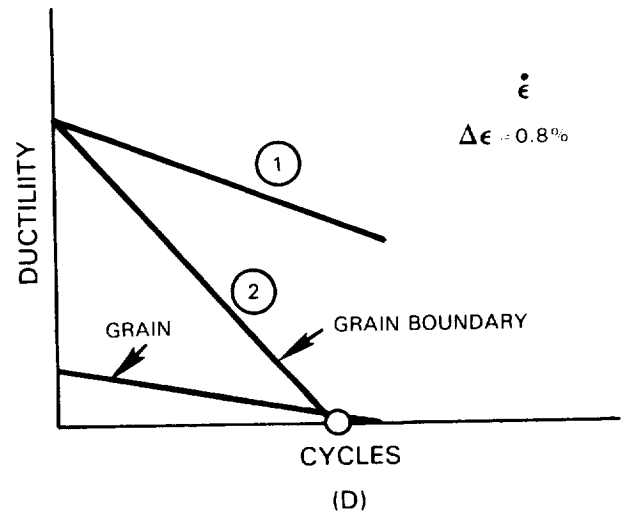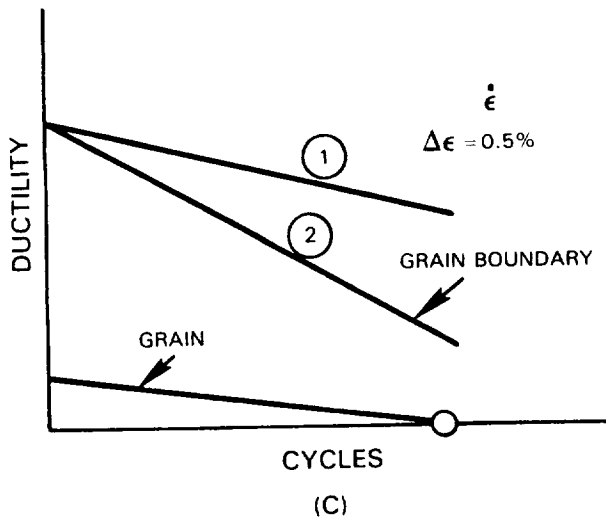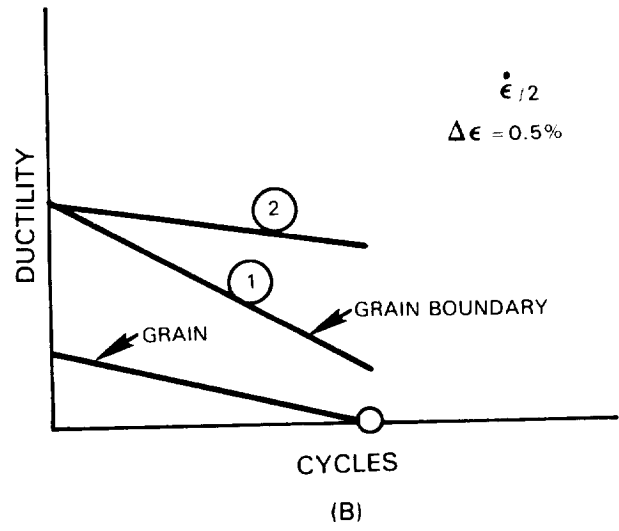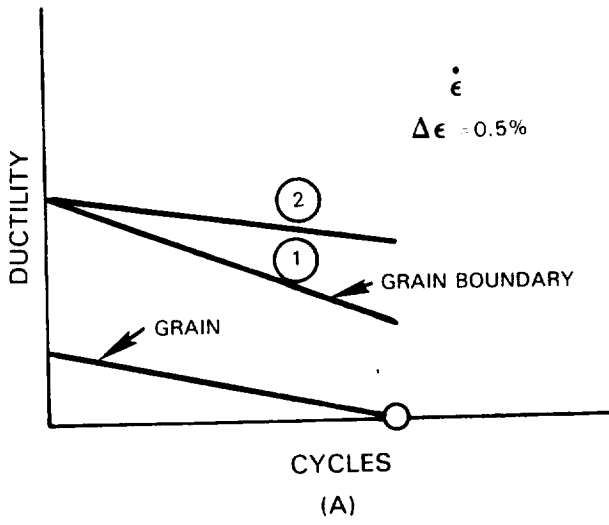
Figure IV-1 Exhaustion of Grain and Grain Boundary Ductilities

DISTRIBUTION LIST

Aerojet Liquid Rocket
Attn: V. Frick
Mgr, Matl's Eng
Box 13222
Sacramento, CA 95813

AFOSR/NA
Attn: Maj. David Glasgow
Mgr, Aerospace Sci
Bolling AFB
Washington, DC 20332

Wright Patterson Air Force Base
Attn: Ted Nicholas
AFWAL/MLLN
Wright Patterson
Air Force Base, OH   45433

Wright Patterson Air Force Base
Attn: Library
AFWAL/MLLAM
Wright Patterson
 Air Force Base, OH   45433

AiReasearch Mfg Co.
Attn: Richard Graves
2525 W. 190th St.
Torrance, CA 90509

Univ. of Alabama
Attn: Dr. A. E. Carden
AME Dept.
Box 2908
University, AL 35486

Allison Gas Turbine Oper.
Attn: Mehmet Doner   W8
P. O. Box 420
Indianapolis, IN 46206

Allison Gas Turbine Oper.
Attn: Frank Walters
P. O. Box 894
Indianopolis, IN 46206
Allison Gas Turbine Oper.
Attn: Donald Vaccari T10
P. O. Box 420
Indianopolis, IN 46206

Univ. of Arizona
Attn: Dr. Paul H. Wirsching
Dept Aero & Mech Eng.
Tucson, AZ 85721

Army Applied Tech Lab
Attn: Jan Lane
DAVDL-ATL-ATP
Fort Eustis VA 23604

Army Applied Tech Lab
Attn: Library
Fort Eustis, VA 23604

AVCO - Space Systems Div.
Attn: Library
Lowell Industrial Pk.
Lowell, MA 01851

AVCO - Lycoming Div.
Attn: Jerry Walters
550 S. Main St.
Stratford, CT 06497

Battelle Columbus Lab
Attn: Brian Leis
505 King Ave. +
Columbus, OH 43201

Boeing
Attn: Library
3801 S. Oliver
Wichita, KS 67210

Case Western Reserve Univ.
Attn: Prof. S. S. Manson
619 Glennan Bldg.
10900 Euclid Ave.
Cleveland, OH 44106

Univ. of Cincinnati
Attn: Dr. Donald Stouffer
Rm. 833 Rhodes Hall
Dept. Eng. Sci.
Cincinnati, OH 45221

Univ. of Connecticut
Attn: Dr. Eric Jordan
Mech. Eng. Dept. U-139
Storrs, CT 06268

Curtiss Wright
Attn: Jerome Mogul
Dir - Matl's Eng.
1 Rotary Dr.
Wood-Ridge, NJ 07075

Univ. of Dayton
Attn: Dr. Joseph Gallagher
Research Institute
Rm. 563 Kettering Bldg.
Dayton, OH 45469

Defense Documentation Ctr.
Cameron Station
5010 Duke St.
Alexandria, VA 22314

DeLaval Turbine
Attn: Harry Gayley
Nottingham Way
Trenton, NJ 08602

Failure Analysis Assoc.
Attn: Dr. Clifford Wells
2225 E. Bayshore Rd.
Palo Alto, CA 94303

Garrett Turbine Eng. Co.
Attn: Joe Adams (503-4Z)
111 S. 34th St.
Box 5217
Phoenix, AZ 85010

Garrett Turbine Eng. Co.
Attn: Lee Matsch
111 S. 34th St.
Box 5217
Phoenix, AZ 85010

Gen. Elec. Co. - AEBG
Attn: Dr. Len Beitch K-221
Mgr, EM & LM
Evandale, OH 45215

Gen. Elec. Co. - AEBG
Attn: J. H. Laflen
Mail Drop G-60
Evendale, OH 45215-6301

Gen. Elec. Co.
Attn: Library
1000 Western Ave.
Lynn, MA 01905

Gen. Elec. Co.
Attn: Library
Box 8
Schenectady, NY 12301

Gen. Elec. Co. - AEBG
Attn: Joe McKenzie
Technical Programs
Mail Drop H-9
Evandale, OH 45215

Gen. Elec. Co.
Attn: Donald Mowbray
Bldg. 55-219
1 River Rd.
Schenectady, NY 12345

Gen. Elec. Co. - AEBG
Attn: Dr. Mel Roberts
Mail Drop K-69
Evandale, OH 45215

Gen. Elec. Co. - R&D Ctr.
Attn: Dr. David Woodford
Bldg. K-1, Rm 231M
Schenectady, NY 12301

Gen. Elec. Co. - AEBG
Attn: Kennard Wright
Evendale, OH 45215-6301

Gen. Elec. Co. - AEBG
Attn: T. Cook
Evendale, OH 45215-6301

Georgia Inst. of Tech.
Attn: Prof. S. Antolovich
Fracture & Fatigue Lab
Bunger-Henry Bldg.
Atlanta, GA 30332

Hamilton Standard
Attn: Gerald Molter
Mail Stop 1-1-6
Bradley Field Rd.
Windsor Locks, CT 06096

Hibbitt, Karlsson & Sorensen, Inc.
Attn: Dr. Kevin Walker
35 South Angell St.
Providence, RI 02906

Univ. of Illinois
Attn: Prof. D. Socie
Dept. Mech Engrng
1206 W. Green St
Urbana, IL 61801

I. I. T. Research Inst.
Attn: Humphries
10 W. 35th St.
Chicago, IL 60616

Int'l Harvester Co. - Solar
Attn: Library
2200 Pacific Hwy.
San Diego, CA 92101

Lockheed California
Attn: Library
Burbank, CA 91503

Lockheed Huntsville
Attn: W. H. Armstrong
Mgr, Struct & Mech
Huntsville, AL 35806

Mass. Institute of Tech.
Attn: Prof. Regi Pelloux
Rm 8-237
77 Mass Ave.
Cambridge, MA 02139

McDonnell Douglas
Attn: Library
Missiles & Space Div.
5301 Bolsa Ave.
Huntington Beach, CA 92647

Michigan State Univ.
Attn: Dr. John Martin
MMM Dept.
330 Engineering Bldg.
E. Lansing, MI 48824

NASA-AFWAL Tech Liaison
Attn: Everett Bailey
AFWAL/DO
WPAFB, OH 45433

NASA Headquarters
Attn: Dr. M. Greenfield
RTM-6, M&S Div.
Washington, DC 20546

NASA Langley Research Ctr.
Attn: Library
MS-185
Hampton, VA 23665

NASA - LeRC
Attn: Dr. Robert Bill
Head, Fatigue Res. Sect
MS 49-7
Cleveland, OH 44135

NASA - LeRC
Attn: D. E. Sokoloski
Mail Stop 49-1
Cleveland, OH 44135

NASA - LeRC
Attn: T. J. Miller
Mail Stop 49-3
Cleveland, OH 44135

NASA - LeRC
Attn: HOST Proj. Off.
Mail Stop 49-7
Cleveland, OH 44135

NASA - LeRC
Attn: R. H. Johns
Mail Stop 49-6
Cleveland, OH 44135

NASA - LeRC
Attn: Dr. S. R. Levine
Mail Stop 105-1
Cleveland, OH 44135

NASA - LeRC
Attn: D. B. Ercegovic
Mail Stop 6-11
Cleveland, OH 44135

NASA - LeRC
Attn: D. R. Englund
Mail Stop 77-1
Cleveland, OH 44135

NASA - LeRC
Attn: J. E. Rohde
Mail Stop 6 - 10
Cleveland, OH 44135

NASA - LeRC
Attn: N. T. Saunders
Mail Stop 3-8
Cleveland, OH 44135

140

NASA - LeRC
Attn: J. A. Ziemianski
Mail Stop 49-6
Cleveland, OH 44135

NASA - LeRC
Attn: A. Kaufman
Mail Stop 49-7
Cleveland, OH 44135

NASA - LeRC
Attn: Dr. R. L. Thompson
Mail Stop 49-6
Cleveland, OH 44135

NASA - LeRC
Attn: M. A. McGaw
Mail Stop 49-7
Cleveland, OH 44135

NASA - LeRC
Attn: T. W. Orange
Mail Stop 49-6
Cleveland, OH 44135

NASA - LeRC
Attn: Dr. L. Berke
Mail Stop 49-6
Cleveland, OH 44135

NASA - LeRC
Attn: Dr. D. A. Robinson
Mail Stop 49-6
Cleveland, OH 44135

NASA - LeRC
Attn: Dr. R. Ellis
Mail Stop 49-6
Cleveland, OH 44135

NASA - LeRC
Attn: Dr. R. L. Dreshfield
Mail Stop 49-1
Cleveland, OH 44135

NASA - LeRC
Attn: S. J. Grisaffe
Mail Stop 49-1
Cleveland, OH 44135

NASA - LeRC
Attn: Dr. R. V. Miner
Mail Stop 49-3
Cleveland, OH 44135

NASA - LeRC
Attn: M. V. Nathal
Mail Stop 49-1
Cleveland, OH 44135

NASA - LeRC
Attn: B. McKay
Mail Stop 49-3
Cleveland, OH 44135

NASA - LeRC
Attn: Dr. J. Gayda
Mail Stop 49-3
Cleveland, OH 44135

NASA - LeRC
Attn: Dr. Gary Halford
MS 49-7
Cleveland, OH 44135

NASA - LeRC
Attn: Marv Hirschberg
Chief, Fatigue & Fracture
MS 49-6
Cleveland, OH 44135

NASA - LeRC
Attn: Report Control
MS 5-5
Cleveland, OH 44135

NASA - LeRC
Attn: Library
MS 60-3
Cleveland, OH 44135

NASA - LeRC
Attn: S&T Section
MS 501-11
Cleveland, OH 44135

NASA - LeRC
Attn: AR&TL Office
MS 77-5
Cleveland, OH 44135

NASA - LeRC
Attn: AFSC Liaison Office
MS 501-3
Cleveland, OH 44135

NASA Marshall Space Ctr.
Attn: Library
Huntsville, AL 35812

NASA Marshall Space Ctr.
Attn: Carmelo Bianca
EP 42, Bldg 4610
Huntsville, AL 35812

NASA Marshall Space Ctr.
Attn: Larry Salter
EP46, Bldg 4610
Huntsville, AL 35812

NASA Marshall Space Ctr.
Attn: Bryan McPherson
Huntsville, AL 35812

NASA Marshall Space Ctr.
Attn: B Bhat
Huntsville AL 35812

NASA Marshall Space Ctr.
Attn: P. Munafo
EH22, Bldg 4612
Huntsville, AL 35812

NASA Sci. & Tech. Info
Attn: Accessioning Dept.
Box 8757
Balt/Washington International Airport
Maryland 21240

Naval Ship R&D Ctr
Attn: Library
Code 522.1
Bethesda, MD 20084

Northwestern Univ.
Attn: Dr. Julia Weertman
Dept. Matl's Sci
Evanston, IL 60201

O R N L   Box X
Attn: Dr. Charles Brinkman
Metals & Ceramics Div.
Oak Ridge, TN 37830

O'Donnell & Assoc.
Attn; Dr. W. O'Donnell
241 Curry Hollow Rd.
Pittsburgh, PA 15232

Pennsylvania State Univ.
Att: Dr. Sam Zamrik
121 Hammond Bldg.
University Park, PA 16302

Rensselaer Polytech Inst.
Attn: Prof. Norman Stoloff
Dept. of Matl's Eng.
Troy, NY 12181

Rockwell Int'l
Att: Dr. Mike Mitchell
Rockwell Science Ctr.
P. O. Box /1085
Thousand Oaks, CA 91360

Rocketdyne
Attn: Dr. Bob Jewett AC10
6633 Canoga Ave.
Canoga Park, CA 91304

Rocketdyne
Attn: Ed Larson AC10
6633 Canoga Ave.
Canoga Pk, CA 91304

Rocketdyne
Attn: Jack Lewis AC10
6633 Canoga Ave.
Canoga Pk, CA 91304

Rockwell Int'l
Attn: Library
6633 Canoga Ave.
Canoga Pk, CA 91304

Rolls Royce, Inc.
Attn: Dr. Ashok Thakker
1895 Phoenix Blvd.
Atlanta, GA 30349

Sandia Labs
Attn: Jack Hyzak
Division 8314
Box 969
Livermore, CA 94550

Sandia Labs
Attn: Library
Albuquerque, NM 87115

Southern Research Inst.
Attn: Library
2000 9th Ave. S.
Birmingham, AL 35205

Southwest Research
Attn: Dr. Gerald Leverant
P. O. Drawer 28510
San Antonio, TX 78284

Southwest Research
Attn: Dr. U. S. Lindholm
P. O. Drawer 285
San Antonio, TX 78284

Southwest Research
Attn: Library
8500 Culebra Rd.
San Antonio, TX 78284

Stanford Univ.
Attn: Prof. Alan K. Miller
Dept. Matl's Sci & Eng
Stanford, CA 94305

Syracuse Univ.
Attn: Dr. H. W. Liu
409 Link Hall
Syracuse, NY 13210

T R W Inc.
Attn: Dr. C. Kortovich
T/M-3357
23555 Euclid Ave.
Cleveland, OH 44117

Teledyne CAE
Attn: Hugh Gaylord
Mgr., Explor. Dev. Appl.
1330 Laskey Rd.
Toledo, OH 43612

Teledyne CAE
Attn: Bryon L. Lewis
1330 Laskey Rd.
Toledo, OH 43612

Teledyne CAE
Attn: Tom Moyer
Box 6971
Toledo, OH 43612

Teledyne CAE
Attn: Jerry Walcher
Box 6971
Toledo, OH 43612

Univ. of Tennessee
Attn: Dr. V. Smith
Space Institute
Tullahoma, TN 37388

V. P. I. & State Univ.
Attn: Dr. Norm Dowling
Eng. Sci. & Mech. Dept.
Blacksburg, VA 24061

Williams Research
Attn: Peter Nagy
2280 W. Maple Rd.
Walled Lake, MI 48088

Westinghouse - R&D Ctr.
Attn: Robert Johnson
Bldg. 401, Rm. 2X9G
Pittsburgh, PA 15235

Westinghouse - ARD
Attn: Alfred Snow
Box 158
Madison, PA 15663

NASA Headquarters
Attn: Charles Bersch
RTM-6, M&S Div.
Washington, DC 20546

N. A. P. C.
Attn: A. Martino
P.O. Box 7176
Mgr. R&T Div.
Trenton, NJ 08628

Wright Patterson Air Force Base
Attn: Richard Hill
AFWAL/POTC
AREA B, Bldg 18
Wright Patterson Air Force Base
OH 45433

AiResearch Mfg. Co.
Attn: Dr. Tekal Nath
Mail T-42, Dept 93-3
2525 W 190th St
Torrance. CA 90509

University of Akron
Attn: Prof. Padovan
Dept. Civil Eng.
Akron, OH 44325

Argonne Nat. Lab.
Attn: S. Majumdar
9700 S. Cass Ave.
Argonne, IL 60439

AVCO - Lycoming Div
Attn: Louis Fiedler
Chief, Matl's Eng & Dev
550 S Main St
Stratford, CT 06497

Case Western Reserve Univ
Attn: Prof. A. Chudnovski
205 Bingham Bldg.
10900 Euclid Ave.
Cleveland, OH 44106

Eng Science Software Inc
Attn: Dr. Kevin Walker
P 65 Log Road
Smithfield, RI 02917

Exxon Res & Eng Co
Attn: R P Gangloff
Box 45
Linden, NJ 07036

FAA - New England Reg.
Attn: Dan Salvano
12 New England Exec. Park
Burlington, MA 01803

Failure Analysis Assoc.
Attn: Dr. Jerrell Thomas
2225 E. Bayshore Rd
Palo Alto, CA 94303

Grumman Aerospace
Attn: R. Friedman
Mail Stop B-43/35
Bethpage, LI NY 11714

General Electric Co
Attn: Ted Russell   G-25
Turbine Division
Schenectady, MY 12345

NASA - LeRC
Attn: J. Acurio, Director
USAR&TL Propulsion Lab
Cleveland, OH 44135

Johns Hopkins Univ.
Attn: Prof. W.N. Sharpe
Chairman, Dept of Mech
123 LaTrobe Hall
Baltimore, MD 21218

Lockheed Georgia
Attn: H.S. Sweet
Marietta, GA 30060

McDonnell Douglas
Attn: F.C. Claser
Dept 243
Box 516
St Louis, MO 63166

McDonnell Douglas
Attn: R.T. Kawai   (36-41)
3852 Lakewood Blvd
Long Beach, CA 90801

Univ. of Minnesota
Attn: Dr. W.W. Gerberich
Dept Chem Eng & Matl Sci
Minneapolis, MN

NASA - LeRC
Attn: R.E. Gaugler
Mail Stop 6-10
Cleveland, OH 44135

NASA - LeRC
Attn: T.W. Orange
Mail Stop 49-7
Cleveland, OH 44135

NASA - LeRC
Attn: J.F. Saltsman
Mail Stop 49-7
Cleveland, OH 44135

NASA - LeRC
Attn: R.J. Simoneau
Mail Stop 6-10
Cleveland, OH 44135

Northwestern Univ
Attn: Prof S. Nemat-Nasser
Dept of Civil Eng
Evanston, IL 60201

NASA - LeRC
Attn: S&MT Div. Files
MS 49-6
Cleveland, OH 44135

O R N L   Box X
Attn: J. McGowan
Oak Ridge, TN 37830

Rensselaer Polytech Inst
Attn: Dr. Erhard Krempl
Mech & Aero Eng Dept
Troy, NY 12181

Rocketdyne
Attn: Dr. D. Matejczk/AC10
6633 Canoga Ave
Canoga Pk, CA 91304

Rockwell Int'l
Attn: Dr. Mike Mitchell
Rockwell Science Ctr
P.O. Box 1085
Thousand Oaks, CA 91360

Rocketdyne
Attn: Jim Newell   AC10
6633 Canoga Ave
Canoga Pk, CA 91304

Sandia Labs
Attn: D.W. Lobitz
Div 1541
Box 5800
Albuquerque, NM 87115

Southwest Research Inst
Attn: Dr. Thomas Cruse
PO Drawer 28510
San Antonio, TX 78284

Southwest Research
Attn: Dr. C.S. Chan
PO Drawer 285
San Antonio, TX 78284

Texas A & M University
Attn: Dr. W.L. Bradley
College Station, TX 77843

Texas A & M University
Attn: Dr. Walter Haisler
Aerospace Eng Dept
College Station, TX 77843

Williams Research
Attn: R.L. Maxwell
2280 W Maple Rd
Walled Lake, MI 48088

Westinghouse - Hanford
Attn: L.K. Severud
Mgr, Plant Analysis
Box 1970
Richland, WA 99352

Cummins Engine
Attn: Justin Drake
Tech Ctr
500 S Poplar St
Columbus, IN 47201

University of Dayton
Attn: Dr. Joseph Gallagher
Research Institute
Rm 563 Kettering Bldg
Dayton, OH 45469

Defense Documentation Ctr
Cameron Station
5010 Duke St
Alexandria, VA 22314

NASA-AFWAL Tech Liaison
Attn: Everett Bailey
AFWAL/DO
Wright Patterson Air Force Base, OH
                                45433

Scientific Info Service
Attn: Ref. USZ   #
7 Woodland Ave
Larchmont, NY 10538

O R N L   Box X
Attn: Dr. Robert Swindeman
Metals & Ceramics Div
Oak Ridge, TN 37830

NASA - LeRC
Attn: N. T. Saunders
Mail Stop 3-8
Cleveland, OH 44135

Scientific Info. Service
Attn: Ref USZ
7 Woodland Ave.
Larchmont, NY 10538

1.REPORT NO. NASA CR-174844	2. GOVERNMENT AGENCY	3.RECIPIENT'S CATALOG NO.	
4.TITLE AND SUBTITLE Creep Fatigue Life Prediction for Engine Hot Section Materials (Isotropic)		5. REPORT DATE March 1985	
		6. PERFORMING ORG. CODE	
7.AUTHOR(S) Vito Moreno, David Nissley, Li-Sen (Jim) Lin		8. PERFORMING ORG. REPT. NO. PWA-5894-34	
9.PERFORMING ORG. NAME AND ADDRESS UNITED TECHNOLOGIES CORPORATION Pratt & Whitney Engineering Division		10. WORK UNIT NO.	
		11. CONTRACT OR GRANT NO. NAS3-23288	
12. SPONSORING AGENCY NAME AND ADDRESS National Aeronautics and Space Administration Lewis Research Center 21000 Brookpark Road, Cleveland, Ohio 44135		13. TYPE REPT./PERIOD COVERED Annual Report (Second)	
		14. SPONSORING AGENCY CODE	

15. SUPPLEMENTARY NOTES
Project Manager: G.R. Halford, NASA Lewis Research Center, Cleveland, Ohio

16. ABSTRACT
This report summarizes the activities performed during the first two years of a two-phase program aimed at improving the high temperature crack initiation life prediction technology for gas turbine hot section components. In Phase I (baseline) effort, low cycle fatigue (LCF) models, using a data base generated for a cast nickel base gas turbine hot section alloy (B1900+Hf), were evaluated for their ability to predict the crack initiation life for relevant creep-fatigue loading conditions and to define data required for determination of model constants. The variables included strain range and rate, mean strain, strain hold times and temperature. None of the models satisfactorily predicted all of the life trends within reasonable data requirements. A Cycle Damage Accumulation (CDA) was therefore developed which fundamentally follows an exhaustion of material ductility approach. Material ductility is estimated based on observed similarities of deformation structure between fatigue, tensile and creep tests. The cycle damage function is based on total strain range, maximum stress and stress amplitude and includes both time independent and time dependent components. The CDA model accurately predicts all of the trends in creep-fatigue life with loading conditions. In addition, all of the CDA model constants are determinable from rapid cycle, fully reversed fatigue tests and monotonic tensile and/or creep data.

17. KEY WORDS (SUGGESTED BY AUTHOR(S)) creep fatigue , crack initiation life prediction, Isotropic material	18. DISTRIBUTION STATEMENT		
19. SECURITY CLASS THIS (REPT)	20. SECURITY CLASS THIS (PAGE)	21. NO. PGS	22. PRICE *

* For sale by the National Technical Information Service, Springfield, VA 22161